AD-A176 808 THREE-DIMENSIONAL NUMERICAL STUDIES OF THE PHYSICS OF 1/2
SEMICONDUCTOR CRYST (U) SCIENTIFIC RESEARCH ASSOCIATES
INC GLASTONBURY CT Y T CHAN ET AL FEB 87
UNCLASSIFIED SRA-R-920018-F N00014-83-C-0510 F/G 20/12 NL

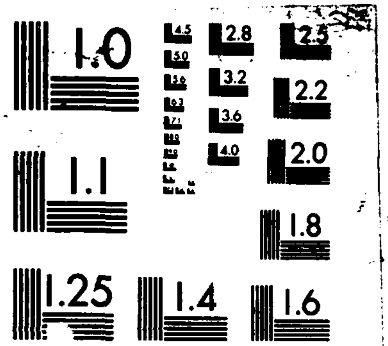

MICROCOPY RESOLUTION TEST CHART
NATIONAL BUREAU OF STANDARDS-1963-A

(12)

Report R-920018-F

AD-A176 808

THREE-DIMENSIONAL NUMERICAL STUDIES OF THE PHYSICS OF SEMICONDUCTOR CRYSTALL GROWTH

Y.T. Chan, H.J. Gibeling, N-S. Liu, H.L. Grubin
Scientific Research Associates, Inc.
50 Nye Road, P.O. Box 1058
Glastonbury, CT 06033

February 1987

Final Report for Period 1 August 1983 - 30 September 1986

Prepared For:

OFFICE OF NAVAL RESEARCH
800 No. Quincy Street
Arlington, VA 22217

392929 cL

SECURITY CLASSIFICATION OF THIS PAGE

REPORT DOCUMENTATION PAGE

1a. REPORT SECURITY CLASSIFICATION
Unclassified

1b. RESTRICTIVE MARKINGS
AD-A176 808

2a. SECURITY CLASSIFICATION AUTHORITY

2b. DECLASSIFICATION / DOWNGRADING SCHEDULE

3. DISTRIBUTION / AVAILABILITY OF REPORT
Approved for Public Release; Distribution Unlimited

4. PERFORMING ORGANIZATION REPORT NUMBER(S)
R920018-F

5. MONITORING ORGANIZATION REPORT NUMBER(S)

6a. NAME OF PERFORMING ORGANIZATION
SCIENTIFIC RESEARCH ASSOCIATES

6b. OFFICE SYMBOL *(If applicable)*
8N189

7a. NAME OF MONITORING ORGANIZATION

6c. ADDRESS *(City, State, and ZIP Code)*
50 Nye Road, P.O. Box 1058
Glastonbury, CT 06033

7b. ADDRESS *(City, State, and ZIP Code)*

8a. NAME OF FUNDING/SPONSORING ORGANIZATION
Office of Naval Research

8b. OFFICE SYMBOL *(If applicable)*
N00014

9. PROCUREMENT INSTRUMENT IDENTIFICATION NUMBER
N00014-83-C-0510

8c. ADDRESS *(City, State, and ZIP Code)*
800 North Quincy Street
Arlington, VA 22217

10. SOURCE OF FUNDING NUMBERS

PROGRAM ELEMENT NO.	PROJECT NO.	TASK NO.	WORK UNIT ACCESSION NO.

11. TITLE *(Include Security Classification)*
"Three-Dimensional Numerical Studies of the Physics of Semiconductor Crystal Growth"

12. PERSONAL AUTHOR(S)
Y.T. Chan, H.J. Gibeling, N-S. Liu, H.L. Grubin

13a. TYPE OF REPORT	13b. TIME COVERED	14. DATE OF REPORT (Year, Month, Day)	15. PAGE COUNT
Final	FROM 83/8/1 TO 86/9/30	87/02/09	115

16. SUPPLEMENTARY NOTATION

17. COSATI CODES

FIELD	GROUP	SUB-GROUP

18. SUBJECT TERMS *(Continue on reverse if necessary and identify by block number)*
Crystal Growth; Silicon Growth; Czochralski Growth, Numerical Analysis.

19. ABSTRACT *(Continue on reverse if necessary and identify by block number)*
The present study involves the development and application of a numerical technique to the most popular method of growing silicon crystal - the Czochralski process. The equations solved for the melt phase are the conservation equations for the mass, momentum, energy and nonreacting species. For the crystal phase, the energy balance equation is solved. The governing equations are formulated using primitive variables and are not thereby restricted to two-dimensional symmetry. The crystal and melt phases are coupled through thermal conditions applied along the melt-crystal interface. The shape of the melt-crystal interface and meniscus are determined through solutions to differential equations that govern the kinematic conditions at the specific interfaces, and are not assumed a priori. The numerical procedures are obtained by a well documented procedure known as the consistently split Linearized Block Implicit (LBI) scheme, originally developed at SRA. Calculations, including one three-dimensional case, are performed for various growth conditions suitable for silicon crystal growth. The present study has successfully demonstrated the numerical capabilities for Czochralski crystal growth simulations. Keywords;

20. DISTRIBUTION/AVAILABILITY OF ABSTRACT
☒ UNCLASSIFIED/UNLIMITED ☐ SAME AS RPT. ☐ DTIC USERS

21. ABSTRACT SECURITY CLASSIFICATION

22a. NAME OF RESPONSIBLE INDIVIDUAL

22b. TELEPHONE *(Include Area Code)*

22c. OFFICE SYMBOL

DD FORM 1473, 84 MAR — 83 APR edition may be used until exhausted. All other editions are obsolete.

SECURITY CLASSIFICATION OF THIS PAGE

TABLE OF CONTENTS

1. INTRODUCTION

1-1. General Aspects

Naval Electronics systems process extremely large quantities of data today and it is expected that demands on high speed real-time signal processing will increase substantially in the next decade. Requisite device speed and densities demand that critical feature size be reduced to submicron or ultrasubmicron scales.

This reduction places uncommon demands on the quality of the materials used in device fabrication. For example, in present bipolar devices, crystallographic microdefects, precipitates, clusters, and deep level traps can result in microplasma and junction leakage, current channeling, nonuniform heating, degraded pn junction breakdown, etc. Taken in combination these introduce limits on size and/or chip yield. In silicon MOS devices, similar defects lead to generation-recombination centers and leakage current sources. Here refresh times in dynamic RAMs, threshold shifts in static RAMs, maximum operating temperatures, etc., are degraded. The situation in gallium arsenide is even more difficult. Defects in the substrate material are severely limiting yield, raising costs, and causing time scales for projected commercial and military applications to be pushed back several years. This is true for both GaAs digital devices and the new MMIC devices.

Material variations arise during all stages of device fabrication, beginning with crystal growth. In most methods of synthetic production of single crystals, the crystal grows slowly from a fluid nutrient. Being a fluid, various hydrodynamic mechanisms drive it's motion. The fluid motion is of concern to crystal growers because they determine the transport of impurities, heat, etc., to the grown crystal, and the stresses on the crystal.

The present study involves the application of numerical techniques to the most popular method of growing crystals: the Czochralski (Cz) process. The Cz method is the principle method by which silicon and gallium arsenide boules are obtained in the microelectronics industry. The study was supported by the Office of Naval Research through the DESAT program. The motivation for the program is clear. It is currently accepted that the properties of the melt are the primary factors affecting the quality of silicon and gallium arsenide substrates. The properties of the melt are themselves determined by a broad and interacting matrix of variables that include crystal rotation, crucible rotation, pull rate, crucible temperature, pressure, orientation, etc. These input variables have been traditionally operator controlled, and the quality of the boule was often dependent upon the past experience of the operator, and resulting trial and error procedures. Because of the high demands of both the commercial and military markets, as well as international competition, the control of the growth variables and the manner in which a variation of one affects another, systematic techniques are needed for optimization of crystal growth. The very first step in this optimization is the development of numerical codes that closely replicate the growth procedures. The second is the development of software that is coupled to the actual growth apparatus and is capable of being self-correcting. At this point in time, both of these procedures are under development. But the degree to which this coupled approach is useful is dependent upon the constraints of the equations governing the fluid flow.

Pragmatically, present crystal growers require a three dimensional transient algorithm that describes crystal growth and is capable of handling such external effects such as the presence of magnetic field, electric fields, encapsulation, melt replenishment, etc. Such algorithms have been developed at Scientific Research Associates, Inc. (SRA) and have been applied to silicon and gallium arsenide.

The equations solved in the SRA study are the continuity, momentum and energy balance equations for the melt, as well as the species concentration equation. For the crystal, the energy balance equation is solved. The governing equations are formulated using primitive variables and are not thereby restricted to limitations of two dimensional symmetry. The crystal and melt phases are coupled through thermal and dynamic conditions applied along the melt-crystal and melt-free surface boundaries. For most of the calculations the shape of the interface is determined through solutions to differential equations that govern the kinematic conditions at the specific interface, and are not assumed a priori. The numerical procedures are obtained by a well documented procedure known as the consistently split Linearized Block Implicit (LBI) scheme, originally developed at SRA. While SRA's numerical studies of crystal growth are perhaps the most general, to date, the extent to which the procedures and results are of relevance should be placed in perspective at this early stage in the discussion.

All numerical studies of Cz growth involve simplifying assumptions and result in placing the studies in different groups, or categories as summarized in Table 1.1.1. The first groups involves only studies of the thermal-hydrodynamics of the melt phase. That is, the energy and momentum balance equations for the melt were solved. The assumptions for this group are generally: 1) planar free surface; 2) planar melt-crystal interface, and; 3) uniform temperature distribution in the crystal phase. The second group involves the studies of temperature distribution in the melt phase and/or the crystal phase. The influence of hydrodynamics of the melt on the temperature is assumed to be small; and only the energy balance equation is solved. However, attention in this group was paid to the shape of the free surface as well as that of the melt surface interface. The third group includes that of the first but also includes energy balance within the crystal. The melt and crystal phases are coupled together via thermal conditions at the melt-crystal interface. The analysis on this group is difficult, and the shape of the free surface and the melt surface interface is not considered.

The present work extends that of the last group, plus: i) the shape of the free surface and includes the mensicus at the crystal-melt-argon contact point, ii) the shape of the melt-crystal interface, iii) normalized dopant distribution in the melt, iv) dopant distribution near the melt-crystal interface, v) the effect of replenishment, vi) the dependence of melt properties on crucible size, vii) the dependence of melt properties on crystal size, viii) the dependence of melt properties on crystal penetration of the melt.

The structure of the paper is as follows: Section 1.2 presents a brief discussion of CZ growth. This is followed by a historical summary of the earlier studies. Section 2 describes the mathematical formulation of the CZ growth problem. In Section 3 numerical details are discussed, including a description of the body-fitted coordinate algorithm, transient capability and CRAY vertorization. Section 4 contains a description of model 'numerically based' calculations. Application to silicon is contained in Sections 5 and 6, with the latter devoted to three dimensional studies. Conclusions and Recommendations of future directions is contained in Section 7.

1-2. Fundamentals of Czochralski growth

The basic principle of growing a single crystal by the Czochralski method is shown in Figure 1.1.1. The crucible is initially filled with the material e.g., polycrystalline Si, to be crystallized. Thermal energy is supplied by a heater surrounding the crucible thereby raising the temperature of the solid above its melting temperature. A seed crystal, at the end of a rod, is then dipped into the melt and, after appropriate start-up procedures, slowly withdraw from the melt.

Under suitable temperature conditions recrystallizaton in the form of single crystals occurs. This method, bears Czochralski's name, who in 1916 [1], established it as a means to determine the crystallization velocity of metals. For the growth of silicon (Si) and germanium (Ge) single crystals, the typical pulling rate is less than 3.5mm/min. For a 2 inch diameter gallium arsenide crystal is about 0.15 mm/min.

To keep the feeding material molten, the crucible is maintained at a temperature above the melting point. The resulting axial and radial temperature gradients within the melt cause natural convection. In order to improve uniformity, the growing crystal is rotated as it is pulled. The rotating crystal acts as a centrifugal pump sucking-up the melt fluid axially, while ejecting it tangentially.

As the crystal rotates, a viscous shear layer (Ekman layer) is formed under the crystal, tending to isolate the growing solid/melt interface from the melt near the bottom of the crucible. The radially outward flow, due to the rotating crystal, is met by a countering radial inflow fluid driven by the hot crucible wall.

A resultant downflow occurs at some radial distance, whose position is determined by the relative strength of the two rotational flows and the buoyancy-driven convection.

Rotation of the crucible, which is also sometimes utilized, is implemented to smooth out additional thermal asymmetries that arise from irregularities in heating. This also introduces a centrifugal flow. The combined effects of crystal and crucible rotation, even in an iso-thermal fluid, are complex and depend on whether the two are iso-rotating or counter-rotating.

With iso-rotation, a Taylor-Proudman cell can be established beneath the crystal, with a detached shear layer separating it from the outer region. The outer region effectively rotates as a solid body with the crucible [2]. Counter-rotation yields a more complex flow pattern beneath the crystal with a stagnation layer separating the flows driven by the crystal from the flows driven by crucible rotation [2,3]. Typical crystal and crucible rotation rates are in the range of 1 to 50 and 0.5 to 30rpm, respectively.

In addition to the natural and forced convection, there is thermo-capillary flow near the free surface. Since the surface tension coefficients of most

Cz melts (for Si, it is -0.43 dyne/cm/k) vary with temperature, a non-zero temperature gradient along the free surface will cause a nonuniform surface tension force, resulting in a finite shear stress at the free surface. For example, for a melt with negative coefficient of surface tension, the surface tension diminishes with increasing radius, provided the crucible temperature is higher than the melt temperature. The resultant effect is that the melt beneath the free surface is pulled toward the crystal. Motion induced in this manner is called Marangoni flow, and is further complicated by the nonplanar nature of the free surface, the loss of heat from the free surface and the consequent destabilizing vertical temperature gradient that gives rise to a Benard-like convection.

In addition, the shape of the melt-crystal interface is controlled by both the coupled effects of heat transfer throughout the crystal growing system and the shape of the free surface. Capillarity and the wetting of the crystal by its melt determine the position and shape of the meniscus.

1-3. Background

Recent tutorial and review articles [4-8] display the nature of such convective motions and their influence on the quality of the crystal. Intensive research to understand the hydrodynamics of the Cz growth system have been carried out in the past decade. As discussed earlier, numerical investigation of Cz growth can be classified into three groups (see Table 1.1.1). Group A involves the studies on the hydrodynamics of the melt phase with the assumption of a planar free surface and melt crystal interface. Group B involves studies of temperature distribution within both melt and crystal phases. Group C studies combine both that of Groups A and B, without the assumption of planar interfaces.

The Group A assumptions include: 1) The melt-crystal interface and free surface are planar; 2) The crucible and crystal are at uniform temperatures and rotating symmetrically; 3) Crystal phase is not studied; 4)The pulling velocity is zero. The first assumption ignores the kinetics of the surfaces which are important when the solute distribution and thermal gradients near the interface are to be determined. The second assumption rests with formulation limitations as it is restricts to axisymmetric situations. Since the crystal phase is not studied in this group, effects due to heat loss at the vertical surface of the crystal cannot be incorporated at the planar melt-crystal interface.

The pioneering work on numerical simulation of convective flow was carried out by Kobayashi [9,11] and Langlois [10] using a model that employed a vorticity-stream function procedure. In these models, the axial and radial velocities were replaced by a stream function through the use of the continuity equation. The pressure was explicitly eliminated by introducing the vorticity function, and the governing equations were then written in finite difference form. Kobayashi [9,11] further assumed a steady state and solved each equation successively. Since the unknowns were coupled, the entire procedure was repeated iteratively until prespecified convergence criteria was met. Langlois [10] formulated the problem as a transient and used a forward time explicit scheme. The stream function (continuity) was calculated at each time step by a successive over-relaxation method. This numerical method (either steady or unsteady) was then used to simulate convective flows in Cz systems (also in a floating zone system, e.g., [12]) with various nondimensional parameters [13-16]. Instead of using a finite difference and SOR methods for the vorticity-stream function formulation, Crochet and Wouters [17] used finite element methods to study convective flows due to various rotational rates and buoyancy forces. The numerical method has been demonstrated to be able to handle oscillatory natural convective flow. These papers have made significant contributions to the understanding of the hydrodynamics of the melt.

In the Group B studies, only the temperature distribution in the melt and/or crystal phase is solved. A study by Williams and Reusser [18] used a finite element method to determine the temperature distribution in the crystal. Their work assumed a planar melt-crystal interface and specified the boundary conditions from the measured surface temperatures. This approach is not general and is unsuited to predictive purposes. More recently, Derby et al., [19] included a meniscus and nonplanar interfaces in two dimensional, steady state, small scale prototype calculations applicable to liquid encapsulated Czochralski (LEC) growth. The thermal equation in each phase was solved using a finite element technique. However, phenomena associated with fluid flow were totally ignored. Thus the shape of the meniscus was simplified to the well known Young-Laplace equation, for which an analytical solution exists [20]. The isotherm at the melt temperature was used to define the melt-crystal interface. Since the flow field was not solved, a solute distribution cannot be determined from this analysis. A study by Ramachandran and Dudukovic [21] used an iterative finite element method to predict the temperature distribution and the position of the melt-crystal interface in the crystal phase. The method accounted for the radiative heat transfer between the various 'surfaces' presented to the crystal pulling apparatus.

In Group C studies, Chang and Brown [21] formulated the vertical Bridgeman system using primitive variables and approximated the solution using a Galerkin finite element method. In their study, the steady state two dimensional Navier-Stokes equations are solved for the case in which flow is due to free convection only. The isotherm at the melt temperature is considered as the melt-crystal interface and is approximated by a set of Hermite cubic polynominals. The coefficients associated with the field variables and interface shape formed a nonlinear set of algebraic equations. In the vertical Bridgeman system, the melt fluid is continuously fed from the bottom while the crystal is formed at the top. No free surface exists in this configuration. The range of parameters studied in these groups is summarized in Table 1.1.2.

Because of the difficulty in making measurements in the melt (e.g. opaqueness, high temperature of the melt), simulation experiments [23-27] have been performed to study melt behavior under Cz conditions. The crystal is simulated by a rotating disc, and the crucible by a heated cylindrical container. The working fluid (simulating the melt) is taken to be water [23-25, 27] and $NaNO_3$ [26] so that the Prandtl number is of the same order as the oxide melts. Photographs from Miller [25] show a 'wheel spoke' pattern at the free surface. The 'ripples' are believed to be due to Marangoni convection resulting from surface tension gradients along the free surface. At high crystal rotation rates, three distinct zones are observed [25]: the stagnant layer at the bottom, the thermally driven zone in the middle, and the crystal driven zone near the crystal. Lamprecht et al., [26] put tracer particles in $NaNO_3$, so that when the fluid was illuminated with a sheet of light, photographs could be taken. By measuring the relative positions of the tracer's particles between time frames, radial velocities were measured. The temperature distribution was measured with thermocouples. Marangoni convection was not observed because the surface tension coefficient for $NaNO_3$ is small (-0.07 dyne/cm/k at 300°C, -0.17 dyne/cm/k for water at 50°C). In another experiment done with water (Jone [27]), an array of thermocouples was located 1 cm below a rotating disc (simulated crystal) to measure the mean and fluctuating temperature when the rate of rotation of the disc was increased. Observed experimental flow patterns and temperature variations qualitatively agree with the melt behavior under Czochralski conditions.

Another aspect of crystal growth being studied is how the dopant impurities and heat are transported to the melt-crystal interface as a result of the convective flows. The flows due to the rotating crystal and the resultant solute distribution produced by segregation at the melt crystal interface have been treated by Wilson and others [28-32] using the similarity solutions of Von Karman [33] for the fluid flow. The melt-crystal interface is prescribed to be a planar disc normal to its axis of rotation. A suitable coordinate can be employed to accommodate the nonplanar crystal surface. The importance of these studies is that it is the behavior of the fluid adjacent to the growing crystal that is the most influential in controlling the solute uptake. The bulk of the melt provides the reservoir of solute. The spatial distribution of the solute in the melt is assumed to be uniform. Originated from Burton et al., [34] an analytical formula can be written for the effective segregation coefficient as a function of equilibrium segregation coefficient and a parameter, Δ. The latter can be interpreted as a concentration boundary layer thickness. Several numerical correlations for the parameter, Δ, as a function of the rotational rate and pulling rate of the crystal were developed in [28,32]. Additionally, Wilson and Favier [30,31,33] also included a time dependent sinuodial varying pulling rate in their model to study compositional inhomogenities in the crystal. The rotating disk model [28-32,34] was limited to cases with a uniform spatial impurity distribution. Molecular oxygen which comes from a continuous corrosion of the crucible walls, is transported throughout the melt and the majority of it evaporates from the free surface with some fraction incorporated in the grown crystal. In this case, the spatial distribution within the melt is not uniform and thus this model is not applicable.

As discussed earlier the goal of the present study was to overcome many of the limitations associated with earlier studies and to develop numerical procedures that are capable of accurately predicting for Cz processes: 1) the thermal hydralic behavior of the melt, 2) the thermal behavior of the crystal; 3) the shapes of the free surface and melt-crystal interface; and 4) the species distribution in the melt fluid.

2. MATHEMATICAL ANALYSIS

2-1. Introduction

In the present study, the governing equations for the liquid state are the conservation equations for mass, momentum and energy of the melt. The only equation considered for the crystal is the heat conduction equation. The melt and crystal phases are coupled through appropriate thermal conditions applied along the interfaces. The interfacial positions are governed by nonlinear kinematic conditions, as discussed below. The solutions to the melt flow field and the temperature distribution inside the grown crystal, along with the positions of the interface, are obtained by a well documented numerical procedure known as the consistently split linearized block implicit (LBI) scheme [35] (see Appendix A).

The addition of free surface boundary conditions introduces nonlinear effects, since the location of free surface is not known a priori, and must emerge as part of the solution. The unknown surface location is obtained from a partial differential equation boundary condition that is coupled to flow within the melt. At the melt-solid interface, the conservation equations for the melt are coupled to the thermal conservation equation for the crystal through the energy balance condition.

In the calculations of the species concentration in the melt, species are assumed to be transported by two mechanisms; i) melt fluid motion, and ii) species diffusion. Concentration gradients induced by the temperature rise at the melt-crystal interface due to both latent heat of crystallization and the curvature of the melt-crystal interface are assumed to be small. Thus motion due to these concentration gradients is assumed to be small and is neglected.

2.2. Governing Equations

The equations describing flow within the melt and energy transport within the crystal are discussed below. Each of these equations are expressed, in two forms: a) in dimensional form, and b) in dimensionless form.

The first equation of interest is that governing the distribution of temperature within the solid crystal. The equation for heat transport is:

$$\frac{\partial}{\partial t} T_s + \frac{\partial}{\partial z}(u'_p T_s) = \alpha_s \nabla^2 T_s \tag{1a}$$

$$\frac{\partial}{\partial t} \theta_s + \frac{\partial}{\partial z}(u_p \theta_s) = \frac{1}{Pe} \nabla^2 \theta_s \tag{1b}$$

In the above T_s is the temperature of the crystal, u_p' the speed at which the crystal is pulled, α_s is the thermal diffusivity which is defined as $k_s/\rho_s' c_{ps}$, and k_s is the thermal conductivity, c_{ps} is the specific heat capacity and ρ_s' is the density. The dimensionless form of the equations is clear. θ_s represents T/T_m where T_m is the temperature of the melt. $u_p = u_p'/u_s$. The reference velocity is $u_s = R_s \omega_s$. R_s is the radius of the crystal. ω_s is the angular frequency of rotation of the crystal. The dimensionless number Pe is referred to as the Peclet number and is given by Pe = $u_s r_s/\alpha_s$. Note that the crystal radius is taken as the reference length, and the reference time is $1/\omega_s$.

The governing equations for the melt are as follows: (1) First there is the continuity equation

$$\frac{\partial}{\partial t}\rho + \nabla \cdot (\rho \underline{u}') = 0 \tag{2a}$$

$$\frac{\partial}{\partial t}\rho + \nabla \cdot (\rho \underline{u}) = 0 \tag{2b}$$

where ρ' is the density of the melt and u' its velocity. In dimensionless form the density is normalized to the density of the melt at the melt temperature. The second melt equation is the momentum balance equation, or more commonly the Navier-Stokes equation

$$\frac{\partial}{\partial t}\underline{u}' + \nabla \cdot (\underline{u}'\underline{u}') = -\frac{1}{\rho}\nabla P' + \underline{F} + \nu\left[\nabla^2 \underline{u}' - \frac{1}{3}\nabla(\nabla \cdot \underline{u}')\right] \tag{3a}$$

$$\frac{\partial}{\partial t}\underline{u} + \nabla \cdot (\underline{u}\,\underline{u}) = -\frac{1}{\rho}\nabla P + \underline{F} + \frac{1}{Re}\left[\nabla^2 \underline{u} - \frac{1}{3}\nabla(\nabla \cdot \underline{u})\right] \tag{3b}$$

Here F' is a force per unit mass and P' is the pressure. ν is the kinematic viscosity which is defined as μ/ρ'. In dimensionless units, the reference pressure is ρu_s^2. The dimensionless Reynolds number Re is given by $\frac{\rho u_s R_s}{\mu}$, where μ is the viscosity.

The third melt equation is the energy equation

$$\frac{\partial}{\partial t}T_l + \nabla \cdot (\underline{u}' T_l) = \alpha_l \nabla^2 T_l \tag{4a}$$

$$\frac{\partial}{\partial t}\theta_l + \nabla \cdot (\underline{u}\theta_l) = \frac{1}{RePr}\nabla^2 \theta_l \tag{4b}$$

In the above α_ℓ is the thermal diffusivity. In dimensionless form, Pr is the Prandtl number, and is given by ν/α_ℓ. The fourth melt equation, species transport equation, is

$$\frac{\partial}{\partial t} C'_K + \nabla \cdot (\underline{u}' C'_K) = D \nabla^2 C'_K \tag{5a}$$

$$\frac{\partial}{\partial t} C_K + \nabla \cdot (\underline{u} C_K) = \frac{1}{ReSc} \nabla^2 C_K \tag{5b}$$

where Sc is referred to as the Schmidt number, and is given by μ/D, and D is species diffusivity.

The force per unit mass term in equation (3) is given by

$$F' = -g(1 + \beta(T - \bar{T})) \tag{6a}$$

$$\underline{F} = \left[-\frac{1}{Fr} + \frac{Gr}{Re^2} \frac{T_m}{\Delta T} (\theta - \bar{\theta}) \right] \hat{e}_z \tag{6b}$$

where g is the acceleration due to gravity and β is the volumetric expansion coefficient of the melt. Fr is the Froude number and defined as u_s^2/gR_s, while Gr is the Grashof number and is defined as $g\beta\Delta T R_s^3/\nu^2$. Here, the Bousinesq approximation is adopted to account for the effects of natural convection. The formulation of the crystal growth problem allows for the incorporation of compressible fluid properties. While not likely to be important for a melt that is exposed to low pressure, significant departures may occur under either high pressure and/or encapsulation. The incorporation of compressibility into the algorithm requires the presence of an equation of state. Care must be taken in the choice of such an equation, in that it must yield results that are virtually identical to those obtained by others in the incompressible limit. The equation of state used below has been successfully applied to compressible fluids, and yields the same results as others in the incompressible limit [36]. This equation is:

$$P = \rho R \left(T_r - \frac{|u_l|}{2C_p} \right) \tag{7}$$

where R is the universal gas constant.

Further, according to the analysis given in [36], if Tr were the local total temperature in the fluid, equation (7) would represent the perfect gas law for an ideal fluid. However, if Tr is taken as a fictitious constant temperature of high enough value so that the Mach number Ma based upon u_ℓ and Tr is small, i.e.,

$$Ma = \frac{|\underline{u}_l|}{\sqrt{\gamma R (T_r - |\underline{u}_l|^2 / 2C_p}} << 1.0 \tag{8}$$

then, equations (2) and (3) will represent the governing equations for nearly incompressible flows. Since, in the present work, the melt is considered as nearly incompressible, all the cases investigated in the present work have Mach numbers on the order of 10^{-2}.

Equations (1) through (5) are written in vector form. The specific dependent variables to be determined are the temperatures, pressure, concentration and velocity components in the direction of the cylindrical polar coordinate lines. In addition, the locations of the free surface and melt-crystal interface will be determined along with the solution of the above equations. An important and novel feature of the study is that a time-dependent, generalized coordinate transformation is introduced to accommodate the motion and the shape of the free surface and melt-crystal interface.

2-3. Free Surface Boundary Conditions

The free surface defined here is the interface between the melt and a gas. In this situation, the stress tangential to the surface is approximated as zero. The stress normal to the surface must exactly balance any externally applied normal stress. With surface tension included, the stress conditions are derived from,

$$\sum_{i=1}^{3} n_i \tau_{ij} = \gamma n_j \tag{9}$$

where n_j are the components of the unit vector normal to the surface, τ_{ij} is the stress tensor and γ is the force due to surface tension. For a Newtonian fluid and axisymmetric flow, the stress conditions can be simplified as [38]:

(i) Tangential stress condition (along the azimuthal direction)

$$\frac{\partial}{\partial r}\left(\frac{u_2}{r}\right) n_1 + \frac{\partial u_2}{\partial z} n_3 = 0 \tag{10}$$

(ii) Tangential stress condition (along the radial direction)

$$2 n_1 n_3 \left(\frac{\partial u_1}{\partial r} - \frac{\partial u_3}{\partial z}\right) + \left(n_3^2 - n_1^2\right)\left(\frac{\partial u_1}{\partial z} - \frac{\partial u_3}{\partial r}\right) = \frac{1}{\mu u_0} \frac{\partial \gamma}{\partial \theta}\left(n_3 \frac{\partial \theta}{\partial \gamma} - n_1 \frac{\partial \theta}{\partial z}\right) \tag{11}$$

(iii) Normal stress condition

$$P = P_a - \frac{Fr}{Bo}\left[\frac{\eta''}{(1+\eta'^2)^{3/2}} + \frac{\eta'}{r(1+\eta'^2)^{1/2}}\right] + \frac{2}{Re}\left[\frac{\partial u_1}{\partial r} n_1^2 + \left(\frac{\partial u_3}{\partial r} + \frac{\partial u_1}{\partial z}\right) n_1 n_3 + \frac{\partial u_3}{\partial z} n_3^2\right] \tag{12}$$

where Bo is the Bond number and is defined as $\rho g R_S^2/\gamma$, and determines the ratio of the surface tension to gravational forces, there η is the free surface elevation and η', η'' are first and second derivatives with respect to r, respectively. n_1, n_2, and n_3 are r, ρ, z components of a unit normal vector at the free surface. The stress conditions are also called dynamic conditions because they are the force balance conditions which must be satisfied along the free surface at all times.

In addition to the dynamic conditions, a kinematic constraint is used to determine the position of the free surface. This condition is based upon the constraint that the normal velocity of the fluid at the interface is the same as the normal velocity of the free surface. In Eulerian form, it can be expressed as,

$$\frac{D}{Dt}(\eta - z) = 0 \tag{13}$$

where $\frac{D}{DT}$ is the substantial deriviative [44]. The location of the free interface is determined by time integration of the above equation.

2-4. Velocity Boundary Conditions

Velocity boundary conditions along the melt-crystal interface and crucible wall are also required. Along the melt-crystal interface, 'no-slip' and mass balance conditions are imposed. The 'no-slip' condition implies

$$\underline{u}_l \cdot \tau_l = \underline{u}_p \cdot \tau_i \tag{14}$$

and the mass balance condition is,

$$\rho_l \underline{u}_l \cdot \underline{n}_i = \rho_s \underline{u}_p \cdot \underline{n}_i \tag{15}$$

where $\underline{\tau}_i$, $\underline{n}_i$ are the unit tangential and normal vectors at the melt-solid interface. The velocity boundary conditions along the crucible wall are

$$\underline{u}_l \cdot \tau_c = 0 \qquad \underline{u}_l \cdot n_c = 0 \tag{16}$$

where $\underline{\tau}_c$, $\underline{n}_c$ are the unit tangential and normal vectors at crucible wall, e.g., the tangential vector at the crucible bottom wall is a horizontal vector, while the tangential vector at the crucible side wall is a vertical vector.

A special kind of velocity boundary condition needs to be used at the junction where the moving surface meets the stationary wall. Physically, 'no-slip' conditions should be used at these points; however, it will cause numerical problems if u is zero at the junction. Here, according to the kinematic condition, the surface will never move at these points. Experience teaches that the surface should move according to the rotating boundary conditions. Thus, at points where the moving points meet the crucible side wall, we allow velocities tangential to the walls to slip, and velocities normal to the wall to be 'no slip'. The slip velocities are obtained from the kinematic condition. At every time step, the kinematic conditions are applied at the surface, except at the junction. The location of the surface at the wall is obtained from a linear extrapolation from the interior points.

2-5. Melt-crystal Interface Boundary Conditions

There are two conditions that need to be satisfied along the melt-crystal interface; 1) the temperature must be equal to the equilibrium melting temperature, and 2) the net heat flux across the interface must equal to the latent heat absorbed per unit volume during solidification. The first condition states that the melt-solid interface is a constant temperature surface i.e., $T = T_m$. The second condition can be written into the form of a kinematic condition and used to determine the position of the melt-crystal interface. We will now develop the second condition.

The heat, ΔQ_i, delivered to or removed away from the melt-crystal interface by phase i in a time interval, Δt, can be written as

$$\Delta Q_i = A_n q_{n,i} \Delta t$$

where $q_{n,i}$ is the heat flux normal to the interface and A_n is the cross-sectional area perpendicular to the heat flux. Using Fourier's law for the heat flux, the net heat delivered to the melt-crystal interface is $Q = \Delta Q_\ell - \Delta Q_s$, i.e.,

$$Q = A_{\hat{n}} \Delta \left(k_s \frac{\partial T}{\partial n}\bigg|_s - k_l \frac{\partial T}{\partial n}\bigg|_l \right) \tag{17}$$

where n is the unit normal vector at the melt-crystal interface. Here, heat transported through radiation is ignored. This net heat, according to the law of conservation of energy, should equal to the latent heat gained due to crystallization process which is

$$A_n \Delta\eta^* \rho_m h_{sl} \tag{18}$$

where $\Delta\eta^*$ is the change of interfacial positions in time, Δt; and $h_{s\ell}$ is the latent of crystallization.

Coupling the net heat flux across the interface to the latent heat absorbed yields:

$$\Delta\eta^* = \frac{\Delta t}{\rho_m h_s} \left[k_s \frac{\partial T}{\partial n}\bigg|_s - k_l \frac{\partial T}{\partial n}\bigg|_l \right] \tag{19}$$

To treat equation (19) specifically, we note that for the Cz problem, the crystal is pulled out u_p at a constant velocity (within a reasonable time period), i.e., the melt-crystal interface is rising at a constant rate. If η^* is written as $\Delta\hat{\eta} - \Delta\bar{\eta}$ where $\Delta\bar{\eta}$ is the area averaged change of interfacial positions and $\Delta\hat{\eta}$ accounts for the spatial variations of change of the interfacial positions, then $\Delta\hat{\eta}/\Delta t' = \Delta\eta^*/\Delta t' + \Delta\bar{\eta}/\Delta t'$. Further, if $\Delta t'$ is small, the above quantities can be approximated by time derivatives, then the above equation can be written as

$$\frac{\partial\hat{\eta}}{\partial t} = \frac{1}{\rho_m h_{s\ell}}\left[k_s \frac{\partial T}{\partial n}\bigg|_s - k_\ell \frac{\partial T}{\partial n}\bigg|_\ell\right] + \dot{u}_p \tag{20}$$

where $\frac{\partial\bar{\eta}}{\partial t'} = u_p'$ is the crystal pulling velocity. In nondimensional form,

$$\frac{\partial\eta}{\partial t} = \frac{1}{Pe}\frac{\rho_s T_m}{S\rho_m \Delta T}\left(\frac{\partial\theta}{\partial n}\bigg|_s - k\frac{\partial\theta}{\partial n}\bigg|_\ell\right) + u_p \tag{21}$$

where Pe and S are Peclet and Stefan numbers, respectively. S is defined as $h_{s\ell}/C_{ps}\Delta T$ and k is the ratio of melt thermal conductivity. Note that in crystal growth problems, u_p is the crystal pulling rate which is externally controlled; thus, $\partial\eta/\partial t$ is a measure of nonuniform crystal growth (in both space and time). Furthermore, the shape of the melt-crystal interface is of great interest in crystal growth process control because it affects the distribution of dopants and unwanted impurities in the crystal, and is responsible for residual strains in the crystal.

In the present model, the crystal pulling velocity is determined from integrating equation (21), i.e.,

$$u_p = \frac{1}{2\pi}\frac{\rho_s T_m}{Pe\, S\rho_m \Delta T}\int_0^{2\pi}\int_0^1 r\left(\frac{\partial\theta}{\partial n}\bigg|_s - k\frac{\partial\theta}{\partial n}\bigg|_\ell\right) dr\, d\theta \tag{22}$$

Physically, the crystal pulling velocity is obtained from the volume averaged net heat across the interface. Since we have assumed a constant crystal diameter growth in a steady state situation, the total net heat removed from the melt-crystal structure will be from the heat gained due to crystallization. In steady state calculations, this relation is exact, but in transient calculations, we have assumed the volume average of the non-uniform growth is small.

2-6. Thermal Boundary Conditions

Three types of thermal boundary conditions are involved in our analysis for the liquid and solid phases. They are, 1) constant temperature boundary condition, 2) constant heat flux boundary condition, and 3) constant heat radiation boundary condition. For the liquid phase, constant temperature boundary condition are always applied at the crucible walls and crystal surface. A combination of heat flux and heat radiation boundary conditions can be applied at the free surface. For the solid phase, constant temperature boundary condition is applied at the melt crystal interface. These boundary conditions are outlined next.

1) Constant temperature boundary condition

$$\begin{aligned} &\text{Liquid: } \theta_\ell = \theta_m \text{ at crystal surface} \\ &\qquad\quad\ \theta_\ell = \theta_c \text{ at crucible wall} \\ &\text{Solid: } \theta_s = \theta_m \text{ at melt solid interface} \end{aligned} \tag{23}$$

2) Heat flux condition

Since argon gas is blowing along the crystal surface and free surface, convective heat transfer may be important, thus:

$$\begin{aligned} &\text{Liquid: } \frac{\partial \theta_l}{\partial n} = -k_{gl} Nu(\theta_l - \bar{\theta}_a) \quad \text{at free surface} \\ &\text{Solid: } \frac{\partial \theta_s}{\partial n} = -k_{gs} Nu(\theta_s - \bar{\theta}_a) \quad \text{at crystal surface (above free surface)} \end{aligned} \tag{24}$$

k_{gi} is the ratio of conductivity of the gas to conductivity of Phase i (ℓ or s), Nu is the Nusselt number which is defined as hR_s/k_g where h is the heat transfer coefficient of the gas and k is the thermal conductivity of the gas. θ_a is the ambient temperature. The Nusselt number can be obtained through some empirical relations, e.g. in Appendix B. Note, at the top of crystal, a zero flux condition is used to simulate an infinitely long grown crystal.

3) Heat Radiation Condition

In a crystal growing system involving N surfaces with different emissivities at different temperatures, the mutual radiation interchange is adequately treated by introducing the concept of geometrical shape factor, f_{kj}. In an ideal situation, f_{kj} is 1. The net heat flux radiated from the kth surface is expressed by,

$$q_k = \varepsilon_k \sigma \sum_{\substack{j=1 \\ j\neq k}}^{N} \varepsilon_j f_{kj} (T_k^4 - T_j^4) \tag{25}$$

When considering only the direct radiation interchange, σ is the Stefan-Boltzmann constant, T_j and ϵ_j are the temperature and emissivity of the jth surface. For the present application, we only consider heat radiation from the free surface to the gas (argon) or heat radiation from the crystal surface above the free surface to the gas phase, and assume a constant ambient temperature above the free surface. A better approximation for the ambient temperature can be used if the heat transfer and flow conditions in argon gas are known. The heat flux radiated can be simplified as,

$$-k_i \frac{\partial T}{\partial n} = \sigma \epsilon_i (T^4 - T_a^4) \qquad i = \ell, s$$

Nondimensionalizing the above equation and introducing a Biot number, H, the above equation becomes

$$\frac{\partial \theta}{\partial n} = -\frac{H \Delta T}{(R_c - 1)\, T_m} (\theta^4 - \theta_a^4) \tag{26}$$

where R_c is the nondimensional crucible radius, and H is defined as $\epsilon \sigma R_s T_m{}^3 / k_\ell$.

2-7. Species Boundary Conditions

At the melt-crystal interface, the flux condition on the concentration is,

$$\frac{\partial C_k}{\partial z} - (1 - K_{ok})\, a\, Re^{1/2}\, Sc\, C_k = 0 \tag{27}$$

where K_{ok} is the equilibrium distribution coefficient for species k. The suction parameter, a, is defined as $u_p/\sqrt{(\omega\nu)}$. We have assumed that diffusion into the crystal is negligible. For most species, in Si growth, the coefficient $aRe^{1/2}$ Sc is on the order of 100 with Sc on the order of 50. Numerically, it means a very fine grid must be used near the interface to resolve the boundary layer. Physically, the boundary layer for the convective-diffussive species equation is approximately $Sc^{1/2}$ times thinner than the momentum boundary layer. To reduce computational efforts, we do not resolve the boundary layer of the species equation in the bulk flow calculations. Instead, we use the zero flux condition:

$$\frac{\partial C_k}{\partial n} = 0 \tag{28}$$

To obtain the resolution of the species distribution near the interface, a solute transport submodel has been developed. This submodel makes use of the solution obtained from the 'bulk flow' calculations.

At the crucible walls, as well as the free surface, a zero flux condition is also used. Here we assume the dissolution and vaporization rates at the crucible walls and free surface respectively, are small. In order to calculate the oxygen concentration in the melt, a model for the rate of dissolution and vaporization of oxygen needs to be developed (either from experimental measurements or derived from crucible properties and argon gas flow dynamics). This is beyond the scope of the present effort.

2-8. Species Transport Submodel

It was found [28-32,34] that the behavior of the fluid adjacent to the growing crystal interface is a primary factor in controlling the species uptake to the crystal. In our model, we assume that species diffusion and forced convection (due to rotation of the crystal) are important in a thin region with thickness Δ_c near the melt-crystal interface. Solute impurities in the melt and from the crucible wall are transported by "bulk" flow and reach the boundary of this thin region. The governing equations (2) and (3), can be simplified to a set of ordinary differential equations [33] to provide a flow field for the species equation (5) in this region.

In the thin region, if the natural convection is ignored, the nondimensionalized axisymmetric continuity [2] and Navier-Stokes equations [3] can be reduced to the following system of equations [33].

$$2F + \frac{\partial H}{\partial \zeta} = 0 \tag{29}$$

$$F^2 - G^2 + H\frac{\partial F}{\partial \zeta} - \frac{\partial^2 F}{\partial \zeta^2} = 0 \tag{30}$$

$$2FG + H\frac{\partial G}{\partial \zeta} - \frac{\partial^2 G}{\partial \zeta^2} = 0 \tag{31}$$

$$H\frac{\partial H}{\partial \zeta} + \frac{\partial B}{\partial \zeta} - \frac{\partial^2 H}{\partial \zeta^2} = 0 \tag{32}$$

where equation (29) is the continuity equation. Here equation (30) through (32) are the three components of Navier-Stokes equation and $u = r\omega F$, $v = r\omega G$, $w = H\surd(\nu\omega)$, $P = \rho B\surd(\omega\nu)$, $\zeta = z\surd(\omega\nu)$ with the following boundary conditions:

1) at $\zeta = \eta_o$: $F = 0$, $G = 1$, $H = a$, $B = 0$

2) at $\zeta = \eta_o{}^{-5}\delta_m$; $F = G = 0$

Where η_o is the axial position of the interface and δ_m is the momentum boundary layer thickness, a is the suction parameter as defined earlier. The solution to the above equations depends on the suction parameter, i.e., for a given suction parameter the flow field can be calculated once and used for various species calculations.

To obtain better numerical resolution in both radial and axial direction, the species concentration, equation (5) in steady state, is nondimensinalized by two reference lengths. The axial distance is nondimensionalized by the crystal radius while the axial distance is nondimensionalized by U_p/D. The resulting equation in steady cylindrical polar coordinates is,

$$\frac{1}{a^2 Sc}\frac{1}{r'}\frac{\partial}{\partial r'}(r' u' C_k) + \frac{\partial}{\partial \zeta}(w' C_k) = \frac{1}{a^2 Sc^2 Re}\frac{1}{r'}\frac{\partial}{\partial r'}\left(r' \frac{\partial C_k}{\partial r'}\right) + \frac{\partial^2 C_k}{\partial \zeta'^2} \quad (33)$$

with boundary condition:

1) $\dfrac{\partial C_k}{\partial \zeta'} - (1 - K_{ok}) = 0$ at $\zeta' = \eta_o \dfrac{u_p}{D}$

2) $C_k = C_{\ell k}(r')$ at $\zeta' = (\eta_o - Sc)\dfrac{u_p}{D}$

3) $\dfrac{\partial C_k}{\partial r'} = 0$ at $r' = 0$

4) $\dfrac{\partial^2 C_k}{\partial r'^2} = 0$ at $r' = 1$

where $w' = w/u_p' = H(\zeta)/a$, $u' = u/R_s\omega$, $\zeta' = zu_p'/D = aSc\zeta$, $r' = r/R_s$. $C_{1k}(r')$ is the species concentration at the lower boundary of the thin layer region for specie k, and must be matched with the values obtained from "bulk" flow calculations. If C_{1k} is a constant, the solution for C_k reduces to one dimensional solutions.

3. NUMERICAL ANALYSIS

3-1. Introduction

The numerical procedure used to solved the governing equations is a consistently split linearized block implicit scheme originally developed by Briley and McDonald [35] and embodied in a computer code termed MINT, an acronym for Multidimensional Implicit Nonlinear Time-Dependent. The basic algorithm has been further developed and applied to both laminar and turbulent flows. Since the scheme has been described in detail in several publications available in the open literature, it will not be detailed here. Rather only a brief outline of the procedure will be given in the following:

The governing equations are replaced by an implicit time difference approximation, optionally a backward difference or Crank-Nicolson scheme. Terms involving nonlinearities at the implicit time level are linearized by Taylor series expansion about the solution at the known time level, and spatial difference approximations are introduced. The result is a system of multidimensional coupled (but linear) difference equations for the dependent variables at the unknown or implicit time level. To solve these difference equations, the Douglas-Gunn procedure for generating alternating-direction implicit (ADI) splitting schemes as perturbations of fundamental implicit difference schemes is introduced in its natural extension to systems of partial differential equations. This ADI splitting technique leads to systems of coupled linear difference equations having narrow block-banded matrix structures which can be solved efficiently by standard block-elimination methods.

The method centers around the use of a formal linearization technique adapted for the integration of initial-value problems. The linearization technique, which requires an implicit solution procedure, permits the solution of coupled nonlinear equations in one space dimension (to the requisite degree of accuracy) by a one-step noniterative scheme. Since no iteration is required to compute the solution for a single time step, and since only moderate effort is required for solution of the implicit difference equations, the method is computationally efficient; this efficiency is retained for multidimensional problems by using ADI matrix splitting techniques. The method is also economical in terms of computer storage, in its present form requiring only two time levels of storage for each dependent variable. Furthermore, the splitting technique reduces multidimensional problems to sequences of calculations which are one-dimensional in the sense that easily-solved narrow block-banded matrices associated with one-dimensional rows of grid points are produced. Consequently, only these one-dimensional problems required rapid access storage at any given stage of the solution procedure, and the remaining flow variables can be saved on auxiliary storage devices if desired. Since each one dimensional split of the matrix produces a consistent approximation to the original system of partial differential equations, the scheme is termed a consistently split linearized block implicit scheme. Consistent splitting has been shown by a number of authors [36] to considerably simplify the application of the intermediate split boundary conditions.

The present work involved an extension of the LBI scheme : in every time step, a boundary fitted coordinate system is constructed to accommodate the time dependent characteristic of the free surface and melt-crystal interface. A simple Eulerian height function is used to represent the free surface and the melt-crystal interface. This function is defined as the distance from a reference line and is obtained from the kinematic conditions equation (12) and equation (14). The computational domain is shown in figure 3.1.1.

For numerical calculations, the height function is discretized into points sometime called markers. These markers are then used to define the time dependent boundaries. Since a boundary fitted coordinate system is used, the boundary is part of the grid system at all times. For this reason, flow variables at the moving boundary are well defined and application of the boundary conditions at these boundaries is straightforward.

The numerical procedure can be summarized in four steps: 1) the governing equations of each phase and their corresponding boundary conditions are transformed into a boundary fitted coordinate system according to the shapes of the interfaces; 2) the equations of each phase are solved in the transformed coordinates using the LBI scheme; 3) interfacial positions (include free interface and melt-crystal interface) are advanced using the kinematic conditions, and 4) advance time step and repeat the sequence. A flow chart for the present numerical scheme is shown in figure 3.1.2.

3-2. Transient Capability

The solution algorithm for iterative solution of steady solutions has been written as the following split LBI scheme (equations A-8)

$$(A - \beta \Delta t L_1^n)(\phi^* - \phi^n) = \Delta t \ (D^n + S^n) \tag{34a}$$

$$(A - \beta \Delta t L_2^n)(\phi^{**} - \phi^n) = A \ (\phi^* + \phi^n) \tag{34b}$$

$$(A - \beta \Delta t L_3^n)(\phi^{n+1} - \phi^n) = A \ (\phi^{**} + \phi^n) \tag{34c}$$

which is an ADI scheme to approximate the linearized unsplit scheme (equation A-6).

$$(A - \beta \Delta t L^n)(\phi^{n+1} - \phi^n) = \Delta t \ (D^n + S^n) \tag{35}$$

to second order in Δt. Combining equations (34a) through (34c) gives

$$(A - \beta \Delta t L_1^n) \ A^{-1} (A - \beta \Delta t L_2^n) \ A^{-1} (A - \beta \Delta t L_3^n)(\phi^{n+1} - \phi^n) = \Delta t \ (D^n + S^n) \tag{36}$$

A comparison of equations (35) and (36) shows that splitting error terms such as

$$(\beta \Delta t)^2 \ L_1 A^{-1} L_2 (\phi^{n+1} - \phi^n) \tag{37}$$

arise due to the ADI scheme. Although these splitting error terms vanish for a steady solution (since $\phi^{n+1} = \phi^n$), they do affect transient accuracy in unsteady applications. The term (equation (37)) is of second order in Δt and, hence, does not lower the formal accuracy from that of equation (35). However, the error term (equation (37)) has a different functional form from the truncation error of the unsplit scheme, and when matrices such as A^{-1} are stiff (i.e., widely differing eigenvalues), the splitting error can cause large errors in transient solutions. Stiffness in the matrix A^{-1} occurs at near incompressible Mach numbers.

The splitting error can be removed by iterating at each time step. One method of iterating is to replace ϕ^{n+1} by $\phi^k + \delta\phi^k$ in the unsplit scheme (35), divide by Δt, and add an artificial time derivative approximation $\tilde{A}\,\Delta\phi^k/\Delta\tau$ to equation (35). Here, k is the iteration index, $\Delta\tau$ is an artificial time step, and A may be chosen to be different from A. The result can be written

$$\left(\frac{\tilde{A}^n}{\Delta\tau} + \frac{A^n}{\Delta t} - \beta L^n\right)\Delta\phi^k = D^n + S^n - \left(\frac{A^n}{\Delta t} - \beta L^n\right)(\phi^k - \phi^n) \tag{38}$$

A Douglas-Gunn type of splitting is introduced, and the result can be written as

$$(B - \beta L_1^n)\,\Delta\phi^* = \text{RHS of Eq.(38)} \tag{39a}$$

$$(B - \beta L_2^n)\,\Delta\phi^{**} = B\,\Delta\phi^* \tag{39b}$$

$$(B - \beta L_3^n)\,\Delta\phi^k = B\,\Delta\phi^{**} \tag{39c}$$

where $B = \tilde{A}^n/\Delta\tau + A^n/\Delta t$.

Note that when the iteration equations (39a) through (39c) converges to a steady solution ($\Delta\phi^k \rightarrow 0$) then $\phi^k \rightarrow \phi^{n+1}$, and the steady solution satisfies the linearized unsplit scheme (equation (35)). The steady solution is independent of A and $\Delta\tau$, and these quantities can be chosen to obtain rapid convergence. The matrix conditioning technique of [36] can be employed for low Mach number calculations, and then A is replaced by A multiplied by a diagonal conditioning matrix.

Since an iteration is being performed at each time step, there is the option of updating the time linerizations which were used in equation (35). In this case, equation (38) is replaced by

$$\left(\frac{\tilde{A}^k}{\Delta\tau} + \frac{A^k}{\Delta t} - \beta L^k\right)\Delta\phi^k = \beta(D + S)^k + (1 - \beta)(D + S)^n - \frac{H(\phi^k) - H(\phi^n)}{\Delta t} \tag{40}$$

and split in the same manner as equations (39a) through (39c).

If equation (40) is used, then the converged solution will satisfy the nonlinear implicit scheme

$$[H(\phi^{n+1}) - H(\phi^{n})] \ / \ \Delta t = \beta (D + S)^{n+1} + (1 - \beta)(D + S)^{n} \tag{41}$$

Test calculations have been performed using equations (39a) through (39c) on simple problems, and it was found that convergence at each time step can be obtained in approximately 3 to 15 iterations, depending on the physical time step used. Fewer iterations are required as the physical time step Δt is reduced.

3-3. Body-Fitted Coordinate Transformation

The numerical solution of the Navier-Stokes equations for problems with a moving boundary is complicated by the need to simultaneously compute both the flow field and the time-dependent boundary location as the calculation proceeds in time. In calculations of this type, stress conditions or heat flux conditions are applied along the time dependent boundaries. A time-dependent body-fitted coordinate system is therefore most suitable and chosen for the present studies, because stress conditions and heat flux conditions can be specified along the coordinate lines.

Body-fitted coordinate systems avoid the need for irregular shaped finite difference computational cells at computational boundaries thereby alleviating the complex computer coding problems associated with irregular shaped cells. In addition, spatial truncation error associated with irregular finite difference cells is avoided by the use of body-fitted coordinates.

Various approaches are available for generating body-fitted coordinates, although in general they can be categorized into two generic groups - algebraic and elliptic method. Algebraic methods have the advantage of being conceptually simple for complex boundary geometries. However, it is often necessary to establish suitable functional forms for each family of coordinates for each new configuration. The main advantage of elliptic generation is that the method is applicable to complex geometries without the need to modify the basic approach for each new configuration.

In the present work, an algebraic method is used for all calculations except the case with a mensicus. In the meniscus case, elliptic methods based on the work of Thompson and his coworkers [39,40] are used. We discuss both methods below:

In algebraic method, the time-dependent non-orthogonal coordinate transformation is given by

$$r = f(\xi) \qquad \theta = h(\chi)$$

$$z = \eta(r, \theta, t) \int_1^{\zeta} g(\xi, t) \, d\xi$$

where ζ, χ and ξ are computational coordinates in the r and z directions, respectively. $f(\xi)$, $h(\chi)$ are grid packing transformation developed by Levy and Gibeling [41] which have the form of hyperbolic tangent function. And

$$g(\zeta, t) = \beta_o + \frac{1}{2} \sum_{i=1}^{N} \left[\beta_i \; \mathrm{erfc} \left(\frac{2.326}{\alpha_i} (\zeta - \gamma_i) \right) - (1 + \mathrm{sign}(\alpha_i)) \right]$$

is a grid distribution generator originated by Oh [42], in which the complementary error function is used and β_o, β_i, γ_i, α_i are grid parameters whose values can be made time dependent.

In the present study, the grid parameters are constants in time and are chosen such that grids are packed at the regions where the flow (and/or temperature) field changes most rapidly. Since $F(\xi)$, $H(\chi)$ are constant in time, the grid spacings in the r and θ direction do not change in time despite the motion of the free surface and interface. The grid spacings in the axial direction depend on the instantaneous locations of the free surface and melt-crystal interface.

The above way to constrain grids is simple, especially in the present application where the slope of the free surface and interface never becomes infinite. However, in the case of a menicus, the contact angle is usually close to 90° (i.e., the free surface near the crystal is close to being vertical). In this case, the algebraic method mentioned above will produce collapsing r and z coordinate lines which is not very desirable. To avoid this, we use elliptic methods [43] to generate grids for the case with mensicus.

3-4. <u>CRAY Vectorization</u>

It is important to realize that any application program will probably execute faster and be able to solve larger problems when transferred to a super computer, e.g., CRAY-1S, CRAY X-MP. This is due to the fact that super computers technology makes use of short cycle times (in the nanosecond range) and large memories (in the Mword range). However, in many applications, an order of magnitude reduction in execution time may be obtained by paying attention to the vectorization of the code.

The extra speed-up is obtained by optimally utilizing the vector processing capabilities of the machine. In today's class VI super computers, areas which have a direct impact on the performance of algorithms are as follows:

a) Vector functional units = the vector functional units in super computer improve upon this performance by using pipeline vector arithmetic. In order to utilize the arithmetic pipelines, data has to be organized so that a steady stream of operands can be supplied. Organizing the operands into vectors is one way to do this. The longer the vectors are, the more efficient the pipelines can be utilized.

b) Interface of vector units with memory = the pipelined functional units which perform the vector arithmetic, require a continuous stream of operands to arrive at the pipeline in order to achieve optimal performance. From the programmer point of view, it is advantageous to reorganize (if possible) a computational method involving two dimensional arrays so that the array is processed in a column-wise fashion.

The numerical code MINT has been under vectorization during this Phase II program and partial vectorization was achieved. In the partly vectorized code, (the version that was used through out these studies), the run time was improved by 12.8% over the unvectorized version.

4. CALCULATIONS

4-1. Introduction

Considerable effort during the Phase II study was devoted to code development for purposes of extending the state-of-the-art CZ studies to include self-consistently determined shape of the melt-crystal interface. In the interest of efficient use of computer resources, initial test runs for these calculations were performed with values of dimensionless parameters chosen primarily for computational resources. Calculations with parameters relevant to silicon are discussed in Sections 5 and 6.

a) Preliminary Test of Free Surface Algorithms

Preliminary calculations were performed to check of free surface algorithm for the rotating fluid. The configuration is the same as shown in Figure 3.1.1 except the crystal is absent. In this calculation, dimensional parameters are normalized by the crucible radius and it's rotating velocity. Analytical solutions with linearized free surface boundary conditions are available [44] for qualitative comparison.

Initially, the free surface is planar and the fluid is quiescent with the crucible rotating along the axis of symmetry. The number of grid points used was 26 x 11 and are packed near the wall and free surface (as shown in Figure 4.1.1a).

Grids become nonorthogonal when the free surface deforms because coordinate lines are constructed every time step according to the current shape of the free surface.

A steady state solution was obtained after 80 time steps. As shown in Figure 4.1.1 the shape of the free surface is parabolic. Linear theory [44] provides,

$$V = \Omega r \quad ; \quad u = w = 0$$

$$\eta = \eta_o + \frac{1}{2} Fr\, r^2$$

where u and w are radial and axial velocities respectively. The tangential zero shear stress condition is satisfied only if the shape of the free surface is nearly planar, i.e. small Fr. In our calculations, which are fully nonlinear, $Fr = 0.5$, and $\omega = 1$. Consequently, discrepancies on the shape of the free surface and azimuthel velocity near the free surface are anticipated. Maximum differences of 3% for the free surface location was found at $r = 0.6$. The contour lines for v (Figure 4.1.1b) near the free surface are perpendicular indicating zero tangential stress.

A second preliminary calculation was performed to check the algorithm for the case of axisymmetric flow in a rotating crucible with a counter-rotating crystal. This calculation is considered important because the algorithm was substantially generalized after the Phase I effort, see e.g., Liu et.al [37].

The calculations were performed on a grid containing 26 radial points and 14 axial points. The solution converged to a steady solution within 80 time steps. While the Reynolds number used is 100, and is considered low in Cz processes, it serves the purpose of verifying the code. Figure 4.1.2a shows the configuration of the coordinate. Grids points are packed horizontally at regions near the free surface and the rotating crystal. Grid points are packed vertically at regions below the junction of the free surface and rotating crystal, and near the crucible wall. Numerical calculations of the velocity distribution (or field) are shown in Figure 4.1.2b and Figure 4.1.2c and show good qualitative agreement with Liu, et.al., [37].

The computer code used in the present study is based on the linearized block-implicit solution procedure (LBI) for compressible Navier-Stokes equations developed by Briley and McDonald [35]. In the present development, the temperature in the solid phase, which is coupled to the fluid through the interfacial shape and heat flux, is solved for simultaneously with the fluid conservation equations. For this reason, a stand-alone LBI scheme for the transient heat conduction equation in cylindical planar coordinate with moving boundary at the axial direction was developed.

b) Preliminary Test of Transient Conduction Solver

The next two examples are devoted to test the stand-alone LBI solution procedures. The first example is that of a semi-infinite cylinder immersed in a hot bath. The boundary conditions are shown in 4.1.3a. For this problem, analytical solution exists and are obtained from Carslaw and Jaeger [45] as

$$\theta_s = 1 - 2 \sum_{n=1}^{\infty} \exp(-\beta_n^2 t) \frac{Jo(\beta_n r)}{\beta_n J_1(\beta_n)}$$

where β_n, n = 1,2 are the roots of Bessel's function.

$$Jo(\beta_n) = 0$$

(Note, do not confuse β_n with the volumetric expansion coefficient.) Figure 4.1.3b shows the comparison between the numerical and analytical results.

Excellent agreement is obtained. The number of grid points used was 21 x 10 and Δt is 0.2. The CPU on CRAY-1 is 0.22 msec per time step per mesh point. In this calculation, steady state, as well as transient solutions for the conduction equation are obtained and were verified with analytical solution.

The next calculation performed was to verify the stand-alone LBI procedure with moving boundary conditions. The boundary and initial conditions are shown in Figure 4.1.4a. Initially, the temperature field θ_s and moving surface at X = -1 are obtained from analytical solution. In every time step the moving surface which is obtained from analytical solution is used as the boundary location for the stand-alone LBI procedure. The numerical solutions can be compared to solutions to the one dimensional analytical transient heat conduction equation and solidification surface, as given by Carslaw and Jaeger [45].

$$\theta_s = \frac{1}{\mathrm{erf}\,(0.5)} \mathrm{erf}\left(\frac{-r}{2\sqrt{t}}\right) \qquad X = -\sqrt{t}$$

The computed temperature field is then compared with the analytical solution every time step. Figure 4.1.4b shows the difference between the numerical and analytical solutions at $t = 2.2$. The maximum error is 2×10^{-4} occurring at the middle of computational domain. The number of grid points is 5 x 42 and Δt used is 0.05.

4-2. Group I - Studies of Melt Dynamics

The purpose of this group of calculations is to study the hydrodynamics of the melt under various rotational conditions and with different crystal immersion depths. The response of free surface under these conditions is also investigated. All dimensionless numbers in this group of calculations were chosen for computational purposes, they are not relevant to silicon. Further, in all Phase II studies the crystal immersion depth, δo, is prespecified, and fixed in time and space. This approximation simplifies the modeling at the junction of the melt-solid interface and at the melt-free surface interface. Isothermal conditions are assumed for the solid and fluid phases are assumed in this group of calculations, i.e., the energy conservation equations for both phases are not solved Three examples, with different rotational conditions, ω, and immersed length, δo, are chosen as representative in this group. In this group of calculations, the Reynolds number and Froude number are chosen to be 100 and 0.5, respectively. Table 4.2.1 shows the difference of parameters chosen for the three examples.

i) Run T1-1

The first example is for a rotating crystal immersed in a stationary crucible, i.e. $\omega = o$. Recall, the dimensionless crystal rotation is -1. The crystal is immersed in the melt with $\delta o = 0.75$. Grid points are packed into the region below the free surface and near the crystal corner. The number of grid points are 26 x 23. Figure 4.2.1 shows results at steady state; a) coordinates configuration, b) secondary flow pattern, and c) azimuthal velocity.

The shape of the free surface is convex up which qualitatively agrees with the linear solution for rotating cylinder. Forced convection is created due to rotation of crystal and is shown in Figure 4.2.1b. The azimuthal velocity shown in Figure 4.2.1c indicates diffusion of momentum which is generated by the rotating crystal.

ii) Run T1-2

This run is performed for the parameters of T1-1 with the addition of a counter rotating crucible. Here $\omega = -0.68$ which means the crucible is counter rotating 0.68 times slower than the crystal. With this parameter change, the forced convection phenomena and shape of the free surface are also changed. The shape of the free surface is convex up near the crystal due to rotation of crystal and is concave up near the crucible wall due to rotation of crucible. Again, the shape of free surface is in good qualitative agreement with the linear solution for counter rotating concentric cylinders. Vortices are generated due to rotating surfaces. Note that the positions of the centers of the vortices depend on the relative (is it relative or the actual magnitudes) magnitudes of the rotations, i.e., ω. Azimuthal velocity is shown in Figure 4.2.2c. Also, note that there is a region within the melt separation two counter rotating fluids.

iii) Run T1-3

This run is performed for the parameters of T1-2 with one change, the crystal is immersed further into the melt, $\delta o = 0.25$. A similar shape of the free surface is found. Location of vortices are changed due to geometric differences. Note, with the crystal further immersed into the melt, more surface area is available to generate shear momentum at the crystal radius. This can be seen from the plot of azimuthal flow. Contour lines are pushed further towards the crucible wall. In other words, the effects of crystal rotation is larger in this case than in the previous case.

For all the calculations with free surface, normal velocities along the free surface are monitored in every time step. They are represented by their averages value and R.M.S. value over the free surface in every time step and are plotted in Figure 4.2.4. The vanishing of the R.M.S. value of the normal velocities serves as a criteria of reaching steady state solution.

With regard to computational efficiency, for this group of calculations (solving the continuity and Navier-Stokes equations of the fluid phase) the CPU on a CRAY-1 is 2.6 msec per time step per mesh point.

4-3. Group II - Studies of Melt Thermohydraulic

In this group of calculations, energy conservation together with the Navier-Stokes and continuity for the fluid phase are solved. Again, dimensionless numbers are chosen with respect to computational conditions. A total of eight examples are performed. The energy equation for the crystal phase is not solved in this group of studies.

Five examples are performed with planar free surface and planar melt-crystal interface. They were performed to develop an understanding of the phenomena caused by temperature driven flow. Effects due to buoyancy, Prandlt number and heat radiation boundary conditions are studied in these five calculations. The shape of the melt-crystal interface and its associated phenomena are studied in the next two calculations, and the interaction with the solid phase forms the last study of this group. Table 4.3.1. shows the parameters used in this group of calculations.

i) Runs T2-1, T2-2, T2-3

Examples with different Grashof numbers (or nondimensional thermal expansion coefficients) are used to study the transition of forced convection to free convection. And for reference comparison is made to run T1-2. In these calculations, crystal and crucible are counter-rotating with $\omega = -0.68$ and the height of the crystal is $\delta_o = -0.75$. With the Boussineq's approximation for the density, the set of conservation equations are coupled through the gravity force term. The Prandtl number used for these runs is 0.054. Run T2-1 to T2-3 indicate cases from forced convection to free convection, as determined by the choice of β equation (7), which are respectively 0, 10 and 25 (which corresponds to Gr = 0, 1.0×10^4, 2.6×10^4). Run T1-2 is identical to T2-1, except that energy equation is also solved in the latter case. Identical results for consequences of the fact that the energy equation is decoupled from the momentum equation (β_0). (Note: In solving this problem, the energy momentum equations are treated as coupled equations). In Run T2-2, β is finite and energy and moments equation are coupled, mixed free-forced convection is found. The fluid has a stronger vertical component near the wall. In Run T2-3, the free convection is stronger than the forced convection. The vortex which was found under the crystal in last runs disappears. The fluid under the crystal reverses direction. When the forced convection dominates fluid is pumped out by the centrifical force; when free convection dominates, fluid is moved toward the center by buoyancy forces.

For cases with rotating crystal in a stationary crucible, free convection is dominant if [14]

$$\frac{Gr}{Re^{2.5}} = 0.1$$

In our case, with counter rotating crystal and crucible, a similar criteria is found to be

$$\frac{Gr}{Re^{25}} = 0.2$$

Note that the temperature fields are also affected by changes of heat transfer mechanism. The differences are not large because of the choice of Prandtl number. For small Prandtl number, the heat transfer mechanism is dominated by heat conduction.

ii) Run T2-4

The purpose of this run is to study the effects of Prandlt number. This run is identical to T2-2, except that Prandlt number (see equation (4)) is increased to 1.0. In run T2-2, heat transfer is mainly due to conduction as can be seen from the uniformity of the temperature contours. Figure 4.3.4c shows the temperature contours of Run T2-4 are lower than those in Run T2-2, because convection effects play a more important role for case with larger Prandlt number.

iii) Run T2-5

Heat radiation is imposed at the free surface (H-10) to study the temperature effects on the fluid. A constant ambient temperature of 1.026 is assumed above the free surface. Runs T2-5 and T2-4 differ in that the latter permits heat radiation at the free surface. It is found that the temperature below the crystal is lower than that in run T2-4 (see figure 4.3.5). The difference is direct: the position of temperature contours under the free surface vary according to the choice of ambient temperature.

iv) Run T2-6

Run T2-6 is performed to study the effects due to free surface conditions with the same conditions as in Run T2-5. These conditions are: a) counter rotating crystal and crucible, $\omega = -0.68$, b) mixed forced-free convections, $\beta = 10$,

c) heat radiation boundary condition at the free surface, H=10, d) large Prandlt number, Pr = 1.0. For comparison of the free surface the results of run T1-2 are also useful.

The shape of the free surface found in this run is concave down (see figure 4.3.6) near the crystal surface, while it is convex up in run T1-2. This is because fluid with lower temperature is carried downward near the crystal surface. The general shapes of the free surface near the crucible are the same in these two runs. By allowing the free surface to deform, the maximum magnitude of secondary flow is larger than the case in T2-5. Consequently, more heat is being carried down below the crystal. The result is that the temperature below the melt-crystal interface is lower than those in run T2-5. Differences in temperature in this region will influence the local formation of melt-crystal interface, as will be shown in the next calculation. Below the crystal, azimuthal velocities from run T2-5 and present run are also different, due to differences of magnitudes of secondary flow. Figure 4.3.7 shows the R.M.S. values of the normal velocities of the free surface as a function of time. Steady state is reached when the normal velocities of the free surface are zero.

v) Run T2-7

In this calculation the temperature field of the crystal phase is assumed uniform and at melt temperature as in T2-1 to T2-6. However, here the melt-crystal interface is allowed to deform according to the kinematic condition. This assumption is valid if the temperature gradient normal the interface is small. All other conditions are identical to the last run (T2-6). The dimensionless parameters for this calculation are S = 22, Pe = 0.1, K = 1 . Indeed, depending upon the choice of parameters, the shape of the melt-solid interface will deform into concave or convex. Figure 4.3.8 shows the results at steady state. The differences in flow field and temperature field indicate the effect due to the deformation of the melt-solid interface.

This calculation is the first to show the distortion of the melt crystal interface due to the thermal-hydralics of the melt. There are two distinct vorticity patterns as revealed by the secondary flow calculations. The fluid is being drawn to the center of the crystal and then thrown out radially. The fluid is transporting the heat away from the axis of symmetry. There is a counter transport of heat arising from the counter-rotating crucible. The dip in the crystal interface occurs near the highest temperature zone of the melt. Also note from the azimuthal distribution that more of the melt is rotating with the crystal, than that experienced with the imposed flat interface.

4-4. Group III - Studies of Species Transport Near the Interface

As discussed in Section 2-8 and repeated here that the behavior of the fluid adjacent to the growing crystal interface is a primary factor in controlling the species uptake to the crystal. In our model, we assume that species diffusion and forced convection (due to rotation of the crystal) are important in a thin region with thickness Δ_c near the melt-crystal interface. Solute impurities in the melt and from the crucible wall are transported by "bulk" flow and reach the boundary of this thin region. The governing equations (2) and (3), can be simplified to a set of ordinary differential equations [33] to provide a flow field for the species equation (5) in this region.

The solution to the set of coupled ordinary differential equations equation (29) through (32) is a function of suction parameter, a, and the boundary conditions at $\zeta = \zeta_2$, where ζ is the nondimensional thickness of the layer. Theoretically, in the case of a finite diameter disk rotating in an infinite fluid, the radial and azimuthal velocities will decay to zero as $\zeta = \infty$. However, in practice, as shown in Schlichting [3] (with a=o), the radial and azimuthal velocities decay asymptotically to zero on distance of within $4\sqrt{(\nu/\omega)}$, i.e., $|\zeta_0 - \zeta_2| = 4$.

There are two approaches to handle the bottom velocity boundary conditions: In the first approach, we extend the thin layer region to a fictitious length (i.e., $\zeta = \zeta_2$ = some large value), and apply zero velocity condition there. This condition was shown to be consistent with the velocities of the bulk flow calculation obtained from the set of ordinary differential equations at the point ζ_1, where $\zeta_2<\zeta_1<\zeta_0$. In the second approach, we find ζ_1 $F(\zeta_1)$, $G(\zeta_1)$ from the bulk flow calculations and use them as boundary conditions for the set of ordinary differential equations.

The first approach is used in the Case 1 study. The fictitious length is arbitrarily taken to be 5 (>4). The zero condition i.e., $F(-5) = G(-5) = 0$ is applied at ζ_2. The solution to the set of ordinary differential equations in this case is shown in Figure 4.4.1. The second approach is used in the Case 2 study. The thickness of the thin layer $|\zeta_0 - \zeta_1|$ is obtained from bulk flow calculations, and is obtained when the radial velocity exhibits a maximum as it is searched axially downward from the interface. $F(\zeta_1)$, $G(\zeta_1)$ are then obtained by averaging u and v in the radial direction, respectively. It is found that $\zeta_1 = 0.83$ and $F(\zeta_1) = 0.16$, $G(\zeta_1) = 0.58$. Results with this condition are shown in Figure 4.4.2. The suction parameter is taken to be zero in both cases. By comparing the results from Cases 1 and 2, we find that the solution to the set of ordinary differential equation using the first approach matches the solution from the bulk flow calculations for $\zeta_1<\zeta<\zeta_0$, where $\zeta_1\approx-1$ and valid at the approximation used. Physically, it means that the fluid characteristic within $\sqrt{(\nu/\omega)}$ away from the melt-crystal interface can be described using the assumption of the thin layer model.

By assuming that the amount of solute impurities is small, i.e., the solute redistribution does not affect melt hydrodynamics, the convective-diffusive species equation can be decoupled from the melt hydrodynamics equation. In the following analysis for the species distribution, we will first use one dimensional approximation to compare our results with those obtained by previous investigators. To predict species radial impurities, a two dimensional equation together with bulk flow solution are used.

a) One-Dimensional Species Distribution

The one-dimensional governing equation for the species distribution is obtained by simplying equation (33), i.e.,

$$w' \frac{\partial C}{\partial \zeta'} = \frac{\partial^2 C}{\partial \zeta'^2}$$

with boundary conditions, $\frac{\partial C}{\partial \zeta'} - (1 - k_o) C = 0 \qquad \text{at } \zeta' = \zeta'_o$

$$C = C_L \qquad \text{at } \zeta' = \zeta'_c$$

The nondimensional velocity w' is obtained from the solution of two dimensional axisymmetric flow equations (29) through (32). Here, ζ'_0 is the location of the interface and can conveniently be taken to be 0, and ζ'_c is equal to $aSc\zeta_c$, where $\zeta'_1<\zeta'_c<\zeta'_0$. Within the range of parameters (a, k_o, Sc) for silicon crystal growth, we found that C approaches C_L if $|\zeta'_c|>$ aSc. In the following calculations, $|\zeta'_c|$ is taken to be 2aSc- a longer computational domain than necessary. This is chosen to ensure that the downstream boundary condition do not influence the upstream condition (in this case, C at the interface). There are various materials (with different k_o) in the melt and calculations were performed to cover the range of k_o from 0.0004(In) to 1.4 (O). Figure 4.4.3 shows the solute distribution in the melt for various k_o using the axial flow field obtained from Case 1. Figure 4.4.4 shows the solute distribution in the melt for various k_o using the axial flow field obtained from Case 2. In this case, ζ'_c = 0.83 aSc.

From the crystal grower's point-of-view, solute impurities distribution in the melt is of less interest. It is more desirable that the solute impurities level in the crystal are known. Here a commonly used parameter is the effective distribution coefficients, k_{eff}, $k_o\, C_o/C_L$, where k_o is the equilibrium distribution coefficient defined as:

$$k_o \equiv \frac{\text{concentration of the species in the crystal at the interface}}{\text{concentration of the species in the melt at the interface}}$$

k_o is usually taken from the phase diagram. The k_{eff} is then a measure of concentration level of a particular specie in the crystal if the concentration level in the melt is known. According to Burton, et al. (BPS) [28], k_{eff} can be written as,

$$k_{eff} = \frac{k_o}{k_o + (1 - k_o)\exp(-\Delta)}$$

where $\Delta = -\ln[1 \quad aSc\int_0^\infty \exp(-\int_0^\xi Sc\, H\, d\zeta)\, d\xi]$

$$= -\ln[1 - aSc\,\mathcal{F}(a, Sc)]$$

BPS' expression for k_{eff} is exact with respect to the one dimensional solute conservation equation and boundary conditions. The function F(a,Sc) depends on the hydrodynamics of the melt (i.e., $H(\zeta')$) and can be obtained by numerical methods. Table 4.4.1 shows numerical correlations for Δ obtained by previous investigators. Their relations are limited to small values of $aSc^{2/3}$ or $(aSc^{1/2})$. For a particular value of a and Sc, 9 different values of k_o (ranging from 0.0004 to 1.4) are used to determine the solute concentrations at the interface, i.e., k_{eff} are known ($k_{eff} = k_o C_o/C_L$). From BPS' expression for k_{eff}, a set of Δ (for each k_o) is obtained. Δs are then averaged and a data point is generated for that particular a and Sc. Within the range of parameters for silicon crystal growth, we used various suction parameters, a, (from 0.0005 to 0.1) and Schmidt numbers, Sc, (from 10 to 54) to determine C_o and consequently k_{eff}. From the numerical data we are able to find a numerical expression for F(a,Sc);

$$\Delta = - \ln [1 - aSc (\frac{a}{2} + 2Sc^{-0.375} \exp (- 1.52\ aSc^{0.55}))]$$

This formula can be reduced to the BPS correlation for small $aSc^{2/3}$. Figure 4.4.5 shows the comparison of our empirical relations with others. The comparison is good.

b. Two Dimensional Species Distribution

In the last section, we assumed that the radial variation of species distribution is small compared to the axial variation. In this section we do not make this assumption i.e., the two dimensional axisymmetric species equation (33) is used for the numerical calculations. The radial and axial velocities of the melt are obtained from the solution of the reduced Navier-Stokes equations (29) through (32). The solute distribution level C_L (r') at $\zeta' = aSc$, which is the boundary condition, is needed and obtained from the solution of the 'bulk' flow calculations equation (5). Two calculations are performed to validate the computer code.

The first calculations assumed $C_L(r')$ at $\zeta' = aSc$ be a constant. The purpose of this calculations is to show that calculations using a two dimensional equation should reproduce the results of the calculations using the one dimensional equation if the axial boundary conditions do not vary in the radial direction. The result is shown in Figure 4.4.6. In this case we used a = 0.05, Sc = 53 and k_o = 0.3 x 5(P). Physically it simulates the distribution of dopant phosphorous which has an equilibrium distribution coefficient of 0.35 in the melt near the melt-crystal interface. The crystal is being grown in a rate of 1mm/min and rotating at 4rpm. At the melt-crystal interface, the normalized concentration level is about 1.78. The specie distribution (in the axial direction) is identical to the result obtained from one dimensional calculations.

In the second case, we allow C_L at $\zeta' = aSc$ varies in the radial direction. The values of C_L at $\zeta' = aSc$ are obtained from the 'bulk' flow calculations equation (5). The radial and axial velocities of the melt are obtained from the solution of the reduced Navier-Stokes equations (29) through (32). The purpose of this calculation is to demonstrate the capability of the thin layer model in predicting the solute distribution (in both axial and radial directions) in the melt near the melt-crystal interface. Nondimensional parameters used are the same as in first case. The result is shown in Figure 4.4.7. It is found that the nonuniform species distribution caused by natural convection has an effect on the distribution of the species at the melt-crystal interface.

5. CALCULATIONS II

5-1. Group IV - Applications to Silicon Crystal Growth

In the previous section we verified the numerical procedures which have implemented in the existing computer code. The calculations were performed using nondimensional parameters not applicable to silicon crystal growth. These parameters were chosen to minimize the computation resources needed to verify the code. In this section, we summarize the numerical calculations performed with parameters relevant to Cz silicon growth under normal conditions. Since not all growth parameters are measurable, e.g. heat transfer coefficient at the free surface, etc., approximations were used for those parameters.

A total of six two dimensional (no θ dependence) calculations were performed for silicon CZ growth. The first four cases are simulations of silicon crystal growth with a crystal diameter of 8.8cm in a 13cm diameter crucible. The silicon is rotating at 1.32rpm, while the crucible is counter-rotating at 0.5rpm. The height of the grown crystal is taken as 5.1cm and the height of the melt (between the crystal interface and crucible bottom) is taken to be 3.8cm. The first two cases assumed the crucible has a uniform temperature of 1462 C, while the third and fourth cases assumed a crucible temperature of 1432 C. The fifth case shown is a simulation of silicon crystal growth in a 26.5cm diameter crucible. The crystal diameter is the same as in the previous cases, and the crucible is counter-rotating at a rate of 0.13rpm. This was chosen to give the same crucible Reynolds number as for the previous case. The height of the melt is taken to be 17.7cm in this case, and the crystal interface is assumed to be at the equilibrium Si melting temperature 1412 C. The heat radiation condition at both the melt-argon and crystal-argon interfaces is applied in all the cases. The sixth case simulated a growth of a large diameter crystal (28.58cm). In this case the Reynold's number is about 7 times larger than the other cases.

The purpose of Cases 1 and 2 is to compare the effects of the temperature variation along the melt-crystal interface with and without the assumption of a planar interface. Case 3 demonstrates that a near planar interface (or nearly uniform temperature variation along the interface) can be achieved by reducing the bouyancy effects, and proper adjustment of the heat radiation condition. Case 4 shows the capability to calculate a case with a meniscus. Further details of these calculations are presented below. Case 5 is to study the effects of large crucible, while Case 6 shows a growth of large diameter crystal.

In all the cases studied, a common flow pattern is observed: at least two vortexes exist in the melt. One vortex is found near the crystal. This vortex has a radially outward flow due to the rotation of the crystal. The radial velocity (near the crystal interface) increases as the radius of the crystal and reaches a maximum at about one crystal radius. It diminishes as it goes further outward. At some radial distance (usually greater than one crystal radius) the flow turns downward, reversed its direction and flow radial inward. This change of direction is caused by another vortex which is driven by the natural convection. The point where the first vortex turns direction depends on the relative strength of the forced convection (induced by the rotation of the crystal) and the natural convection (induced by the hot crucible walls). The strength of the forced convection depends on rotational rate and radius of the crystal. While, the strength of the natural convection depends on the magnitude of the Grashof number and Prandlt number. The Grashof number depends on the physical properties of the melt, temperature difference between the crucible wall and the melt temperature, and a characteristic length. The Prandlt number depends on the physical properties of the melt. For this reason, the flow pattern in a large crucible (Case 5) is much more complicated.

Details of each case study follows:

CASE 1

In this calculation, the melt-crystal interface is assumed planar, i.e., the shape of the melt-crystal interface is predetermined. The assumption is valid if the net heat flux along the interface is approximately constant. The average temperature of the argon gas (above the free surface) is assumed to be 1355 C. Emissivities for the crystal surface and free surface are taken to be 0.2 (a constant for simplicity). Figure 5.1.1 shows the grid used for the numerical simulations. Grid points are packed near the interface and crystal corner to obtain better resolution in those regions.

Since the melt-crystal interface is planar, the rotating crystal acts as a centrifugal disk pump which sucks up the melt and spins it out in the radial direction. As can be seen from Figure 5.1.2, an Ekman layer of thickness 0.11cm is formed under the planar interface. The theoretical value from a finite diameter rotating disk in a semi-infinite fluid without free convection is about 0.14cm. The radial outward flow, due to the rotating crystal, meets the radial inward flow, due to natural convection driven by the hot crucible wall, at a radial distance 1.2cm away from the crystal corner. Temperature contours for both phases are also shown in Figure 5.1.2. The zero heat flux condition has been used at the top of the crystal, hence a certain axial distance (in this case 5.1cm), the temperature within the crystal becomes uniform. The axial heat flux along the melt-crystal interface is nonuniform, which is a consequence of the neglect of the latent heat of crystallization at the interface.

Figure 5.1.3 shows the heat fluxes along the interface in the melt and crystal phases. The difference between the curves indicates the net heat flux removed from the heat gained due to latent heat of crystallization. Due to natural convection, the higher temperature melt is carried towards the interface for $r>0.3$. This motion of the melt produces nonuniform heat flux along the interface in the melt phase and, consequently, nonuniform solidification at the interface results. Physically, nonuniform solidification along the interface means a nonplanar interfacial shape. This example shows that if the assumption of a planar interface is used, uniformity of the net heat flux to the interface must be checked to verify the consistency of the assumption.

The concentration distribution of an arbitrary impurity is shown in Figure 5.1.4. The distribution is calculated by assuming no loss or creation of species at any surface. For convenience, the concentration level is normalized to a reference concentration. Since the species boundary layer thickness is about $Sc = 7.3$ times thinner than the momentum boundary layer thickness, numerical resolution of the concentration distribution will be inadequate near the interface. A zero condition is used at the interface for this reason, hence, in this 'bulk' flow calculation, species concentration levels near the interface are valid only outside the species boundary layer. A submodel (thin layer) was developed to resolve the species boundary layer near the melt-crystal interface as discussed in Section 4-4. Concentration levels at the interface from the 'bulk' flow calculation are used as boundary conditions in the submodel calculation. In the thin layer, natural convection effects are assumed to be small, and the fluid flow is solely due to the rotation of the crystal. In this case, the thickness of the thin region is taken to be $0.8\sqrt{(\nu/\omega)}$ (0.11cm). Phosphorus, which has a segregation coefficient, k_o, of 0.35, is chosen for the numerical calculations. Using the rotational rate of the crystal and a calculated pulling rate equation (14) of 0.2mm/min, the suction parameter 'a' is determined to be 0.0175.

Figure 5.1.5 shows the concentration distribution inside the thin layer. We note again that from a crystal grower's point of view, the species concentration distribution in the melt is of no interest; rather, the species concentration level in the crystal is of primary interest. The commonly used effective distribution coefficient k_{eff}, defined as $k_o * C_o / C_L$, is a measure of concentration level of a particular specie in the crystal. Here, k_o is the equilibrium distribution coefficient which is a ratio of specie concentration in the crystal at the interface to the concentration of specie in the melt at the interface, and k_o is usually taken from the phase diagram. For a particular specie, if the concentration of the specie in the melt near the interface is known, k_{eff} can be determined. From our numerical calculations, the k_{eff} (based on C_o and C_L) for phosphorus varies from 0.427 to 0.408, while a numerical correlation using one dimensional approximation by BPS [34] gave a value of 0.445. The one dimensional analysis [34] assumed a quadratic variations for the axial velocity and ignored the radial variation of the species concentrations.

CASE 2

The geometric configuration in this calculation is the same as in the first case, except that the shape of the interface is also determined as part of the solution from the heat flux condition at the melt-crystal interface. The crystal pulling velocity can be determined from the area average net heat transfer across the interface, since this is a necessary condition for a steady state solution to exist. In other words, for the physical parameters used, the crystal is growing at a constant diameter. The interfacial position is considered as steady state if the local pulling velocity along the interface is within 3% of the average pulling velocity obtained from average net heat available for solidification.

Figure 5.1.6 shows the coordinates at the end of the steady state calculation. The initial coordinate mesh is orthogonal, which is the same as that shown in Figure 5.1.1, but due to deformation of the interface the coordinates become nonorthogonal. Figure 5.1.7 shows the secondary flow and temperature contours where it is seen that the vortex structure and temperature distributions are similar to those for Case 1. The shape of the interface becomes convex for the parameters used, and the maximum int rface deformation is about 0.9cm. The pulling velocity obtained from the calculations is about 0.2mm/min. Local heat fluxes in the melt and crystal phases along the melt-crystal interface are plotted in Figure 5.1.8. The difference between the heat fluxes indicates the amount of heat gain from crystallization.

In this example, we have shown that nonuniform solidification at the interface leads to nonplanar interface and nonuniform temperature near the melt-crystal interface.

CASE 3

The purpose of this calculation is to show that a 'near' planar interface can be achieved by adjusting various parameters. In this particular calculation, the crucible temperature has been reduced such that the strength of natural convection is reduced to provide a more uniform temperature distribution near the melt-crystal interface. On the other hand, rotational rate of the crystal is increased to provide a stronger forced convection with a similar result.

In this calculation, the temperature of the crucible is assumed to be 1432 C. Emissivities for the free surface and crystal surface are taken to be 0.2 and 0.08, respectively. As seen from Figure 5.1.9, the influence of natural convection is substantially decreased. Temperature contours for both phases are also shown. The maximum deviation of interfacial height is less than 1.2%, while the maximum deviation of the free surface height (without considering surface tension) is less than 0.2%. Heat fluxes of both phases along the interface are shown in Figure 5.1.10, where again the difference between the two curves indicates the amount of heat gained from crystallization. Figure 5.1.11 shows the normalized net heat fluxes along the interface with and without the assumption of planar interface, where it is seen that the heat flux is much more uniform in the case with the calculated nonplanar interface.

The specie concentration distribution of an arbitrary impurity is shown in Figure 5.1.12. The boundary conditions used are the same as in Case 1. The more uniform distribution near the interface which is found in this case confirms that the effect of natural convection in transporting species from the melt toward the interface is reduced with the parameters chosen for this simulation.

Again, a thin layer submodel calculation near the melt-crystal interface is performed to resolve the species boundary layer (see Figure 5.1.13). Using the rotational rate of the crystal, and the calculated crystal pulling velocity (0.04mm/min), the suction parameter is determined to be 0.0035. From the present numerical calculations, the k_{eff} for phosphorous only varies from 0.369 to 0.368, due to the nearly uniform concentration distribution while the one dimensional approximation by BPS [34] is 0.368.

CASE 4

The purpose of this calculation is to demonstrate the numerical capability of the existing code to handle a case with a meniscus. In this calculation a Bond number of 58 and contact angle of 15 are used. The Bond number and the contact angle are determined from the physical properties of silicon. The free surface shape is determined by the surface tensional force and inertial force due to rotations. Other parameters are the same as in Case 3 except the following: the average temperature of the argon gas is assumed to be 1379 C.

Due to the sharp change in slope of the free surface near the crystal, a new method of constructing the grid is used, with the coordinates shown in figure 5.1.14. The boundary-fitted coordinates are generated using elliptic partial differential equations based on the work of Thompson, et al., [39,40]. The origins of the elliptic generation technique are based on an analogy between the requirements of two dimensional coordinate systems, and the properties of streamline and potential function distributions. This grid generation technique have been modified and applied successfully [43] in complicated geometries. The temperature contours of both phases and secondary flow are shown in Figure 5.1.15. The maximum deviation of the interfacial height, in this case is within 4% (i.e., $\sim$1mm) while the maximum deviation of the free surface is about 7mm. The calculated meniscus shape when the rotational effects are not considered have been compared with the analytical solution of Young-Laplace's equation [20]. The comparison is in good agreement. The flow pattern obtained in this case is quite similar from those in previous cases. The vortice which under the free surface in the previous case is now 'pushed' into the interior of the melt under the crystal by the meniscus.

The general flow pattern, however, does not change: an Ekman layer under the crystal; radially outward flow caused by the rotating crystal is forced to turn-around by the radially inward flow caused by natural convection; axial flow beneath the crystal center is upward or downward depends on whether it is above or below the Ekman layer.

CASE 5

The calculation shown in (Cases 1 through 4) are done in a crucible of relatively small diameter. Note that the short height of the crucible means that the simulations are done for the near-end stage of a nonreplenishable process. In this case, a larger size crucible is used. The diameter of the crucible is 26.5cm with a melt height of 17.7cm and the length of the crystal is assumed to be 13.3cm. The rotational rate of the crystal is the same as before, but the rotational rate of the crucible is reduced so that the crucible Reynold's number is the same as for the previous cases. In physical terms, the crucible is rotating at 0.13rpm, and the temperature of the crucible is assumed to be 1432 C.

Figure 5.1.16 shows the coordinates for this calculation where there are 66 radial and 60 axial mesh points in the melt phase, and 42 radial and 22 axial points in the crystal phase. Figure 5.1.17 shows the secondary flow and temperature distributions, while a detailed velocity vector plot near the melt-crystal interface is shown in Figure 5.1.18. In this calculation, several more vortexes are found in the melt fluid. The most distinguished one is the one centered at 6.8cm from the crucible bottom. It carries the hot-melt fluid to a region near the crystal interface. Several recirculating vortexes are also observed. As shown in Figure 5.1.18, an Ekman layer of approximately 0.11cm is also found. We observed the similar results as in the previous cases since the nondimensional number in the governing equations are the same. However, there is no geometric similarities with the last cases (e.g., aspect ratio of the crucible are not the same as before). In this calculation, the ambient temperature of the argon gas is adjusted so that a melt-crystal interface of a maximum derivation of about 1% is obtained.

CASE 6

The calculation shown in this case is to simulate the crystal growth process to yield a large diameter crystal. A crystal of diameter 19.05cm is grown crucible of diameter 28.58cm. The height of the melt is 9.53cm. The crystal is rotating at 2rpm while the crucible is counter-rotating at 0.5rpm. In nondimensional terms, the Reynolds number, Re_s, based on the crystal radius and rotation is 7000 and the Reynold's number Re_c, based on the crucible radius and rotation is 4000.

Figure 5.1.19 shows the coordinates for this calculation where there are 68 radial and 48 axial mesh points in the melt phase, and 35 radial and 25 axial points in the crystal phase. Figure 5.1.20 shows the secondary flow and temperature contours of the melt and crystal phases. In this calculation, the forced convection induced by both the crystal and crucible rotations is larger than the previous cases and this results in a much more complicated flow pattern and temperature distribution in the melt. The radial velocities near the crucible are much larger than in the previous cases. These large radial velocities push the counter-rotating vortex upward and closer to the crucible side wall. The center of the vortex is at about one crystal radius in contrast to about 0.9 radius in previous cases. The strong radial flow makes a strong return flow at the free surface near the crucible side wall. This strong return flow brings the hot melt from the bottom and side crucible wall to the free surface.

6. THREE DIMENSIONAL CALCULATIONS

6-1. Group V - Applications to Continuous Feed Silicon Growth

A simulation of Czochralski silicon growth with a Continuous Liquid Feed (CLF) option has used to demonstrate the three dimensional capability of the computer code developed. A continuous CLF crystal growth was designed to permit crystal growth from a small melt volume. It has been reported that large melt volume changes during growth of the crystal was a strong influence to the crystal quality. The advantage of small melt volume used in CLF is then obvious. Another advantage of the CLF method is the high crystal yield per crucible i.e., longer crystal can be grown from each crucible.

A description of the set-up of the CLF is following. Two identical Czochralski crystal growth chamber are used. One crucible (the melter) serves as a supplier of melt fluid to the other (the grower). These two chambers are isolated from each other to eliminate problems associated with SiO build-up in the growth chamber. All growth conditions in these two chambers are identical except that the vertical motion of the two solid rods are in opposite directions. The melt fluid in the two crucibles is connected by an inverted U-tube at the free surface and melt fluid is transferred from the melter to the grower by hydrostatic pressure differentials through the inverted U-tube.

Since we are interested in the physics inside the grower chamber, numerical calculations are done for the growth chamber only and the three dimensional aspect of the problem is obtained by assuming a specific temperature distributions within a small region. The justification for this temperature assumption is as follows. The contact surface between the connecting tube and free surface is modeled as an area with a temperature different from that of the free surface. The flow rate in the inverted U-tube is assumed to be small compared to the melt-fluid velocity (secondary velocity) near the free surface. The temperature of the contact surface is specified as following. In CLF growth, the environment in the grower chamber is the same as the environment in the melter chamber, except that the directions of the growth are reversed in the two chambers. The temperature profile at the inlet of the inverted U-tube (in the melter side) should approximately be equal to the temperature profile at an area on the free surface of a grower crucible. Due to the passing of melt the fluid inside the tube, the outlet temperature of the tube can approximate as the average of the inlet temperature profile.

In our numerical simulation, an rectangular area of 0.87 x 0.84cm^2 is assumed to be the contact surface of the connecting tube. This contact surface is located about 1cm from the crucible wall at the free surface. The initial conditions correspondence to a two dimensional Czochralski growth with boundary conditions as stated in Case 3, Section 4.5. Once the three dimensional steady state solution is obtained, we change the temperature of the contact area to the average of the temperature in the area. Calculations with a rectangular spot of constant temperature at the free surface is then performed. Figure 6.1.1 shows the coordinates in the r-θ plane for the melt and solid phases. Notice that the grids are packed where the connecting tube is in contact with the melt phase at the free surface. Coordinates in the r-z plane are the same as in the two dimensional cases. Figure 6.1.2 shows the velocity plots in the r-θ planes at various heights. The free surface is located at about $\zeta = 0.84$. The small temperature perturbation due to the connecting tube does not seem to have a large effect on the azimuthal velocities. Figures 6.1.3 and 6.1.4 shows the temperature contours of the melt and crystal phases respectively. The cooler temperature melt is well mixed at 0.6cm below the free surface. Further, the small temperature disturbance does not have influence as the temperature contours of the crystal Figure 6.1.5 and 6.1.6 show the secondary flow and temperature contours of the melt phase under the contacting area. In order to look at how the temperature disturbance distribute in space, we plot the non-dimensional temperature difference in the radial direction for various height. The plot is shown in figure 6.1.7. As shown in Figure 6.1.8, the temperature disturbance behaves like an exponential decay function in height.

7. CONCLUSIONS AND RECOMMENDATIONS

A numerical algorithm to follow free and melt-crystal interfaces in conjunction with the LBI scheme has been developed and tested for Czochralski crystal growth problems. The physical domain is transformed using a time dependent boundary fitted coordinate system and the nonlinear interfacial boundary conditions are applied along these boundaries which can be evolving in time. The solid and liquid phases are coupled through the heat flux conditions along the melt-solid interface. The velocity, temperature, and species distribution of the melt phase, temperature distribution of the crystal phase, along with the positions of the melt-crystal interface and free surface, are obtained by the consistency split LBI scheme. The crystal pulling velocity is also determined from the necessary condition of the interface tracking algorithm. A thin layer submodel which can provide species concentration levels near the melt-crystal interface is also included. The procedure has been utilized for sample calculations which demonstrate the feasibility of the approach and its potential value for assessing the Czochralski crystal growth process.

With the numerical capability developed in the present work, the thermal variation and dopant concentration homogeneity along the melt-crystal interface can be predicted based on the external growth parameters. Moreover,a crystal pulling velocity can be provided for uniform growth.

Since our numerical scheme is written in primitive variable forms, extension to study three dimensional effects is not limited and was demonstrated in a simulation of Continuous Liquid Feed (CLF) Czochralski silicon growth.

In the present studies, we found that with the physical properties of the molten silicon and crucible sizes used in the industry, the shape of the free surface caused by rotation of the crucible and crystal cannot be approximated as planar. Surface tensional force at the melt-crystal-gas junction and near the free surface is important. The former causes the existence of a mensicus and latter causes Marangoni flow. The shape of the melt-crystal interface is important to know because it indicates the uniformity of the heat flux (directly the uniformity of the thermal stress) in the grown crystal. To achieve a near planar melt-crystal interface, the rotational rate of the crystal and/or the heat transfer conditions of the argon gas need to be determined.

8. REFERENCES

1. J. Czochralski, Z. Physik. Chemie 92 (1917) 219.

2. J.R. Carruthers and K. Nassau, J. Appl. Phys. 39 (1968) 5205.

3. D.S. Robertson, Brit. J. Appl. Phys. 17 (1966) 1047.

4. S.M. Pimputkar and S. Ostrach, J. Crystal Growth 55 (1981) 614.

5. S. Ostrach, J. Fluids Eng. 105 (1983) 5.

6. D.T.J. Hurle, J. Crystal Growth 65 (1983) 124.

7. W. Zulehner, J. Crystal Growth 65 (1983) 189.

8. W.E. Langlois, Ann. Rev. Fluid Mech. 17 (1985) 191.

9. N. Kobayashi and T. Arizumi, J. Crystal Growth 30 (1975) 177.

10. W.E. Langlois and C.C. Shir, Comput. Methods Appl. Mech. Eng. 12 (1977) 145.

11. N. Kobayashi, Comput. Methods Appl. Mech. Eng. 23 (1980) 24.

12. N. Kobayashi and R. Wilcox, J. Crystal Growth 59 (1982) 616.

13. W. Langlois, J. Crystal Growth 42 (1977) 386.

14. N. Kobayashi, J. Crystal Growth 52 (1978) 425.

15. W. Langlois, J. Crystal Growth, 46 (1979) 743.

16. N. Kobayashi, J. Crystal Growth 52 (1981) 425.

17. M.J. Crochet and P.J Wouters, J. Crystal Growth 65 (1983) 153.

18. G. Williams and R.E. Reusser, J. Crystal Growth, 64 (1983) 448.

19. J.J. Derby, et al, J. Electrochem, Soc. 132 (1985) 470.

20. D.T.J. Hurle, J. Crystal Growth 63 (1983) 13.

21. P.A. Ramachandran, M.P. Dudukovic, J. Cryst. Growth, 71 (1985) 399.

22. C.J. Chang and R.A. Brown, J. Comp. Phys. 53 (1984) 1.

23. K. Shiroki, J. Crystal Growth 40 (1977) 129.

24. C.D. Brandle, J. Crystal Growth 42 (1977) 400.

25. D.C. Miller and T.L. Pernell, J. Crystal Growth 57 (1982) 253.

26. R. Lamprecht et al, J. Crystal Growth 65 (1983) 143.

27. A.D.W. Jones, J. Crystal Growth 69 (1984) 165.

28. L.O. Wilson, J. Crystal Growth 44 (1978) 371,

29. A.M.J.G. Van Run, J. Crystal Growth 47 (1979) 680.

30. L.O. Wilson, J. Crystal Growth 48 (1980) 435.

31. L.O. Wilson, J. Crystal Growth 48 (1980) 451.

32. D. Camel & J.J. Favier, J. Crystal Growth 61 (1983) 125.

33. H. Schlichting, Boundary Layer Theory, McGraw Hill.

34. J.J. Favier and L.O. Wilson, J. Crystal Growth 58 (1982) 103.

35. W.R. Briley and H. McDonald, J. Comp. Phys. 34 (1980) 54.

36. W.R. Briley, H. McDonald, S. Shamroth, AIAA Journal 21 (1983) 1467.

37. N.S. Liu, S. Shamroth, H.L. Grubin, SRA Report R82-920013-4 (1982).

38. Y.T. Chan, N.S. Liu, H.J. Gibeling, H.L. Grubin, 23rd National Heat Transfer Conf., Denver, CO (1985).

39. J.F. Thompson, F.C. Thames, C.W. Mastin, J.Comp.Phys. 15, (1974).

40. J.F. Thompson; Ed, 'Numerical Grid Generation' North Holland 1982.

41. R. Levy and H.J. Gibeling. SRA Report R80-2, 1980.

42. Y.H. Oh, NASA-Langley Research Final Report NSG 1087, 1978.

43. R.C. Buggeln, D.V. Roscoe, Y.N. Kim, H. McDonald, AFWAL-TR-85-2038, 1985.

44. R.B. Bird, et al., Transport Phenomena, John Wiley & Sons, 1960.

45. Carslaw and Jaegar, Conduction of Heat in Solids, Oxford, 1959.

46. J.A. Burton, R.C. Prim and W.P. Slichter, J. Chem. Phys. 21 (1953) 1987.

9. ACKNOWLEDGEMENTS

This work is supported by ONR under Contract N00014-83-C-0510.

APPENDIX A

Split LBI Algorithm

Linearization and Time Differencing

The system of governing equations can be written as a single grid point in the following form:

$$\partial\, H(\phi)/\partial t = D(\phi) + S(\phi) \qquad \text{(A-1)}$$

where ϕ is the column-vector of dependent variables, H and S are column-vector algebraic functions of ϕ, and D is a column vector whose elements are the spatial differential operators which generate all spatial derivatives appearing in the governing equation associated with that element.

The solution procedure is based on the following two-level implicit time-difference approximations of (A-1):

$$\left(H^{n+1} - H^{n}\right)/\Delta t = \beta\left(D^{n+1} + S^{n+1}\right) + (1-\beta)\,\left(D^{n} + S^{n}\right) \qquad \text{(A-2)}$$

where, for example, H^{n+1} denotes $H(\phi^{n+1})$ and $\Delta t = t^{n+1} - t^{n}$. The parameter β $(0.5 \leq \beta \leq 1)$ permits a variable time-centering of the scheme, with a truncation error of order $[\Delta t^2, (\beta - 1/2)\,\Delta t]$.

A local time linearization (Taylor expansion about ϕ^n) of requisite formal accuracy is introduced, and this serves to define a <u>linear</u> differential operator L such that

$$D^{n+1} = D^{n} + L^{n}\,\left(\phi^{n+1} - \phi^{n}\right) + 0\,\left(\Delta t^{2}\right) \qquad \text{(A-3)}$$

Similarly,

$$H^{n+1} = H^{n} + \left(\partial H/\partial\phi\right)^{n}\,\left(\phi^{n+1} - \phi^{n}\right) + 0\,\left(\Delta t^{2}\right) \qquad \text{(A-4)}$$

$$S^{n+1} = S^{n} + \left(\partial S/\partial\phi\right)^{n}\,\left(\phi^{n+1} - \phi^{n}\right) + 0\,\left(\Delta t^{2}\right) \qquad \text{(A-5)}$$

Equations (A-3, 4,5) are inserted into Eq. (A-2) to obtain the following system which is linear in ϕ^{n+1}

$$\left(A - \beta\Delta t\ L^n\right)\left(\phi^{n+1} - \phi^n\right) = \Delta t\left(D^n + S^n\right) \qquad \text{(A-6)}$$

and which is termed a linearized block implicit (LBI) scheme. Here, A denotes a square matrix defined by

$$A \equiv \left(\partial H/\partial\phi\right)^n - \beta\Delta t\left(\partial S/\partial\phi\right)^n \qquad \text{(A-7)}$$

Consistent Splitting of the LBI Scheme

To obtain an efficient algorithm, the linearized system (A-6) is split using ADI techniques. To obtain the split scheme, the multidimensional operator L is rewritten as the sum of three "one-dimensional" sub-operators L_i (i = 1, 2, 3) each of which contains all terms having derivatives with respect to the i-th spatial coordinate. The split form of Eq. (A-6) can be derived either by following the procedure described by Douglas and Gunn in their generalization and unification of scalar ADI schemes, or using approximate factorization. In either case, for the present system of equations the split algorithm is given by

$$\left(A - \beta\Delta t L_1^n\right)\left(\phi^* - \phi^n\right) = \Delta t\ D^n + S^n) \qquad \text{(A-8a)}$$

$$\left(A - \beta\Delta t L_1^n\right)\left(\phi^{**} - \phi^n\right) = A\left(\phi^* - \phi^n\right) \qquad \text{(A-8b)}$$

$$\left(A - \beta\Delta t L_l^n\right)\left(\phi^{n+1} - \phi^n\right) = A\left(\phi^{**} - \phi^n\right) \qquad \text{(A-8c)}$$

where ϕ^* and ϕ^{**} are consistent intermediate solutions[12]. If spatial derivatives appearing in L_i and D are replaced by three-point difference formulas, then each step in Eqs. (A=8a), b, c) can be solved by a block-tridiagonal elimination.

APPENDIX B

Heat transfer model at crystal surface

If the heat convection boundary, as outlined in section 2-6, is used, the Nusselt number must be known. The boundary condition is applied along the exposed crystal surface. The most suitable heat transfer model can be found in Bird [44] - Heat transfer coefficients for forced convection around submerged objects. A correlation is available under the following assumptions.

a) uniform surface temperature
b) gas properties are evaluated at film temperature
c) gas approaching velocity is constant
d) gas flow is cross stream

$$\log (Nu\, Re^{-1}\, Pr^{-1/3}) = m \log Re + b$$

where $m = -0.4725$
$b = -0.3147$

and the Nusselt and Reynolds numbers are nondimensionalized by the diameter of the cylinder.

Group	Description
A	Studies on hydrodynamics of the melt phase with planar melt-crystal interface and free surface
B	Studies on temperature distribution of the melt and/or crystal phase
C	Combined problem of melt and crystal phase

TABLE 1.1.1 - Groups of Numerical Modeling in Czochralski Growth

	Melt Phase						Crystal Phase	
Authors	Method	Convection: Forced	Convection: Free	Heat Radiation	Free Surface	Melt Interface	Method	Heat Radiation
Kobayashi and Arizumi 1970	FDM 2-D	$Re<500$; $Pr=0.3$ Rotating Crystal	$Gr=60$	$\varepsilon=0.2$	Planar	N/A	N/A	N/A
Langlois and Shir 1977	FDM 2-D	$Re=2$; $Pr=2$ Counter Rotation	$Gr=<3$	N/A	Planar	N/A	N/A	N/A
Langlois 1977	FDM 2-D	$Re=40$; $Pr=0.08$ Counter Rotation	$Gr=9\times10^5$	N/A	Planar	N/A	N/A	N/A
Kobayashi 1978	FDM 2-D	$Re=40$; $Pr=0.01, 0.1$ Rotating Crystal	$10^3<Gr<10^5$	Insulated	Planar	N/A	N/A	N/A
Langlois 1979	FDM 2-D	$Re=1700$; $Pr=0.03$ Rotating Crystal	$Gr<4.7\times10^7$	$\varepsilon=0.33$	Planar	N/A	N/A	N/A
Kobayashi 1980	FDM 2-D	$Re=40$; $Pr=1$ Counter Rotation	$Gr=500$	Insulated	Planar	N/A	N/A	N/A
Kobayashi 1981	FDM 2-D	$40<Re<200$; $Pr=1$ Counter Rotation	$Gr<10^5$	Insulated	Planar	N/A	N/A	N/A
Crochet, et al. 1983	FEM 2-D	$Re<1000$; $Pr=0.01$ Counter Rotation	$Gr<10^6$	Insulated	Planar	N/A	N/A	N/A
Arizumi and Kobayashi 1972	FDM 2-D	N/A	N/A	$\varepsilon=0.2$	Planar	Included	FDM	$\varepsilon=0.2$
Williams and Reusser 1983	N/A	N/A	N/A	N/A	N/A	Planar	FEM	Specified Temperature
Derby and Brown 1985	FEM for LEC 2-D	N/A	N/A	$\varepsilon=0.8^*$ $\gamma=0.05$	Meniscus	Included	FEM	$\varepsilon=0.8^*$ $\gamma=0.05$
Ramachandran 1985	N/A	N/A	N/A	N/A	N/A	Included	FEM	$\varepsilon=0.64$
Chang and Brown 1984	FEM for Bridgeman 2-D	$Pr=1$ No Rotation	$2\times10^5<Gr<10^6$	N/A	N/A	Included	FEM	N/A
Liu, et al. 1982	FDM 2-D	$Re=4000$; $Pr=0.08$ Counter Rotation	$Gr=0, 2\times10^2$	N/A	Planar	N/A	N/A	N/A
Present Work	FDM 2-D & 3-D	$100<Re<4000$ $Pr=1, 0.054$ Counter Rotation	$0<Gr<6\times10^6$	$\varepsilon=0.2$	Included & Meniscus	Included	FDM	$\varepsilon=0.2$

* $q=\varepsilon(\theta^4-\theta_a^4)+\gamma(\theta-\theta_a)$

TABLE 1.1.2 - Numerical Studies of Cz Crystal Growth by Various Authors

RUN # / PARAMETERS	TI-1	TI-2	TI-3
ω	0	-0.68	-0.68
δ_o	0.75	0.75	0.25

TABLE 4.2.1 - Parameters Used in Group I Studies

RUN # / PARAMETER	T2-1	T2-2	T2-3	T2-4	T2-5	T2-6	T2-7	T2-8
β	0	10	25	10	10	10	10	10
H	0	0	0	0	10	10	10	10
Pr	0.054	0.054	0.054	1.0	1.0	1.0	1.0	1.0
FREE SURFACE	NO	NO	NO	NO	NO	YES	YES	YES
INTERFACE	NO	NO	NO	NO	NO	NO	YES CONST. θ_S	YES*

TABLE 4.3.1 - Parameters Used in Group II Studies

RUN # / EFFECTS OF	T1-1	T1-2	T1-3	T2-1	T2-2	T2-3	T2-4	T2-5	T2-6	T2-7	T2-8
ROTATIONS	√	√									
CRYSTAL IMMERSION		√	√								
BUOYANCE				√	√	√					
PRANDLT NUMBER					√		√				
HEAT RADIATION AT FREE SURFACE							√	√			
MELT-SOLID INTERFACE									√	√	
SOLID-PHASE HEAT FLUX										√	√

TABLE 4.3.2 - Features Studied in Groups I and II

B.P.S. [46]	WILSON [28]	CAMEL et al. [32]
$\Delta \cong 1.6\ aSc^{2/3}$ for $aSc^{2/3} < 0.56$	$\Delta = \dfrac{1.8\ aSc^{2/3}}{1 + 0.13\ aSc^{2/3}}$ for $aSc^{2/3} < 1$	$\Delta \cong 2\ aSc^{1/2}$ for $aSc^{1/2} < 0.4$

TABLE 4.4.1 - Numerical Correlations for Δ

CASES 1 through 5

$Re_s = 1000.$

$Re_c = 850.$

$Pr = 0.054$

$Fr = 0.001$

$$\frac{Gr\ Tm}{Re^2 \Delta T} = 5.0$$

$Pe = 27.$

TABLE 5.1.1. Nondimensional Parameters Used in Group IV studies

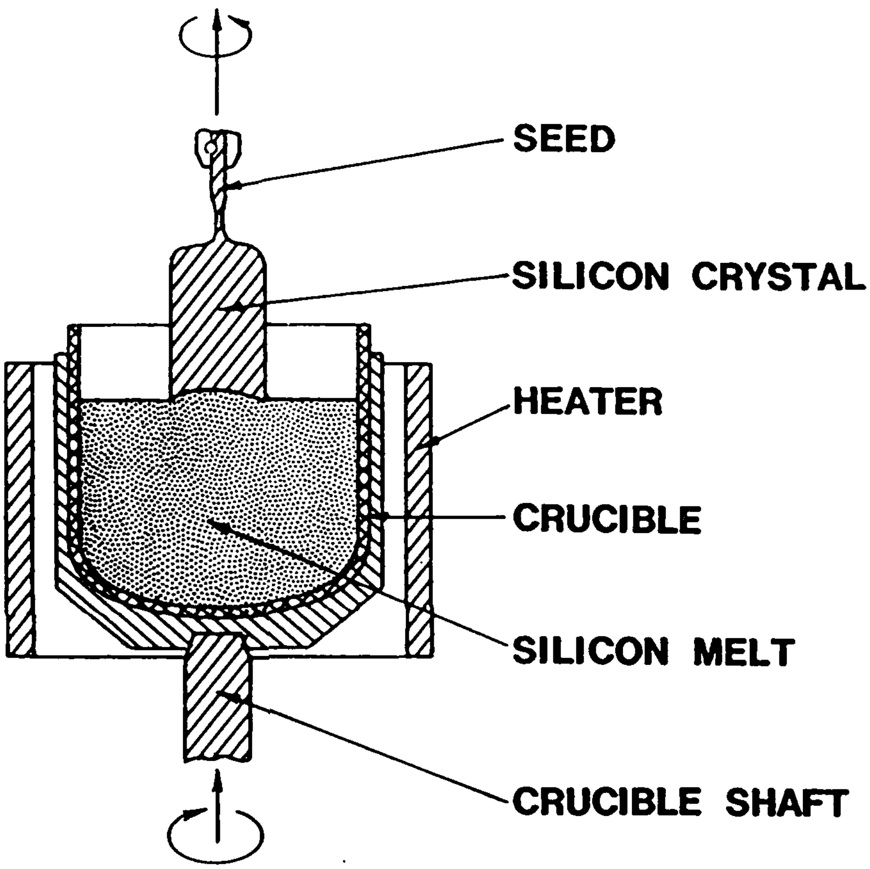

FIG. 1.1.1 - Basic Principle of Czochralski Crystal Growth Method

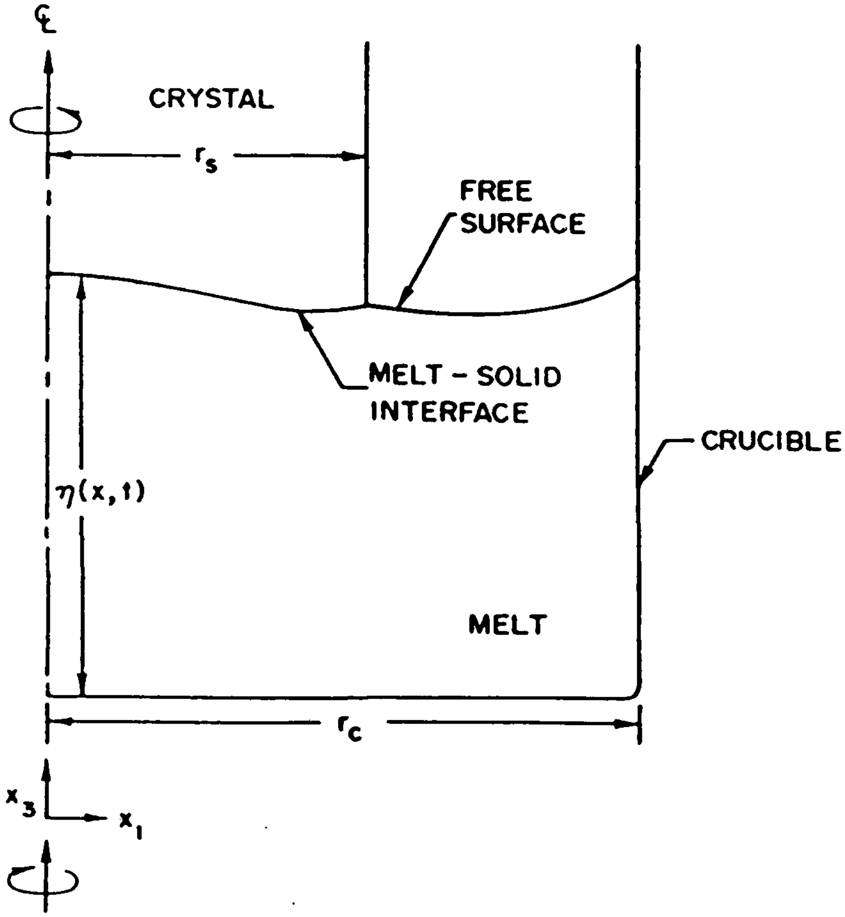

FIG. 3.1.1 - Computational Domain of a CZ Growth

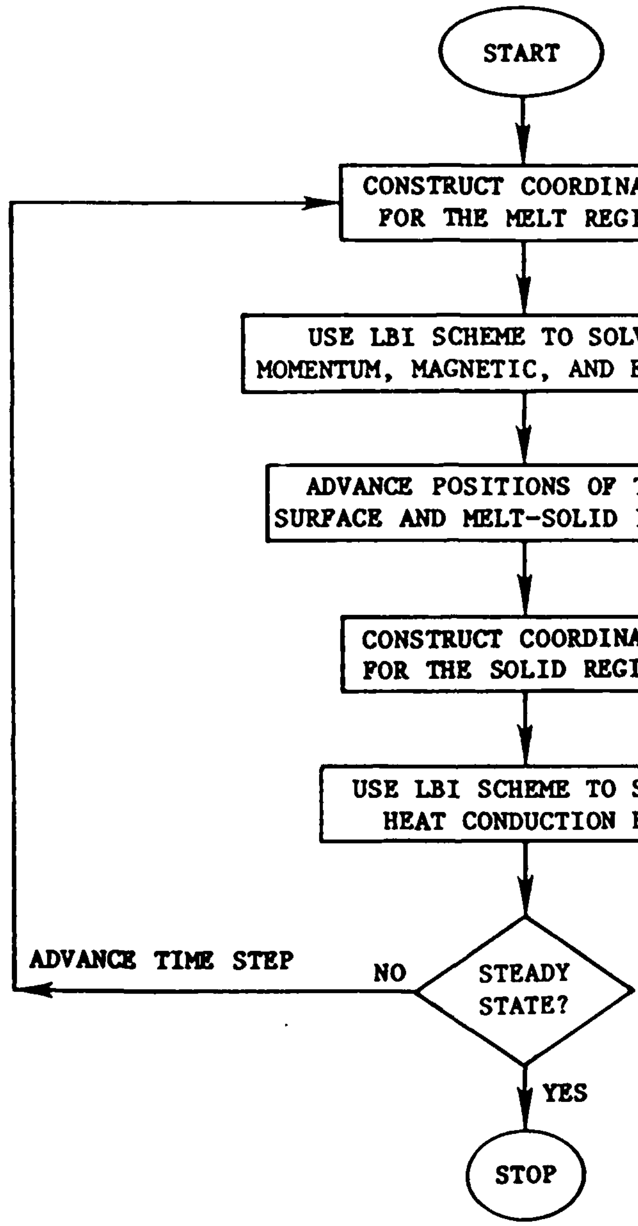

FIG. 3.1.2 - Flow Chart of the Numerical Method

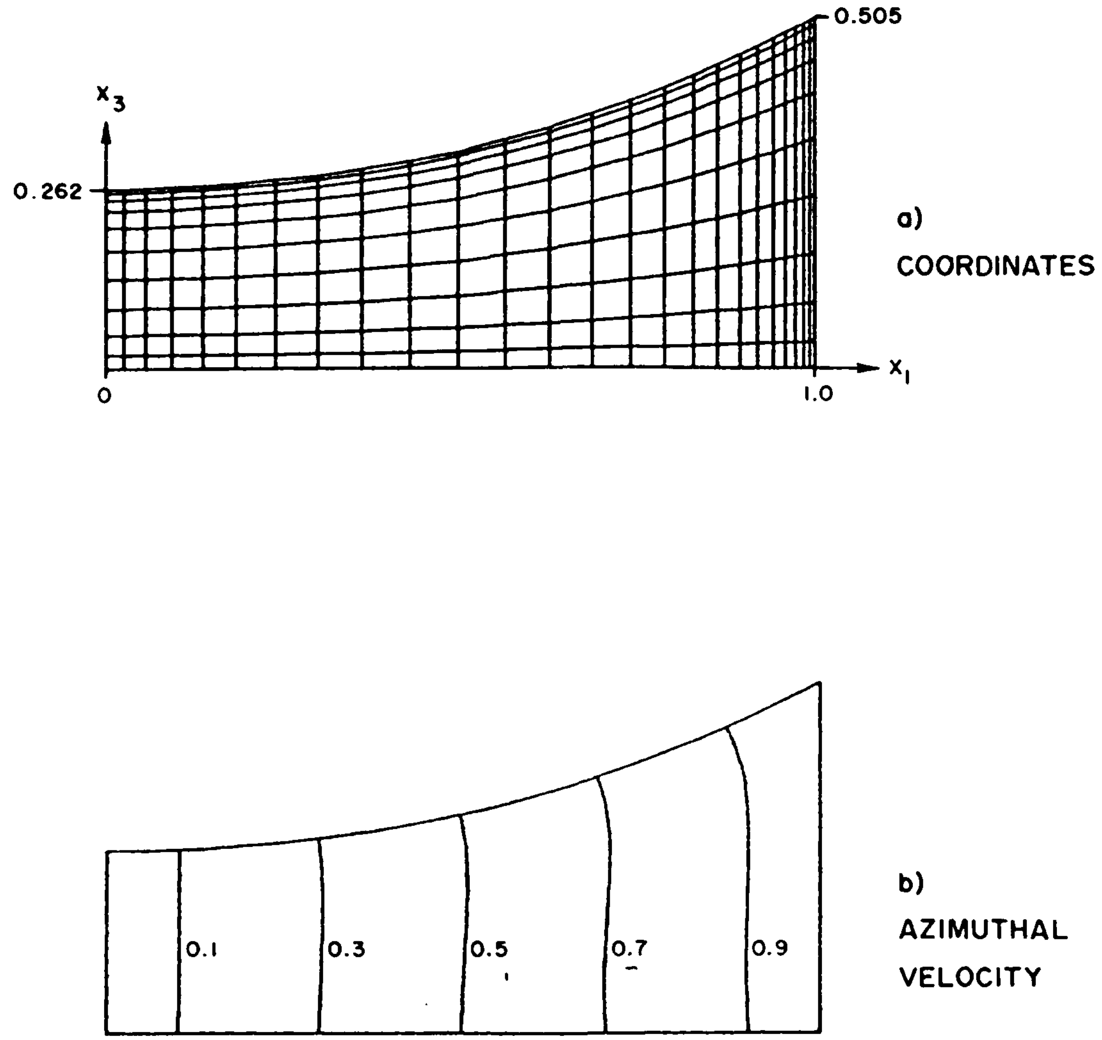

FIG. 4.1.1 - Free Surface Calculations in a Rotating Fluid

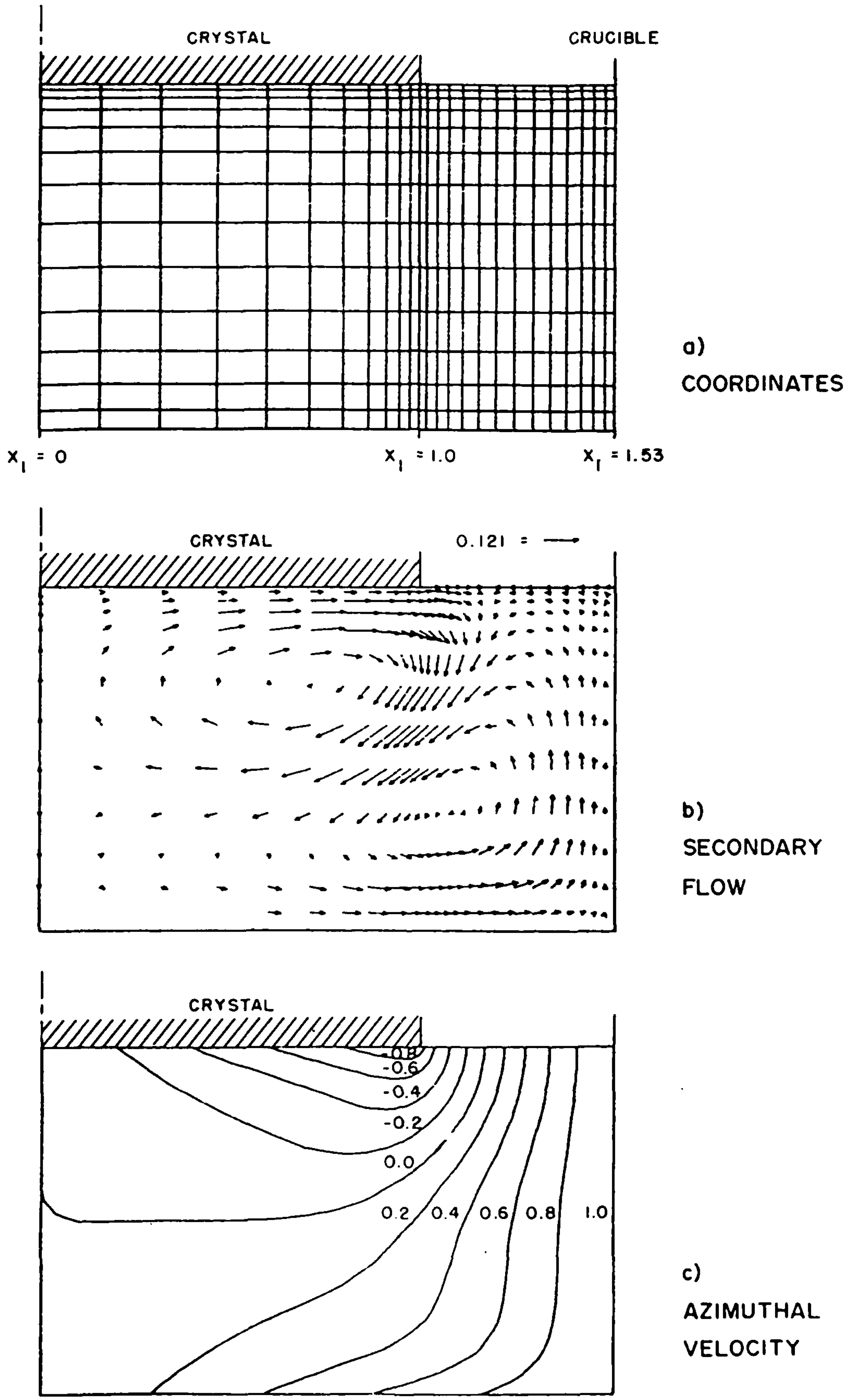

FIG. 4.1.2 - Preliminary Calculations on an Axisymmetric Flow in a Rotating Crucible with Counter-Rotating Crystal

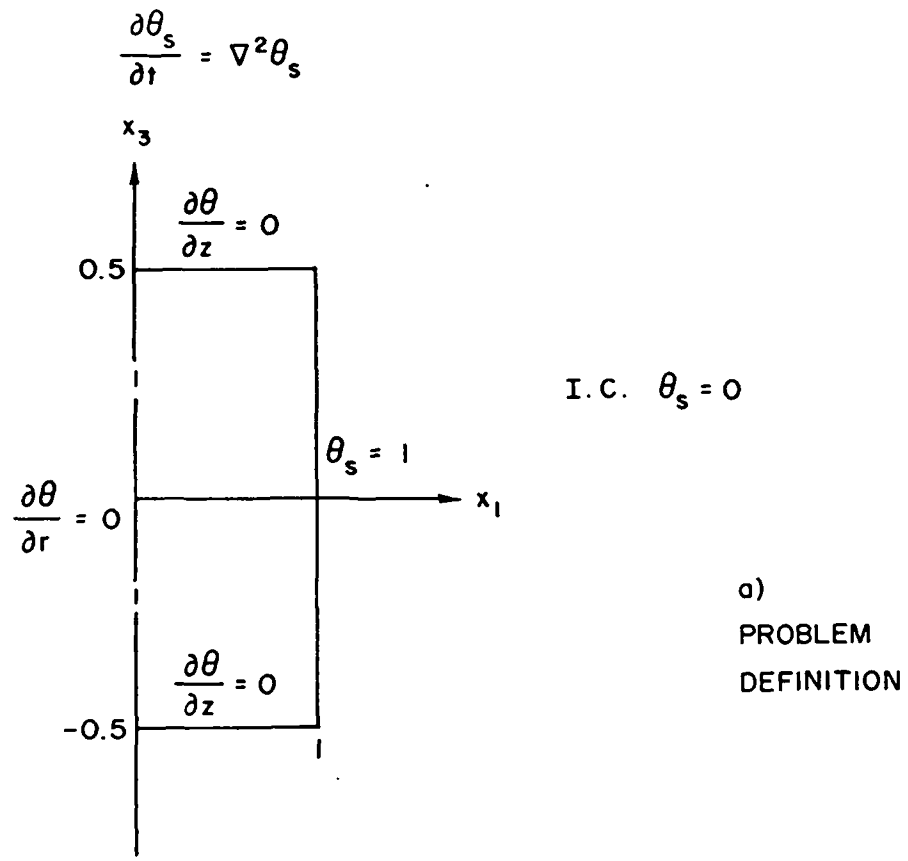

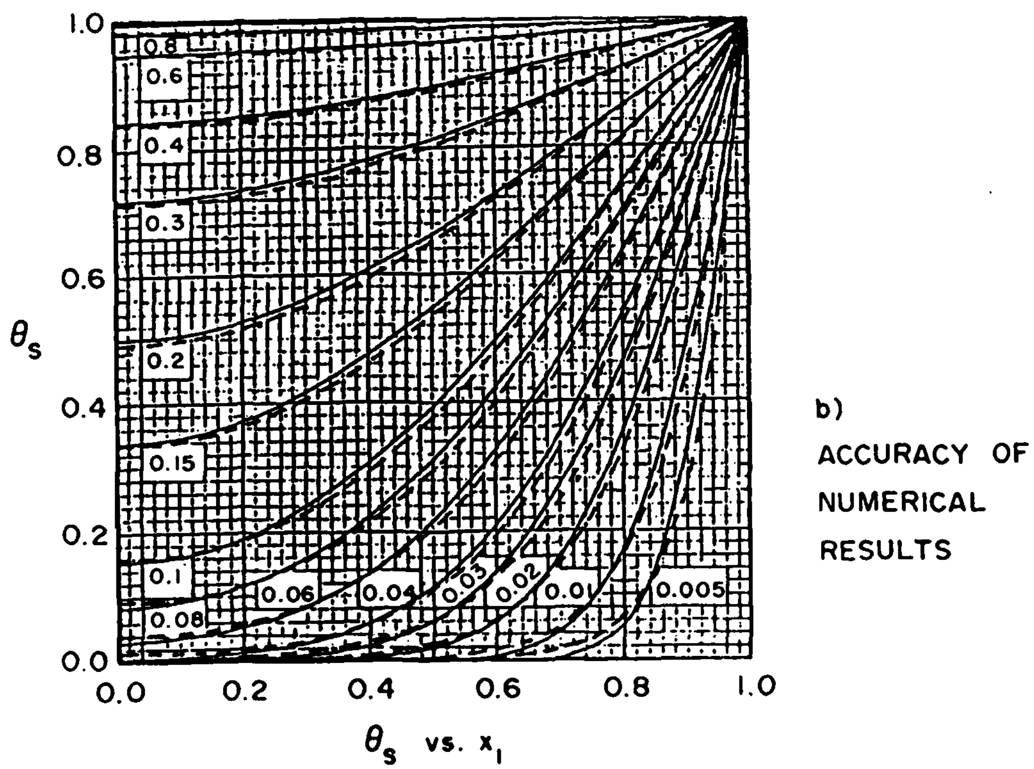

FIG. 4.1.3 - Comparison Between the Numerical and Analytical Results of a Semi-Infinite Cylinder Immersed in a Hot Bath

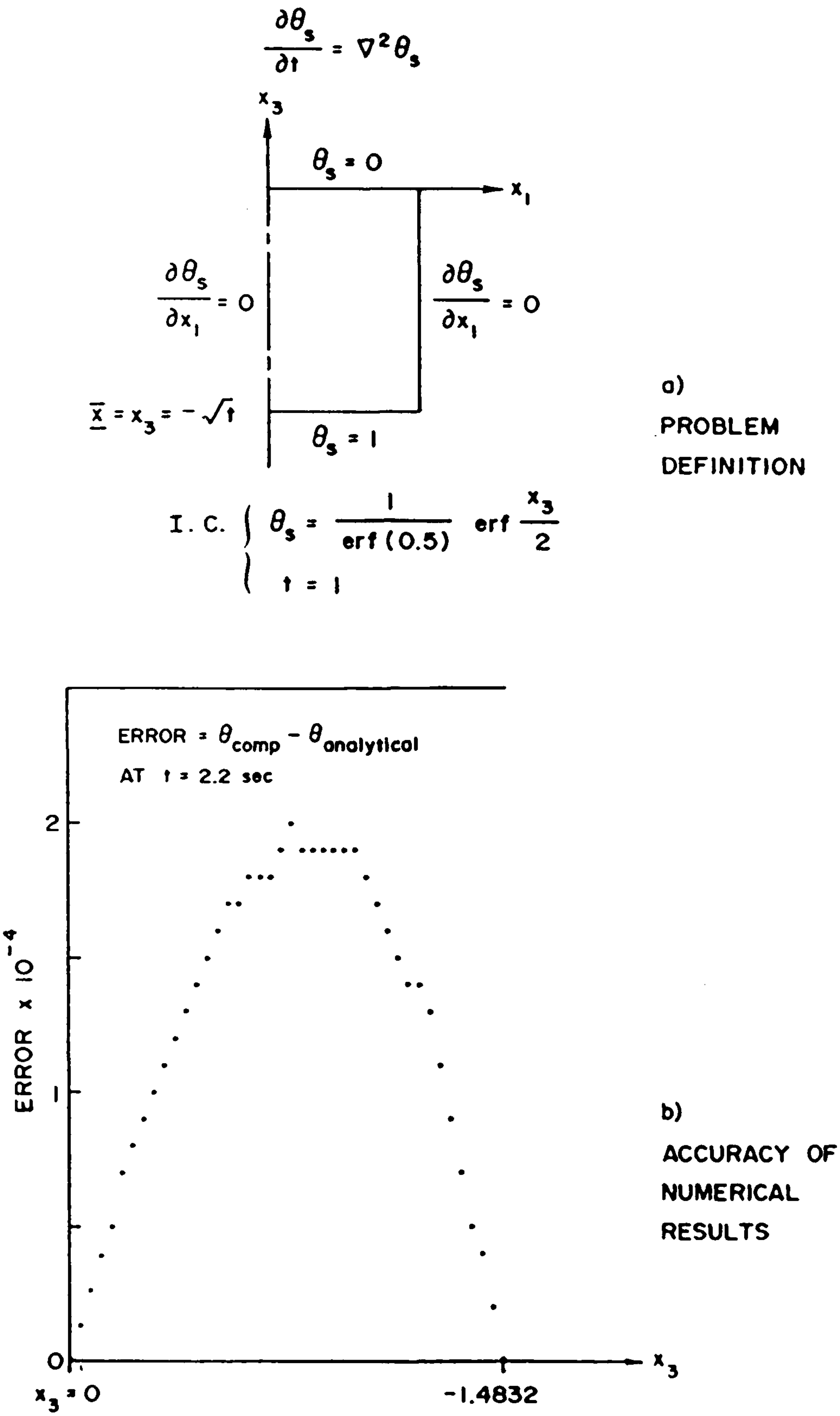

FIG. 4.1.4 - Comparison Between the Numerical and Analytical Results of the One-Dimensional Transient Heat Conduction with a Solidification Line

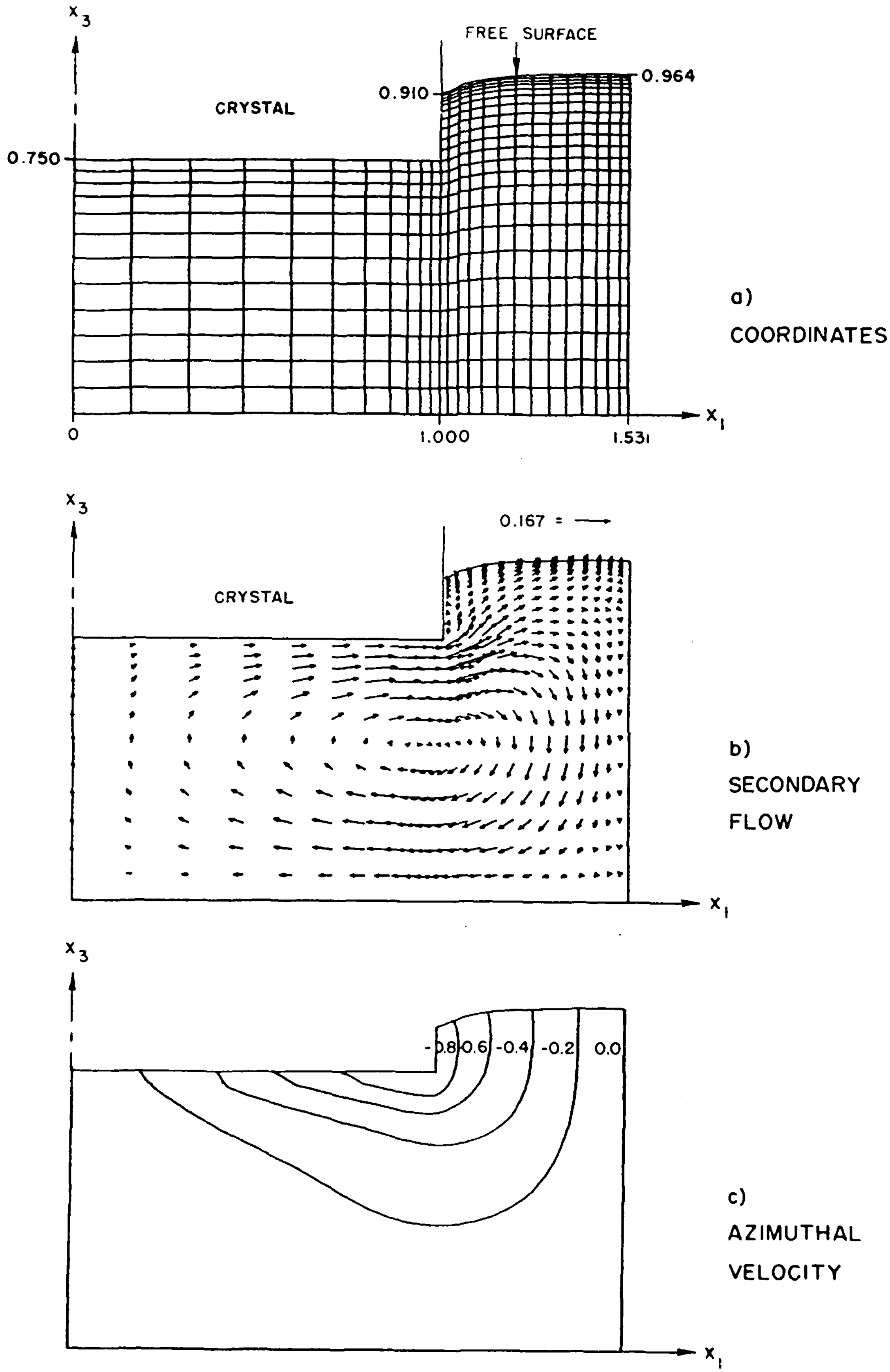

FIG. 4.2.1 - Run T1-1: $\omega = 0$, $\delta_o = 0.75$

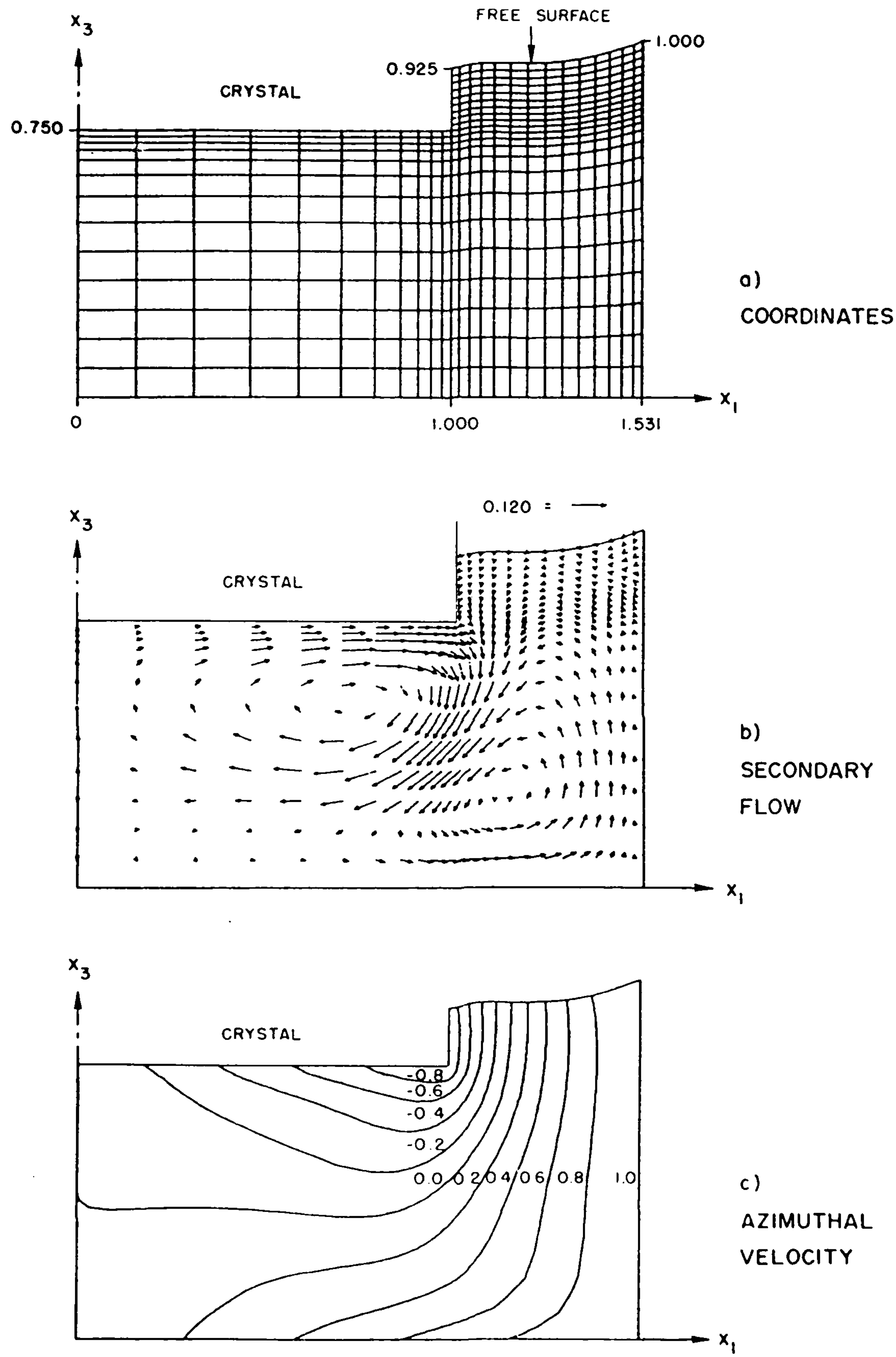

FIG. 4.2.2 - Run T1-2: $\omega = -0.68$, $\delta_o = 0.75$

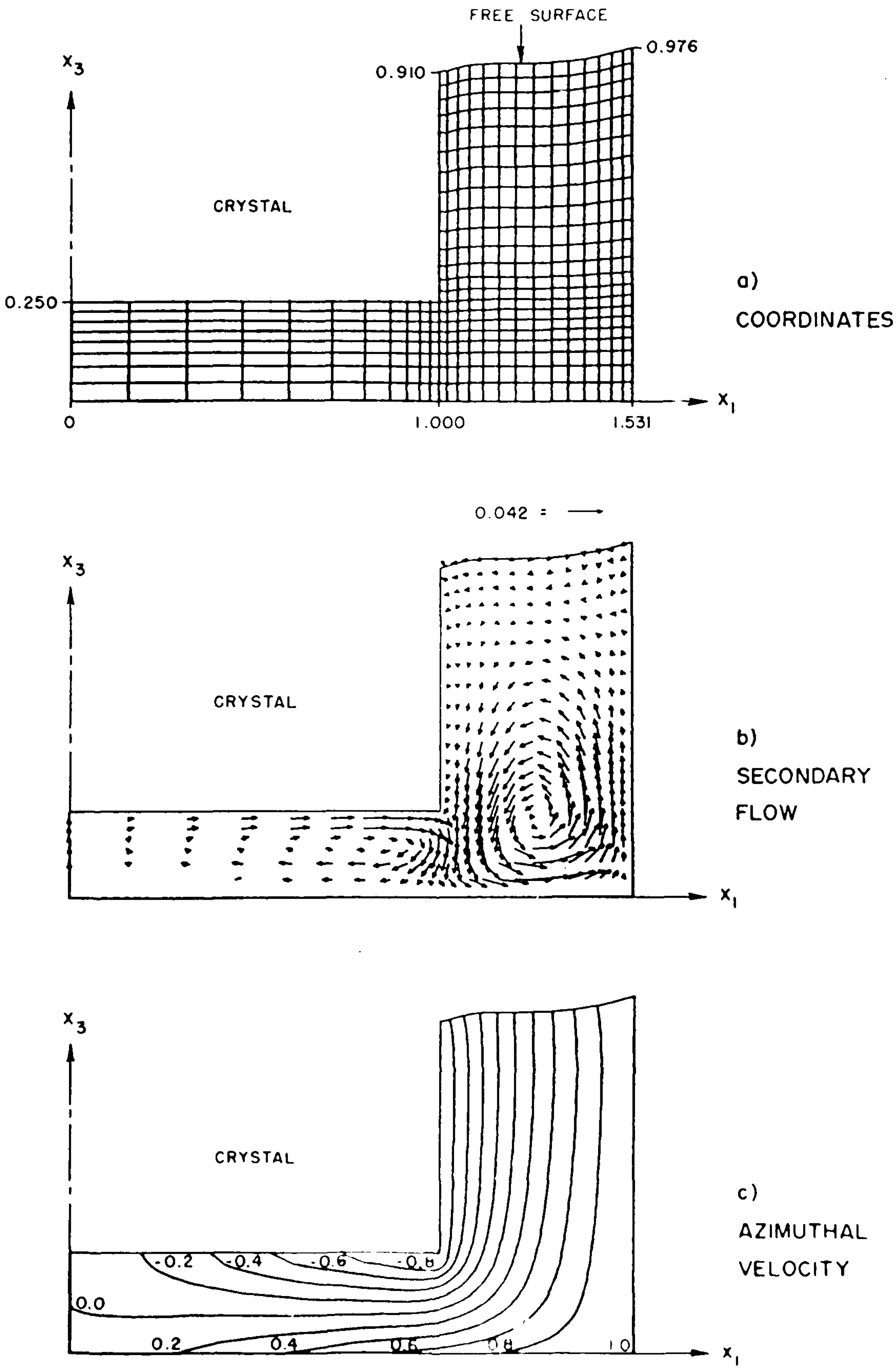

FIG. 4.2.3 - Run T1-3: ω = -0.68, δ_o = 0.25

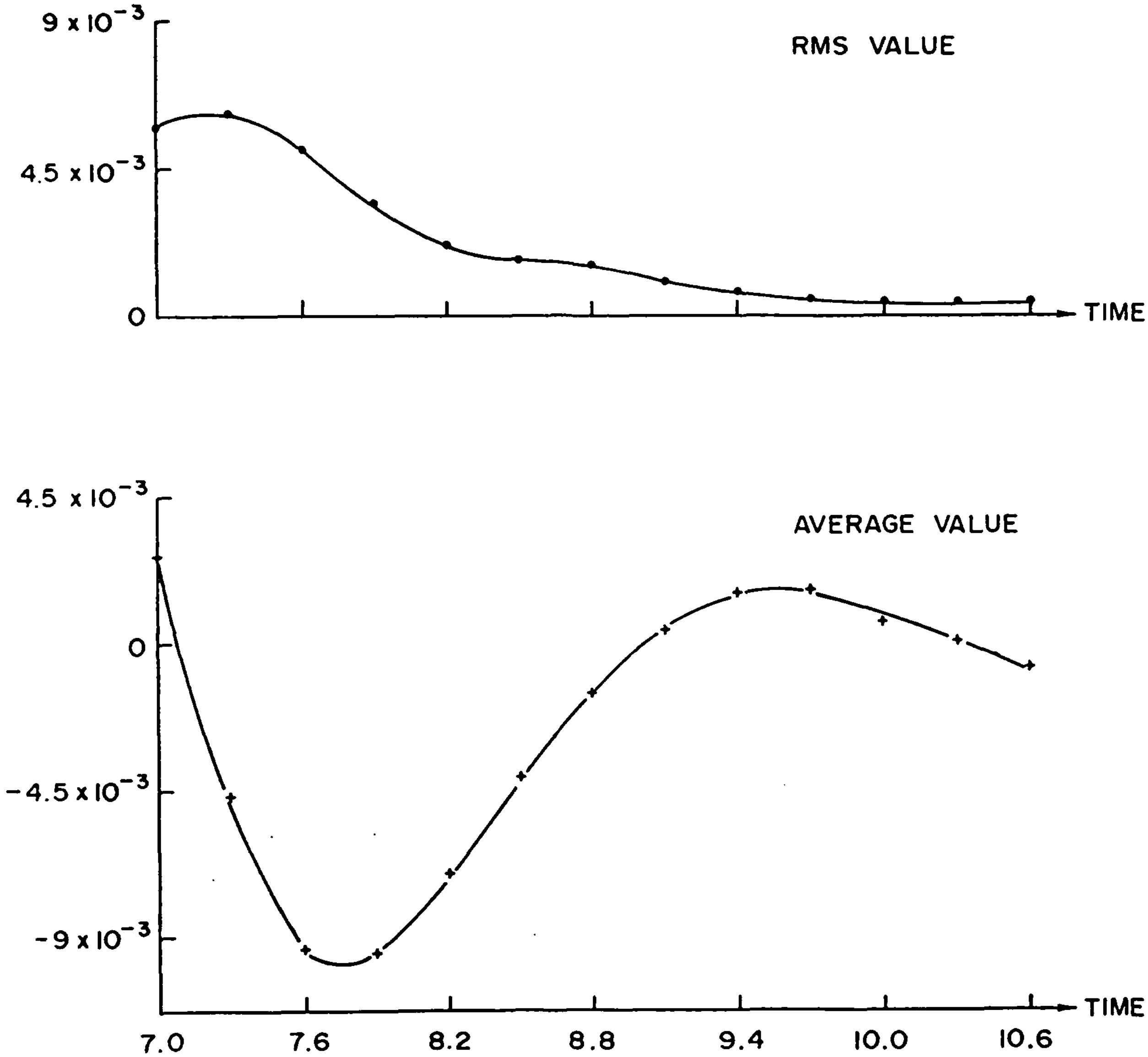

FIG. 4.2.4 - **Average and RMS Values Along the Free Surface vs. Time in a Typical Group I Study**

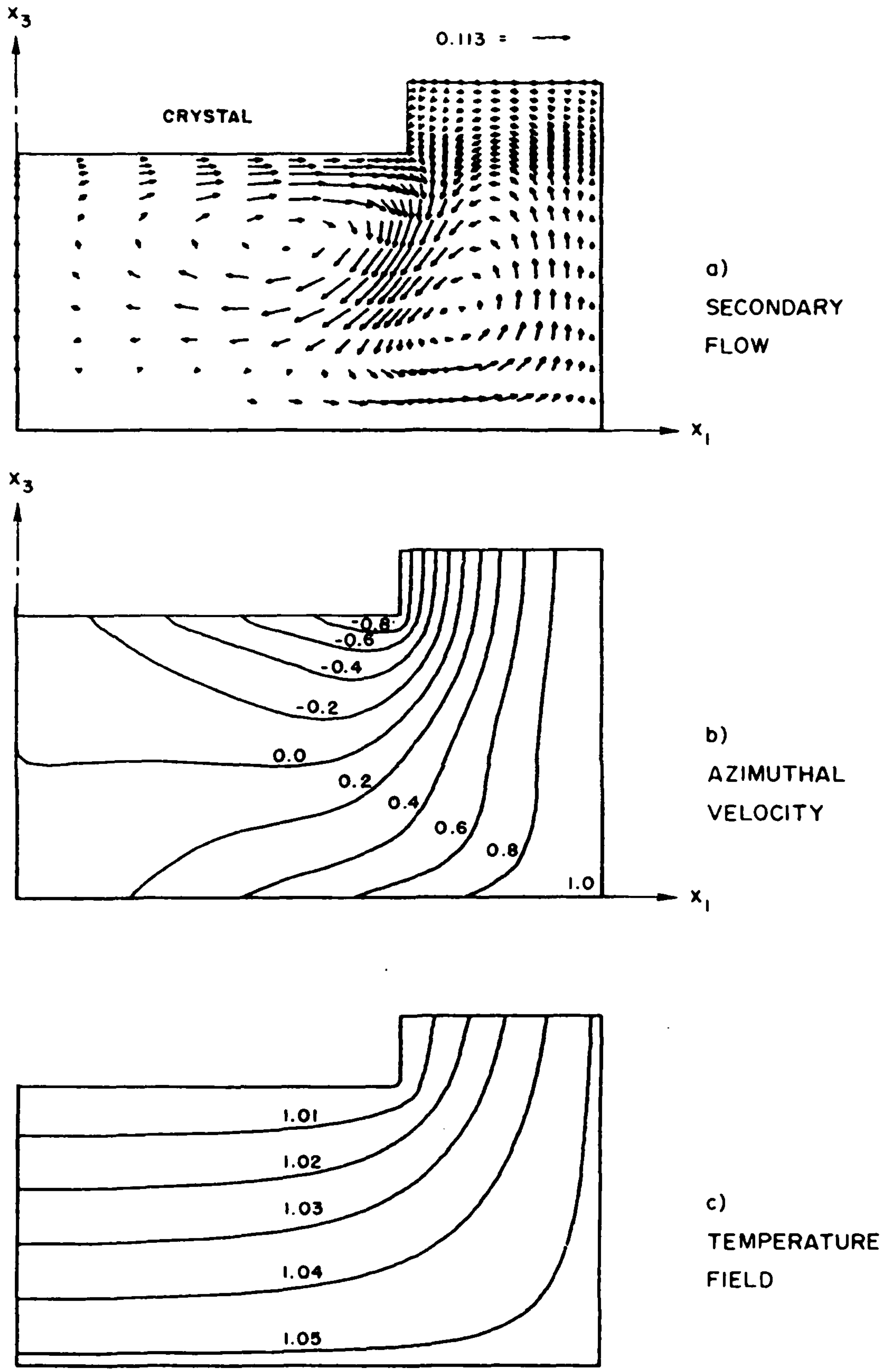

FIG. 4.3.1 - Run T2-1: $\beta = 0$, $H = 0$, $Pr = 0.054$

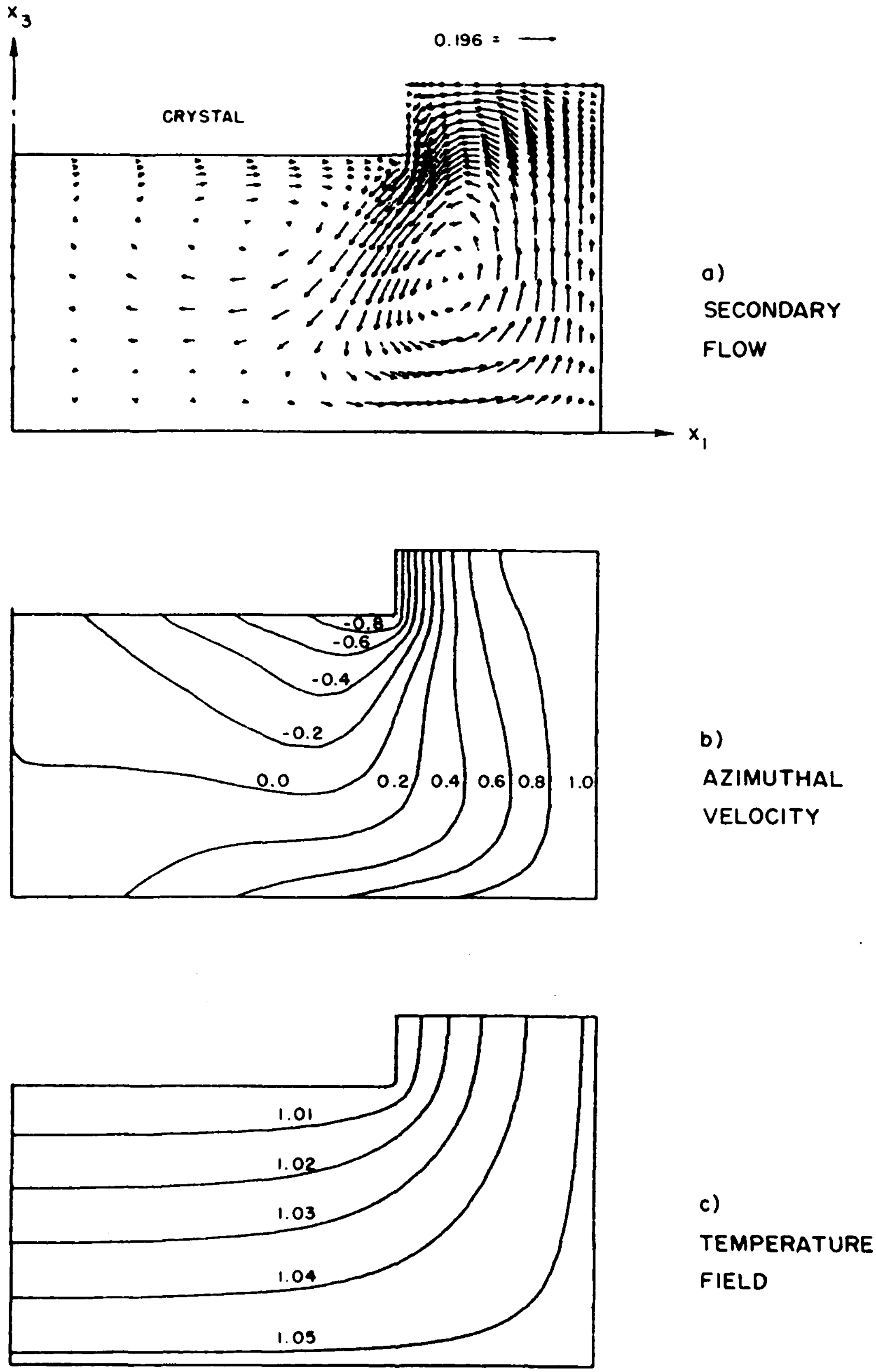

FIG. 4.3.2 - Run T2-2: $\beta = 10$, $H = 0$, $Pr = 0.054$

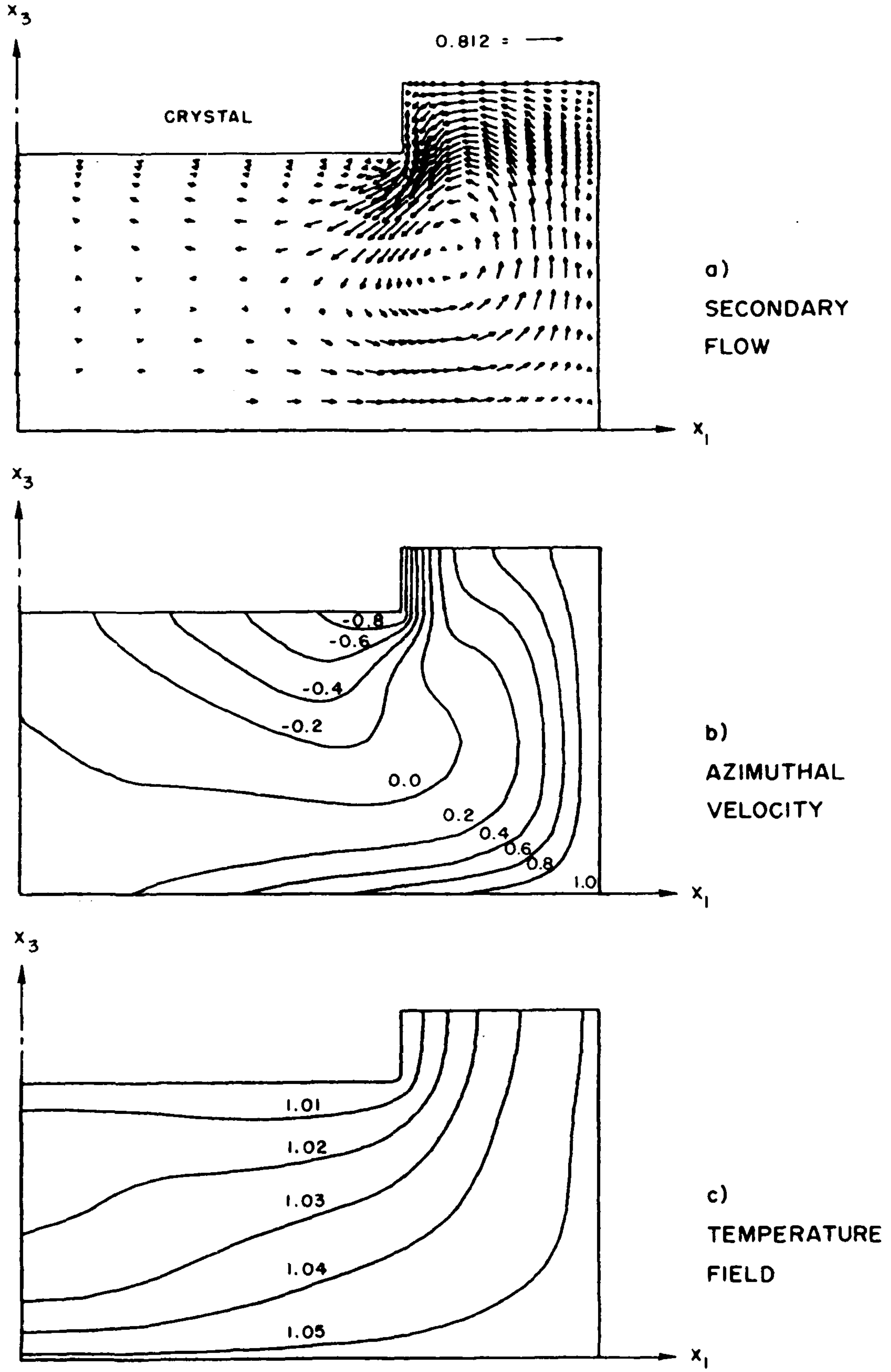

FIG. 4.3.3 - Run T2-3: $\beta = 25$, $H = 0$, $Pr = 0.054$

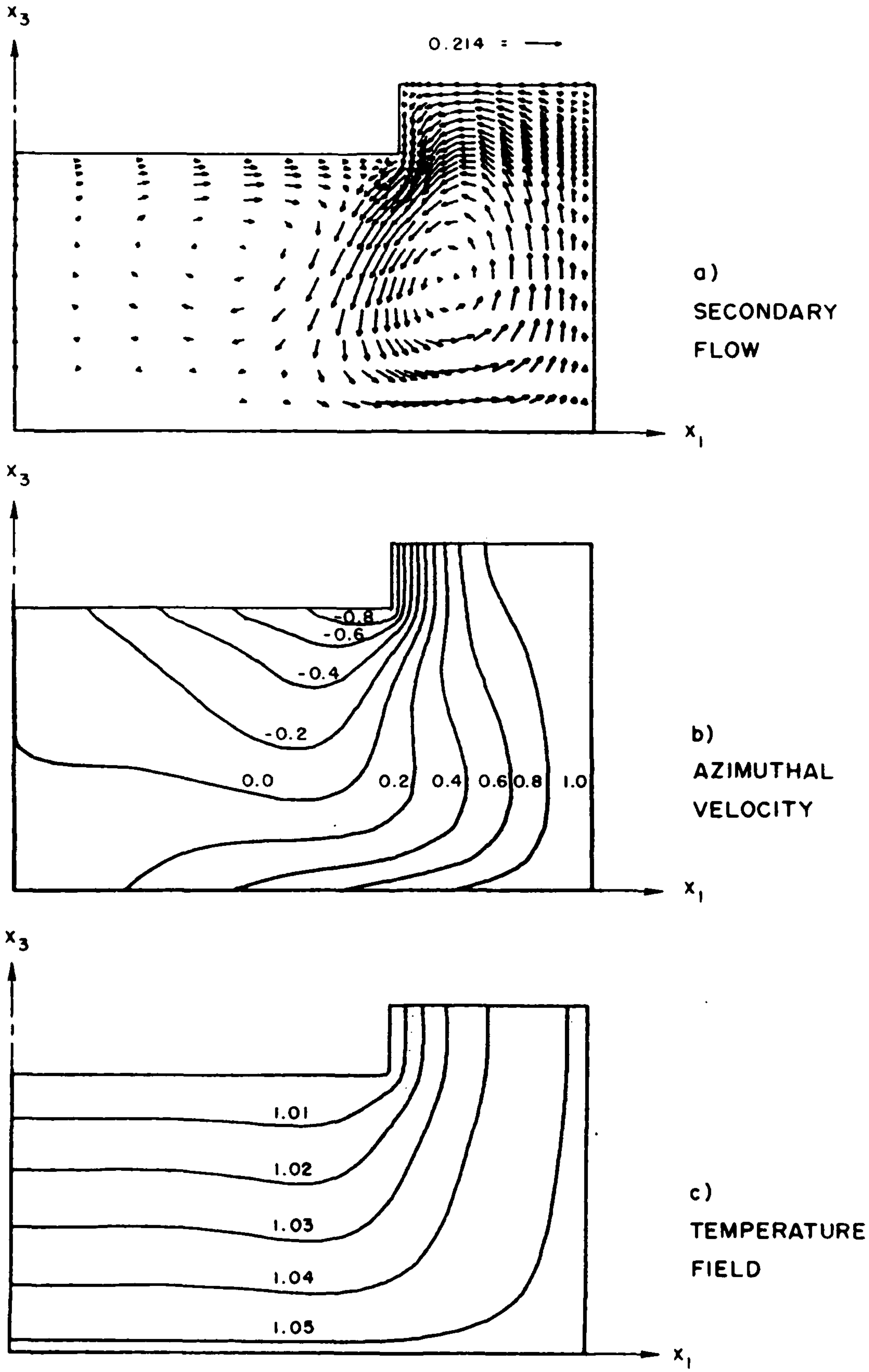

FIG. 4.3.4 - Run T2-4: $\beta = 10$, $H = 0$, $Pr = 1.0$

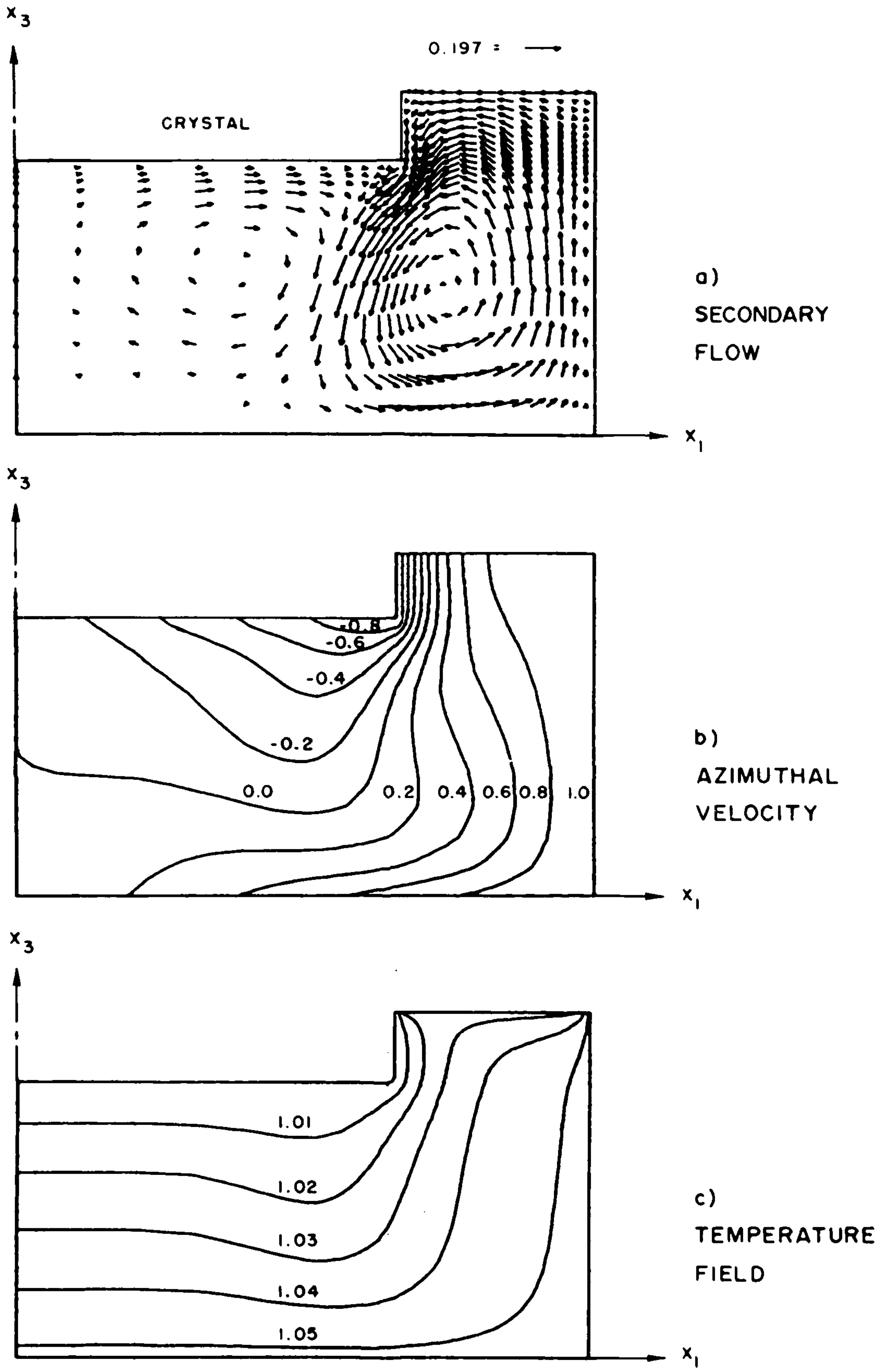

FIG. 4.3.5 - Run T2-5: β = 10, H = 10, Pr = 1.0

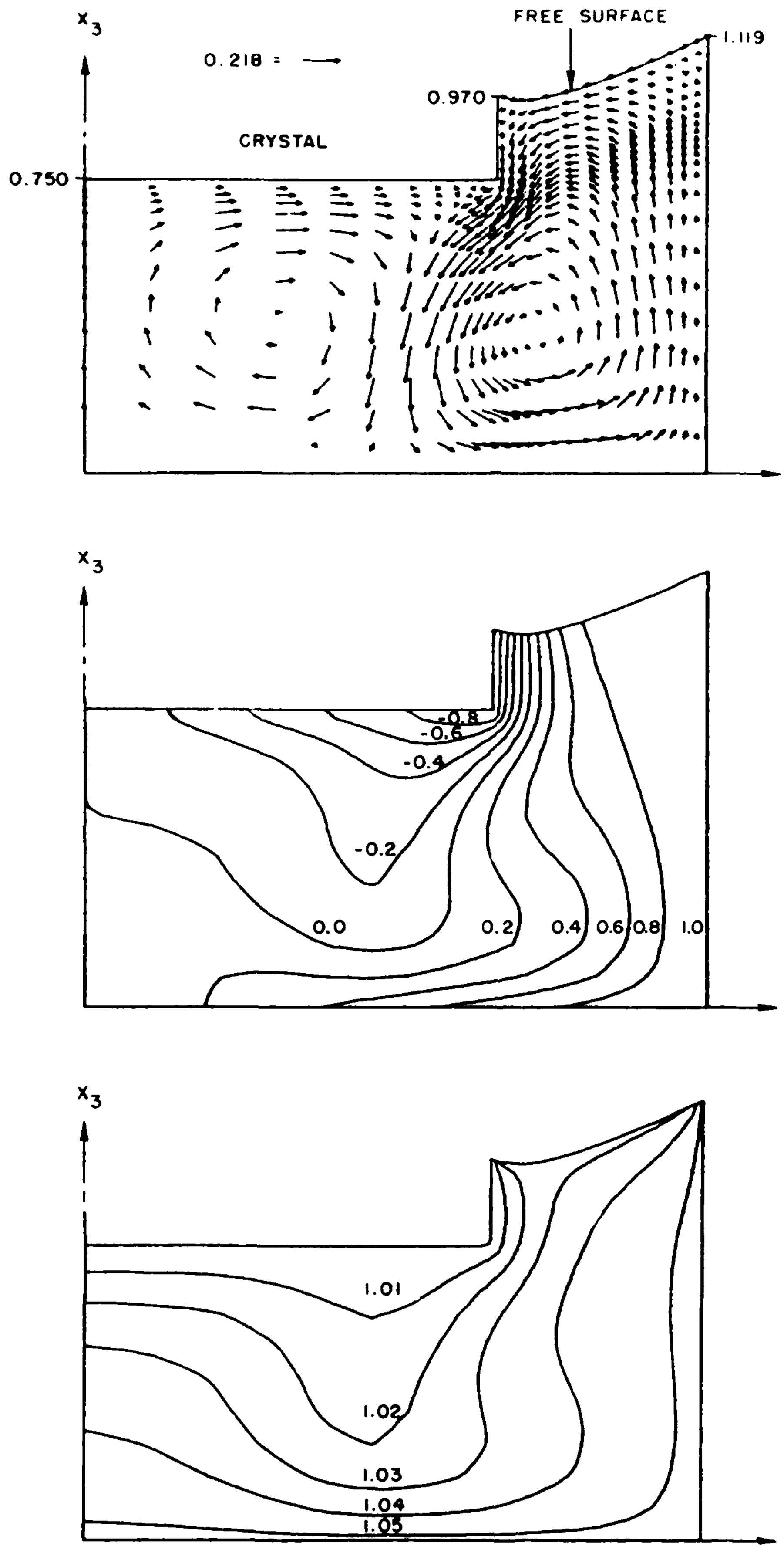

a) SECONDARY FLOW

b) AZIMUTHAL VELOCITY

c) TEMPERATURE FIELD

FIG. 4.3.6 - Run T2-6: β = 10, H = 10, Pr = 1.0, with Free Surface

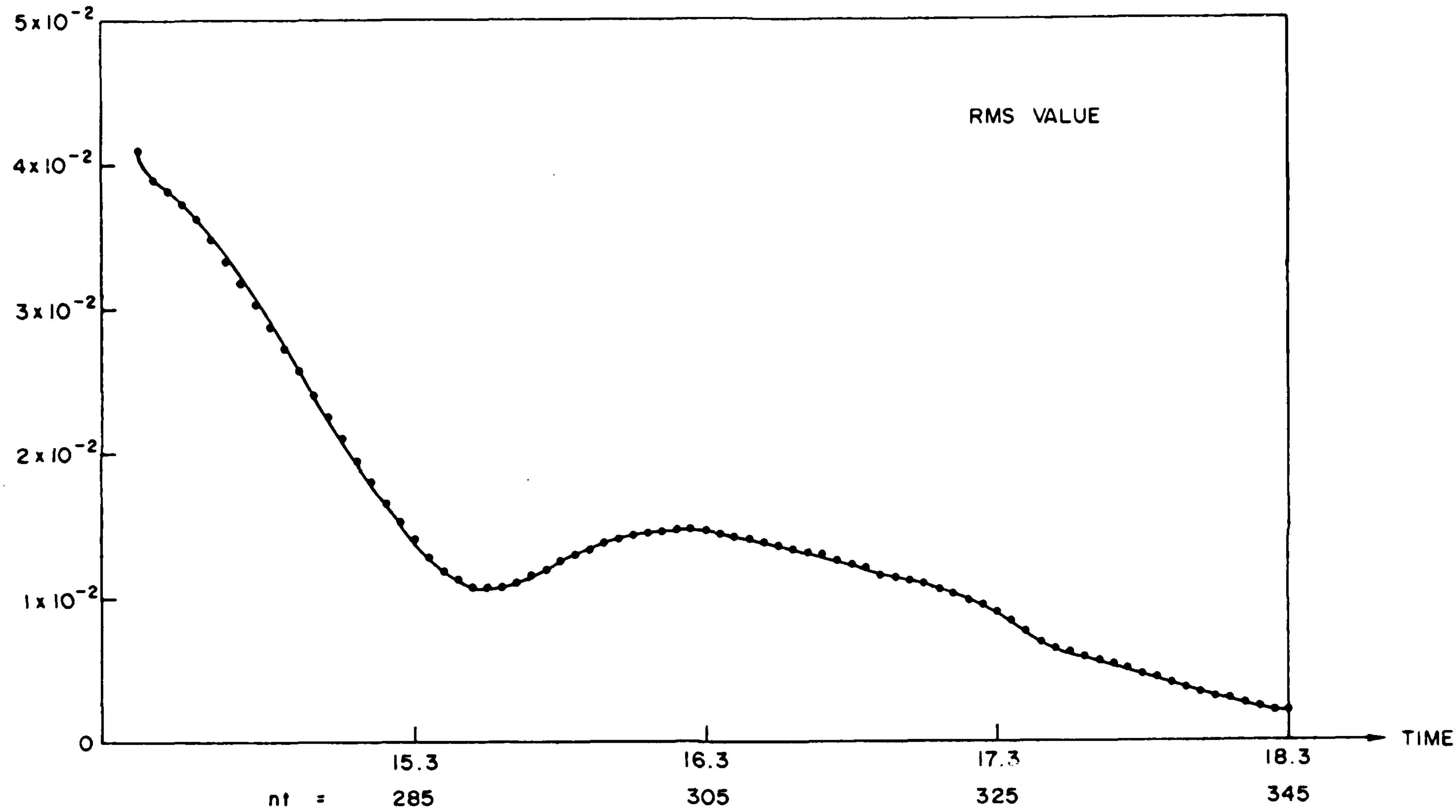

FIG. 4.3.7 - Run T2-7: $\beta = 10$, $H = 10$, $Pr = 1.0$, with Free Surface, Melt Interface

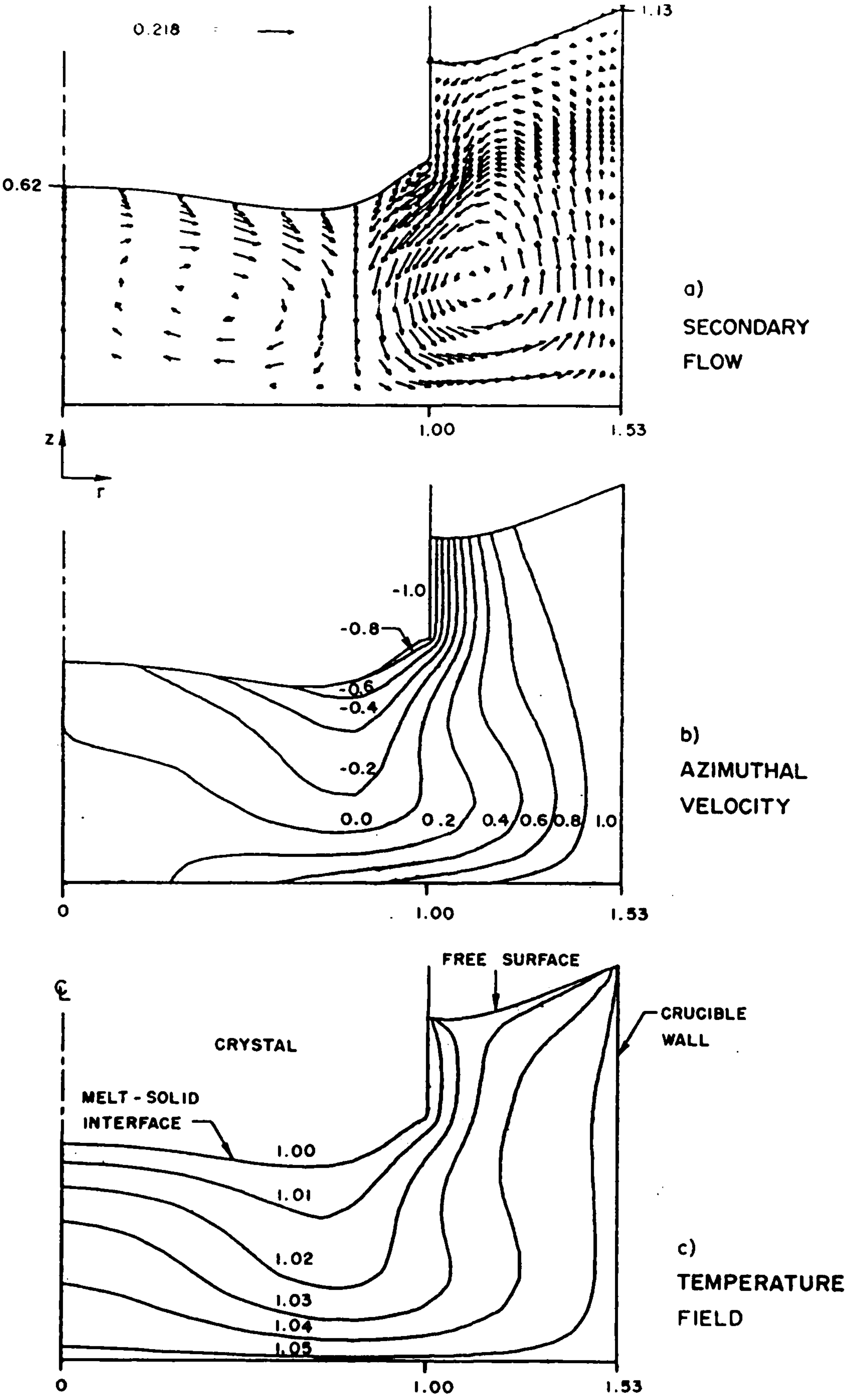

FIG. 4.3.8 - Run T2-7: $\beta = 10$, $H = 10$, $Pr = 1.0$, with Free Surface, Melt Interface and Crystal Phase

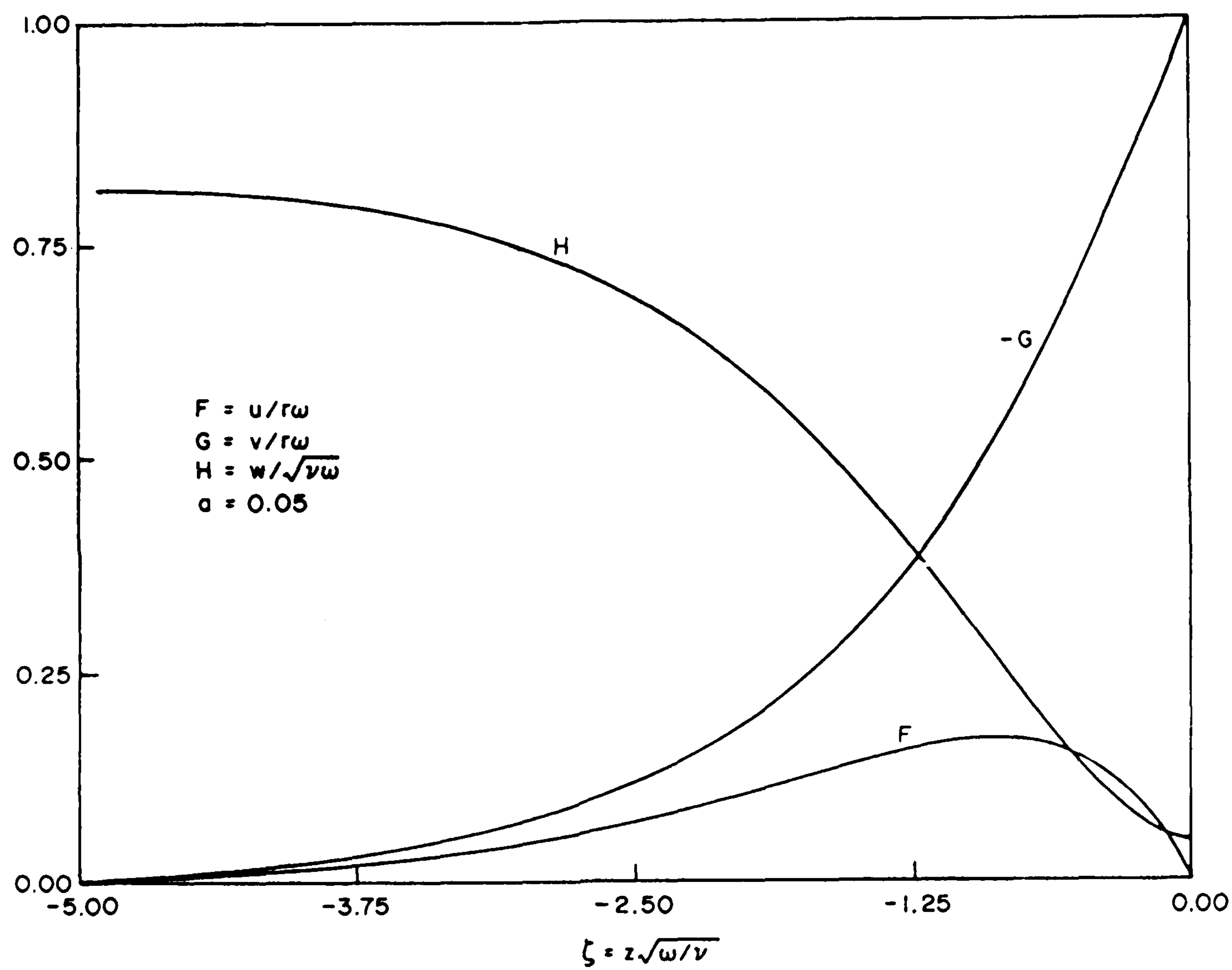

FIG. 4.4.1 - Normalized Velocities in the Thin Region Model

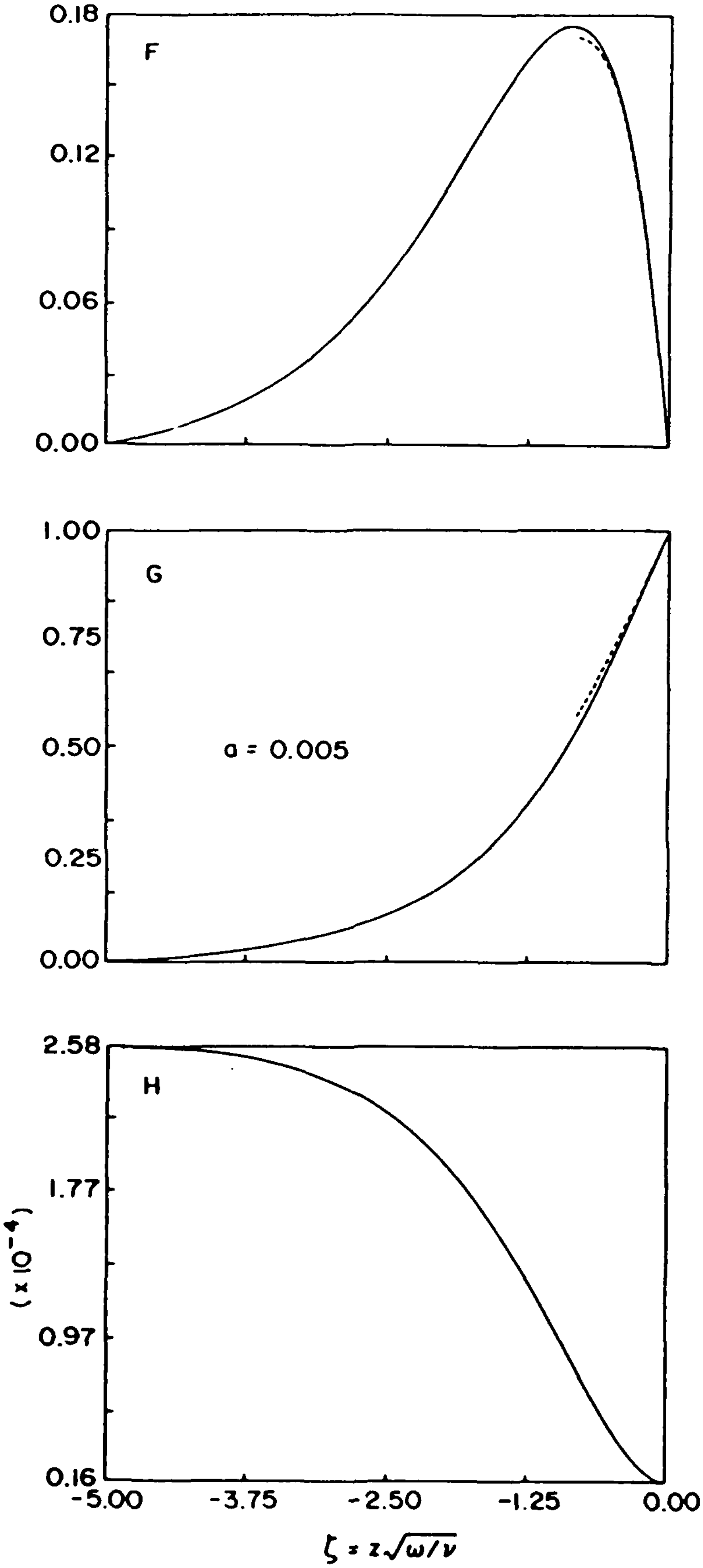

FIG. 4.4.2 - Comparison of Two Normalized Velocities Calculations:
a) Assume Quiescent Condition at $\zeta = 5$;
b) 'Bulk' Flow Conditions at $\zeta = 0.83$

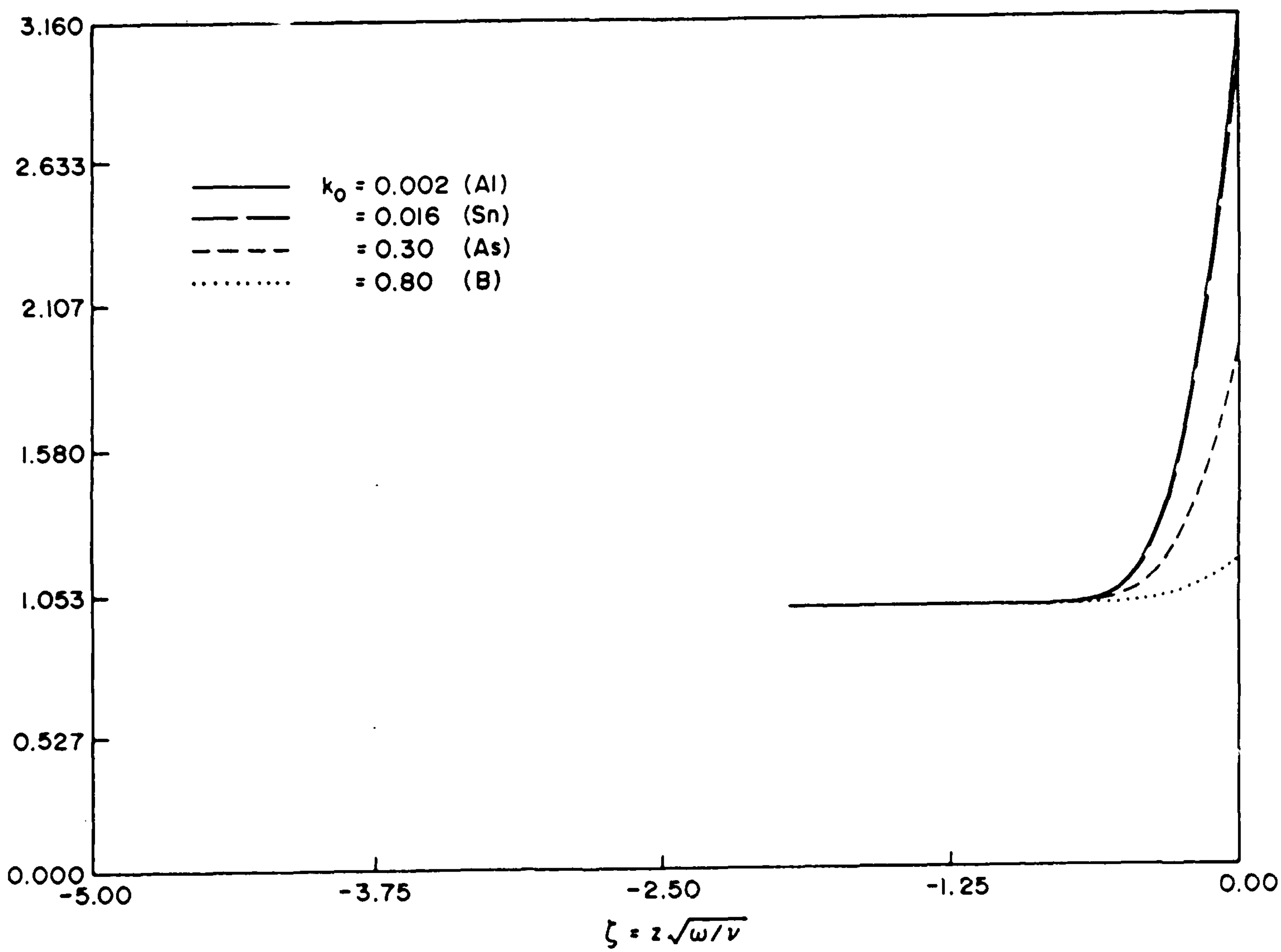

FIG. 4.4.3.a - Species Distributions for Various Dopants Using Velocity Field from Fig. 4.4.2.a

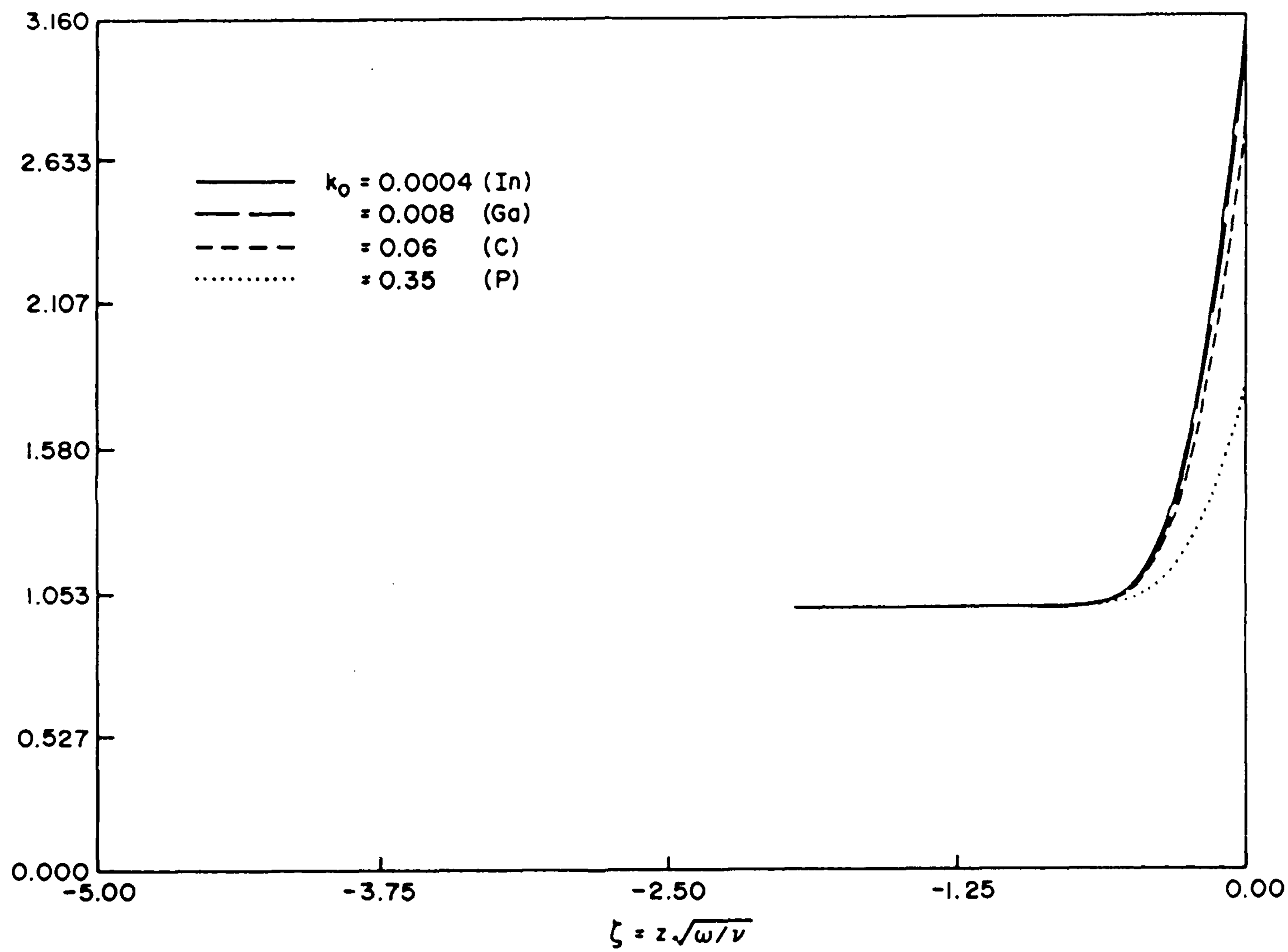

FIG. 4.4.3.b - Species Distributions for Various Dopants Using Velocity Field from Fig. 4.4.2.a

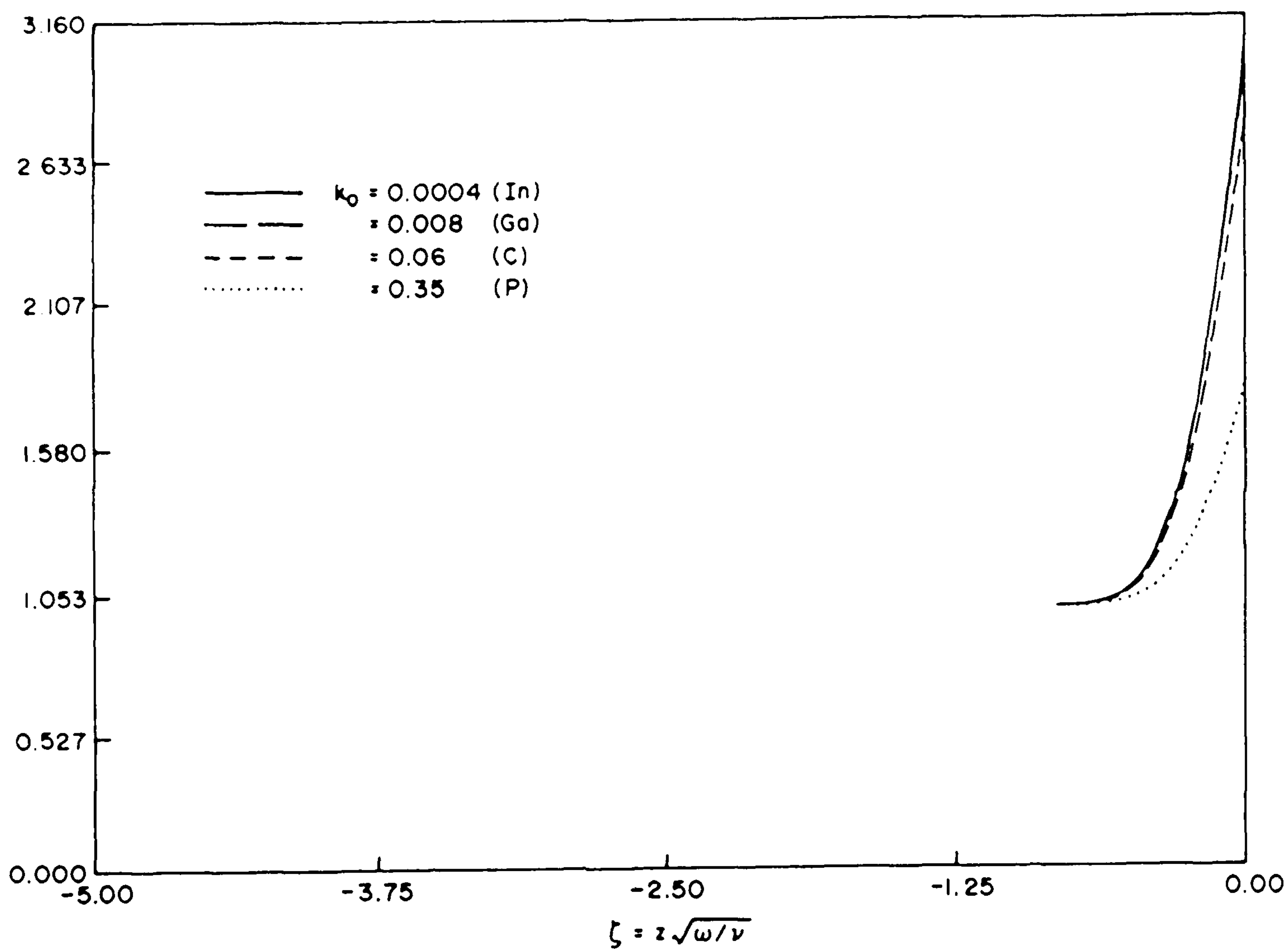

FIG. 4.4.4.a - Species Distributions for Various Dopants Using Velocity Field from Fig. 4.4.2.b

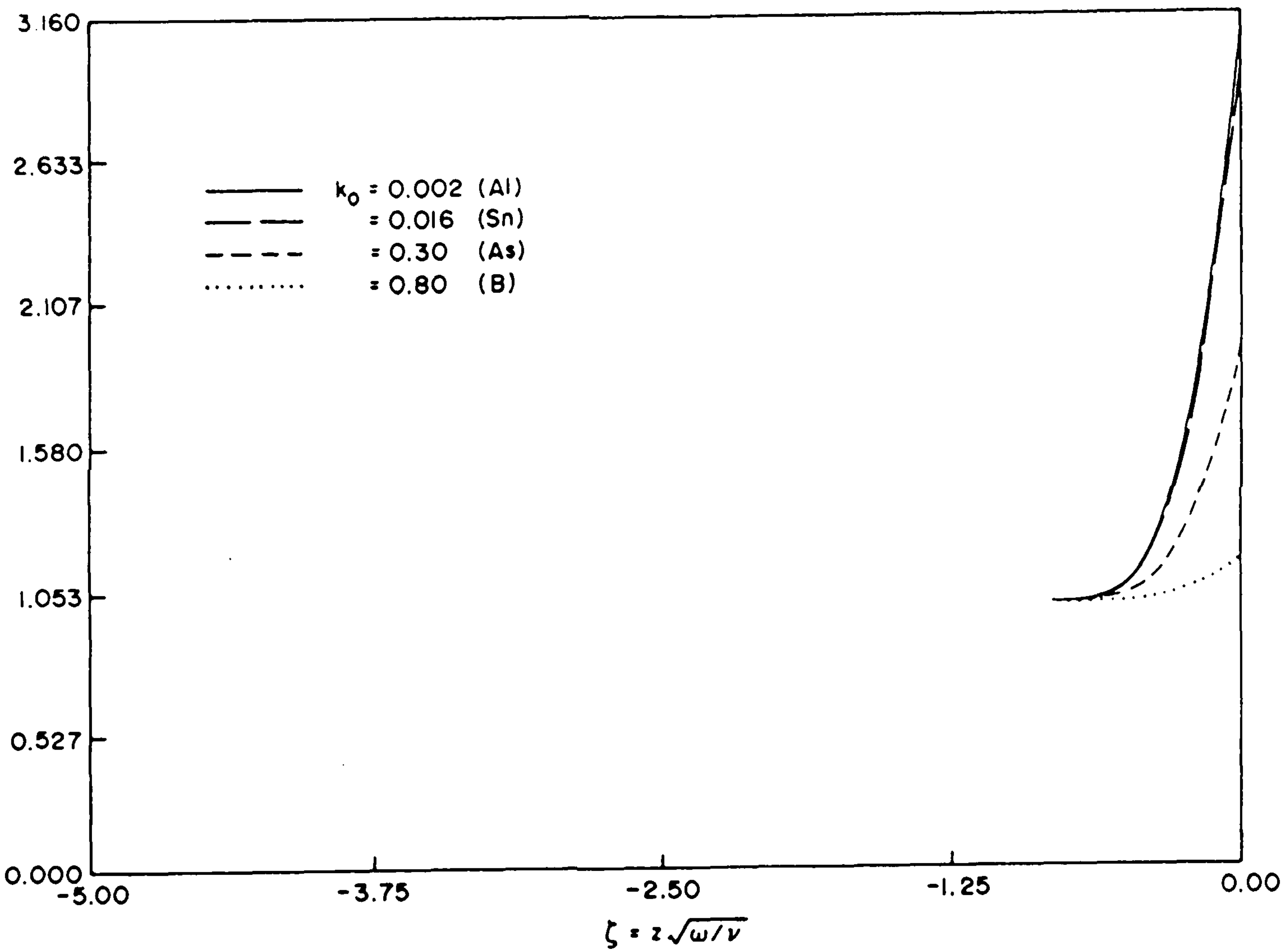

FIG. 4.4.4.b - Species Distributions for Various Dopants Using Velocity Field from Fig. 4.4.2.b

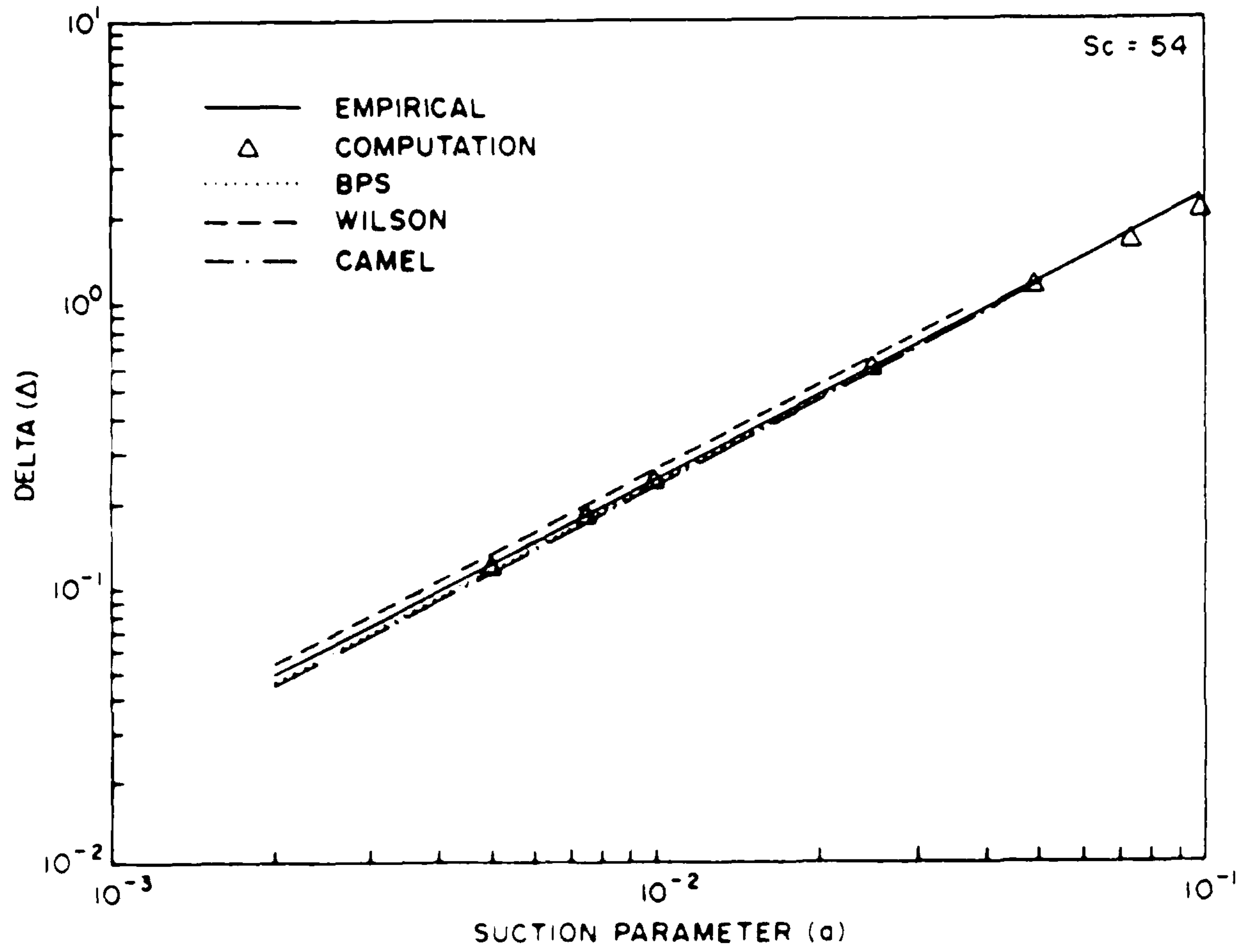

FIG. 4.4.5 - Comparison of Various Empirical Correlations

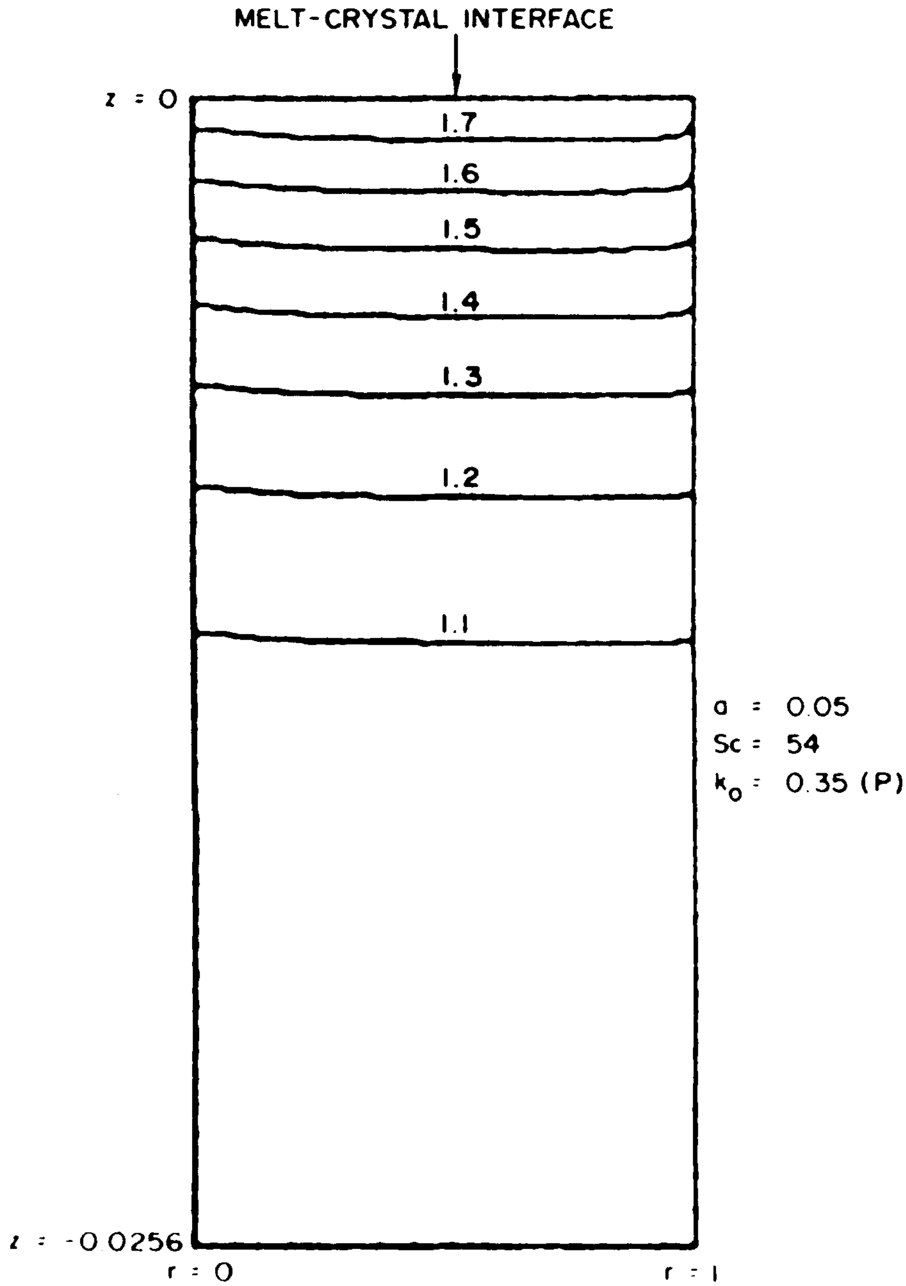

FIG. 4.4.6 - Species Distribution of Phosphorous With Constant Radial Variation Assumption Along the Boundary

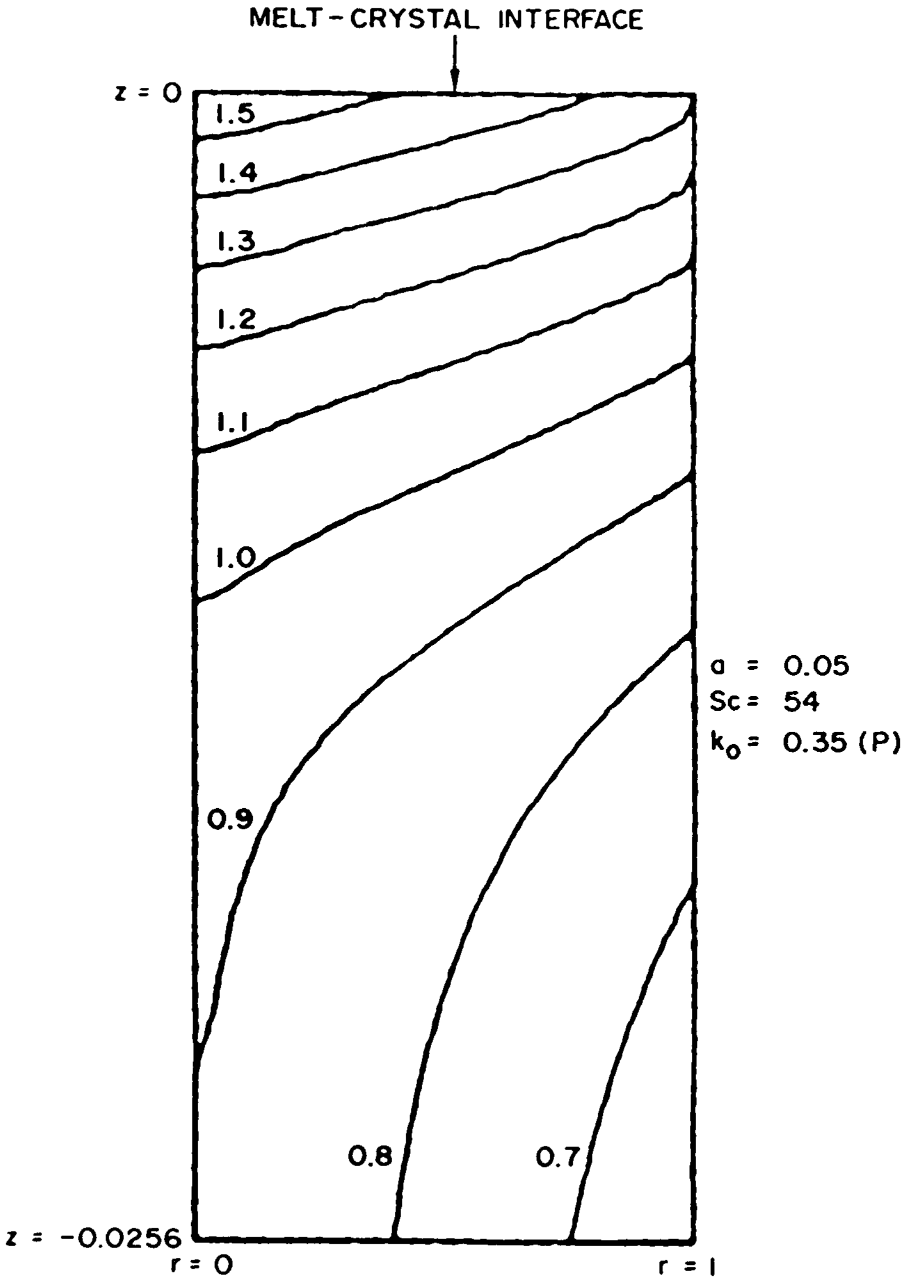

FIG. 4.4.7 - Species Distribution of Phosphorous With Bulk Flow Calculations Along the Boundary

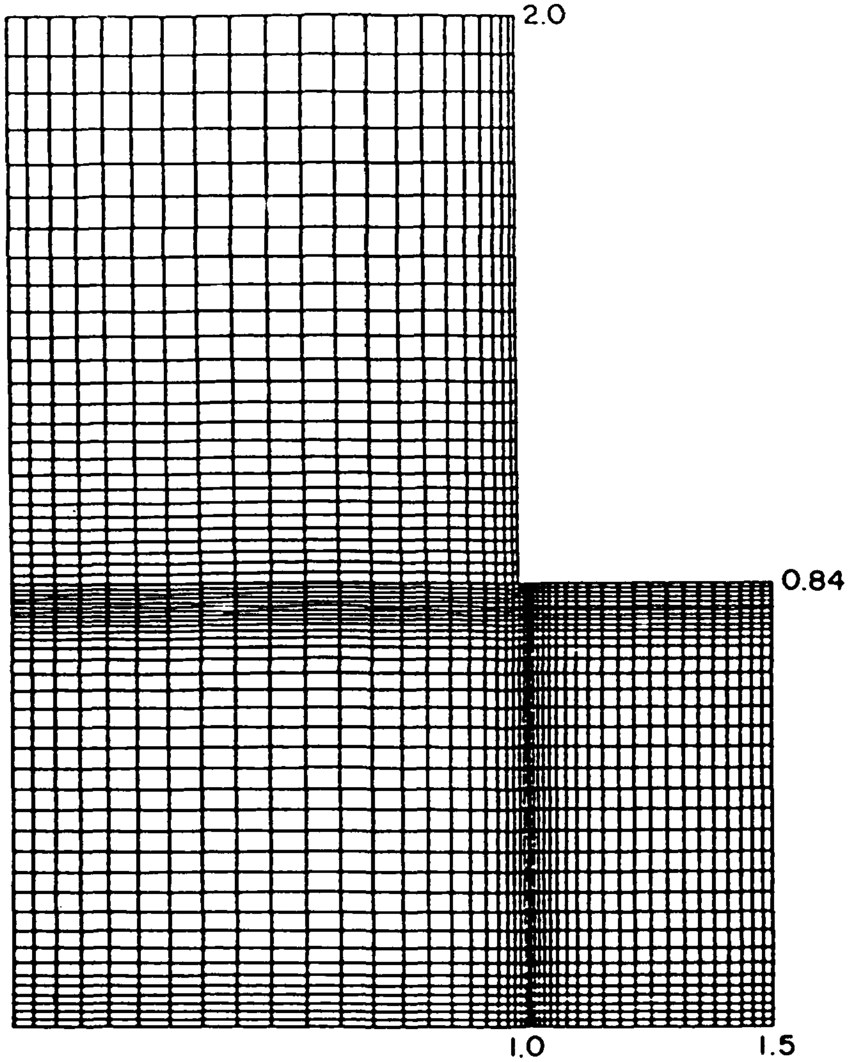

FIG. 5.1.1 - Group IV: Case 1 - Coordinates

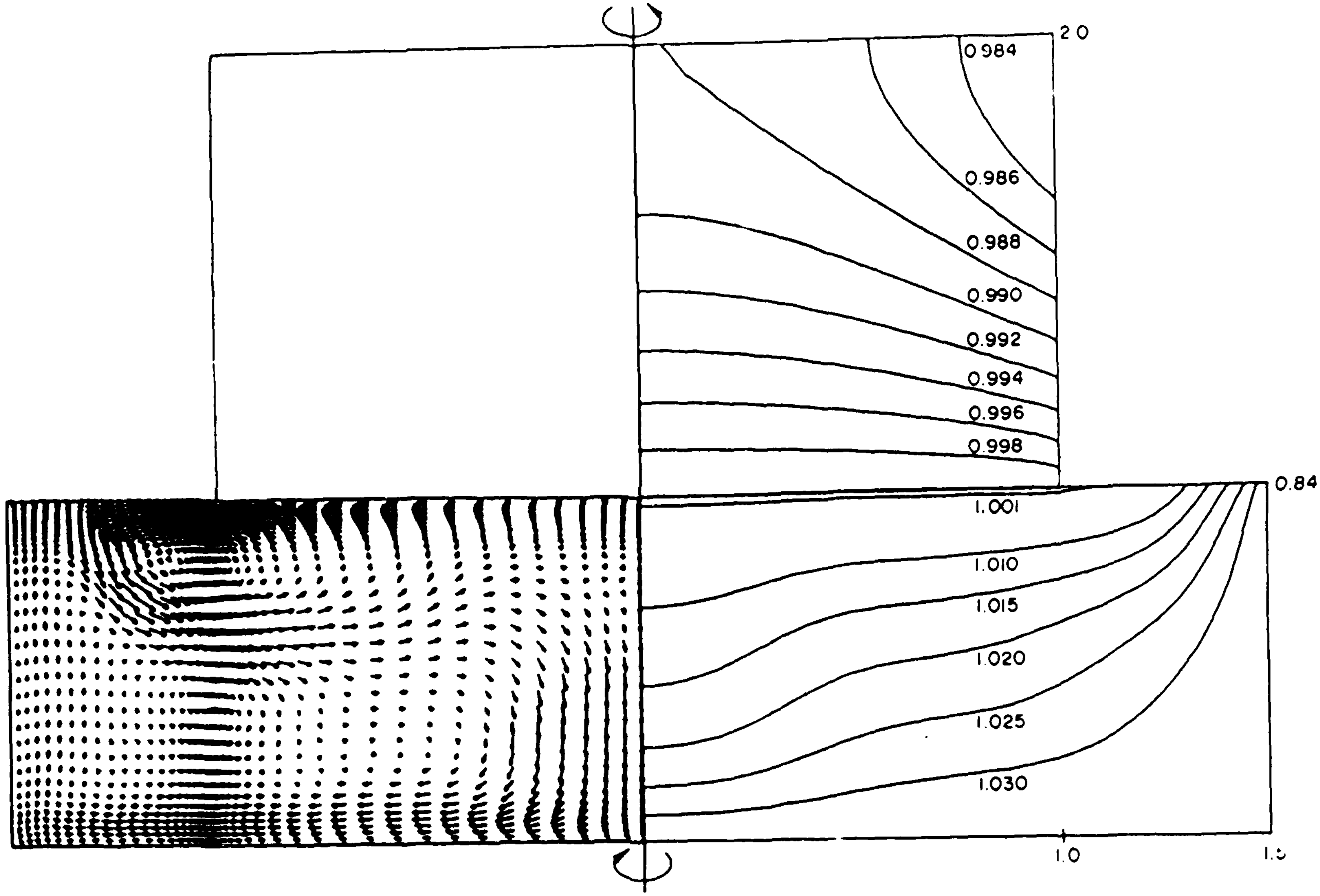

FIG. 5.1.2 - Group IV: Case 1 - Secondary Flow Field and Temperature Contours

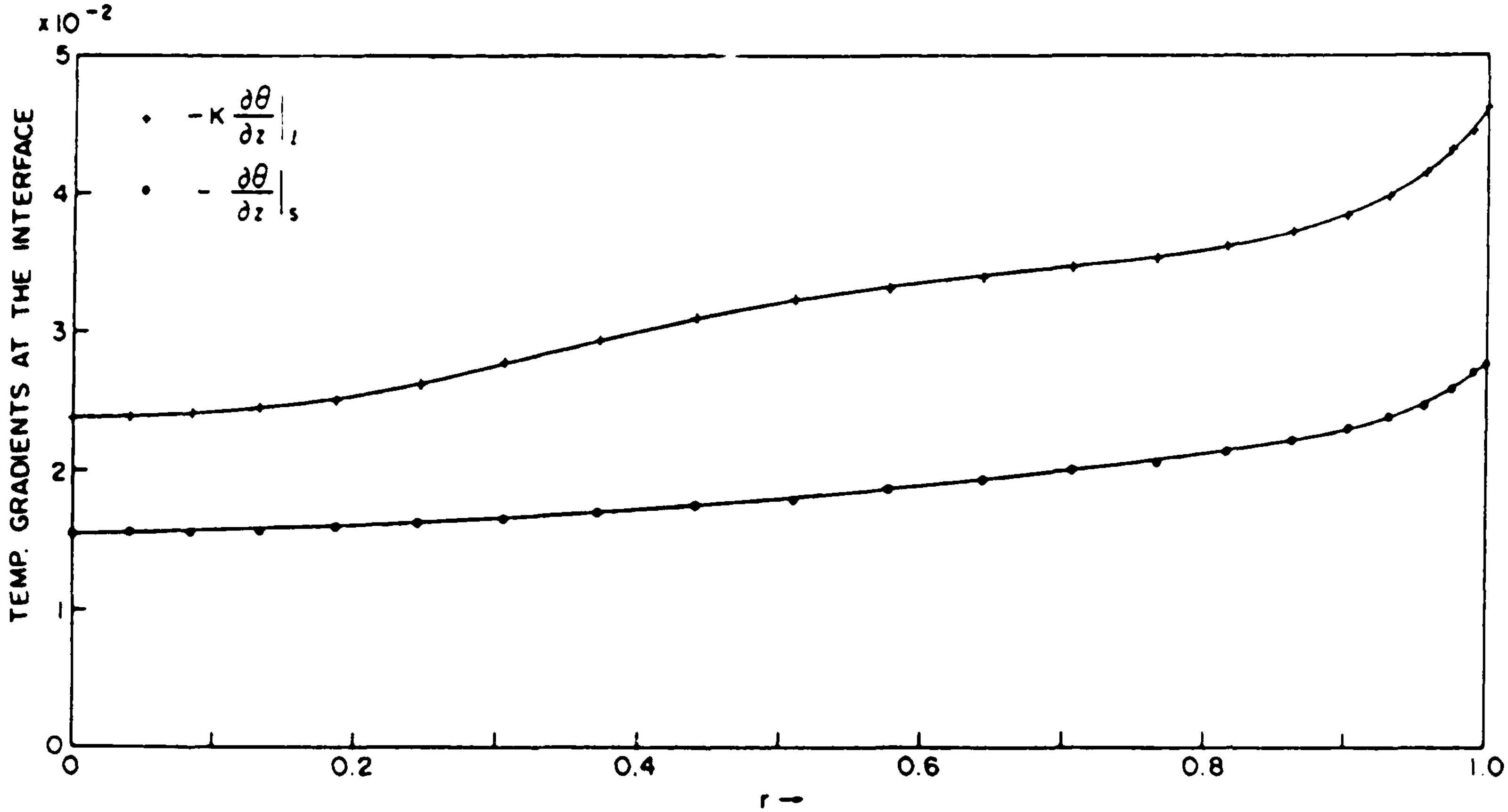

FIG. 5.1.3 - Group IV: Case 1 - Temperature Gradients of the Phases Along the Melt-Crystal Interface

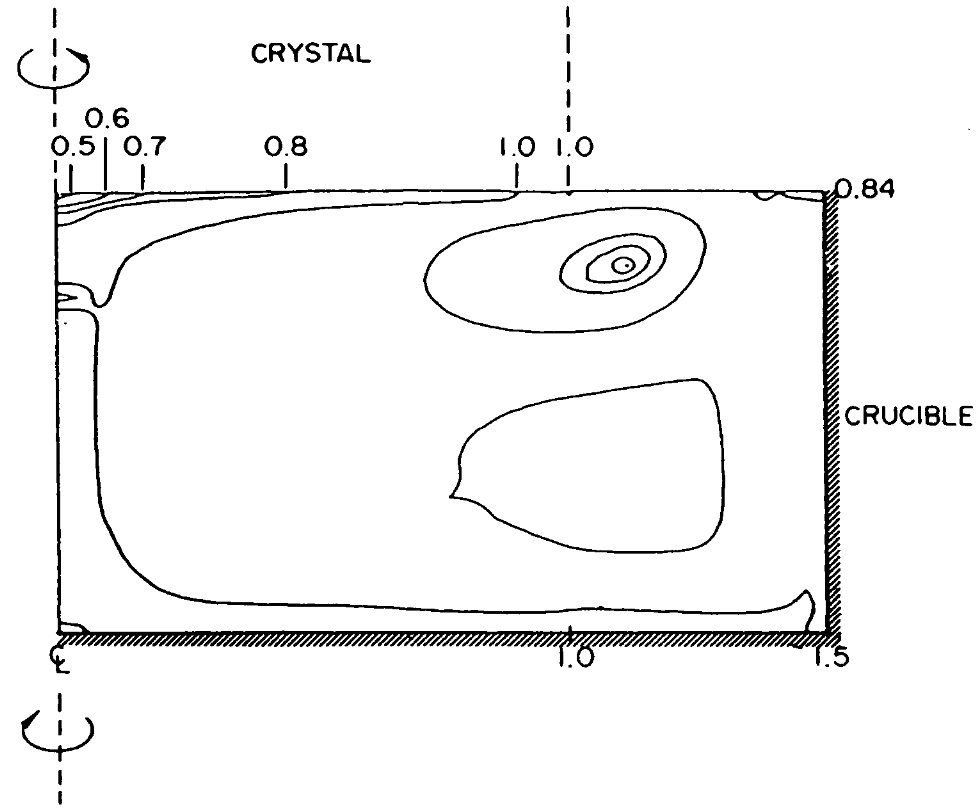

FIG. 5.1.4 - Group IV: Case 1 - Normalized Species Distribution in the Melt Phase

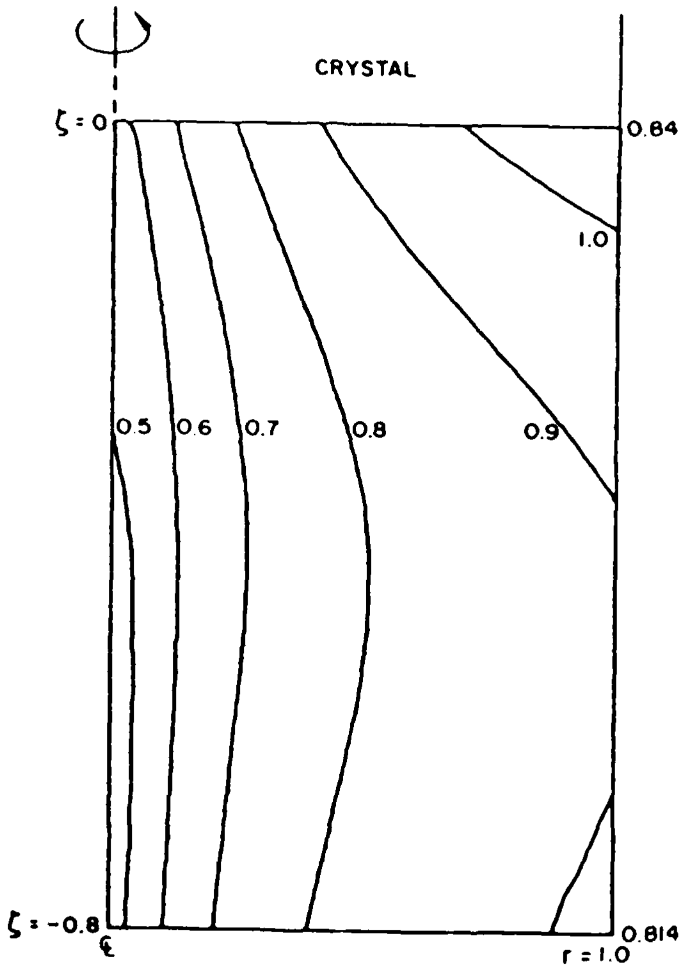

FIG. 5.1.5 - Group IV: Normalized Species Distribution in the Thin Region

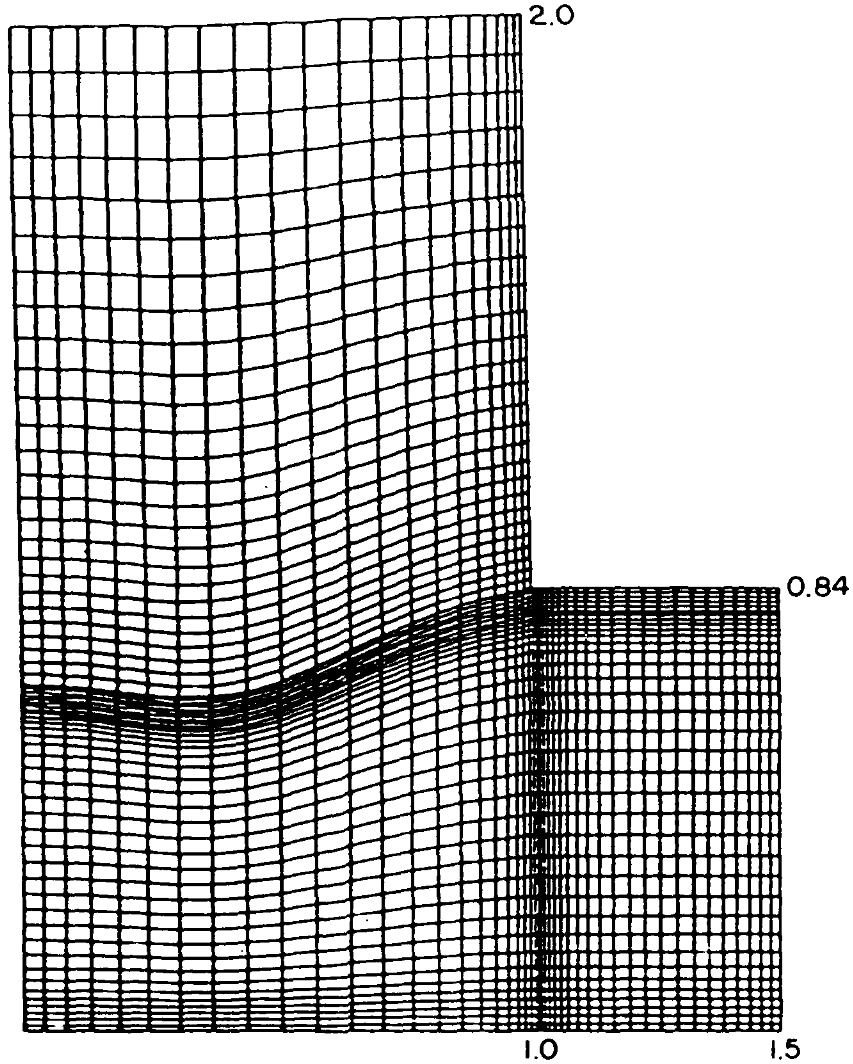

FIG. 5.1.6 - Group IV: Case 2 - Coordinates

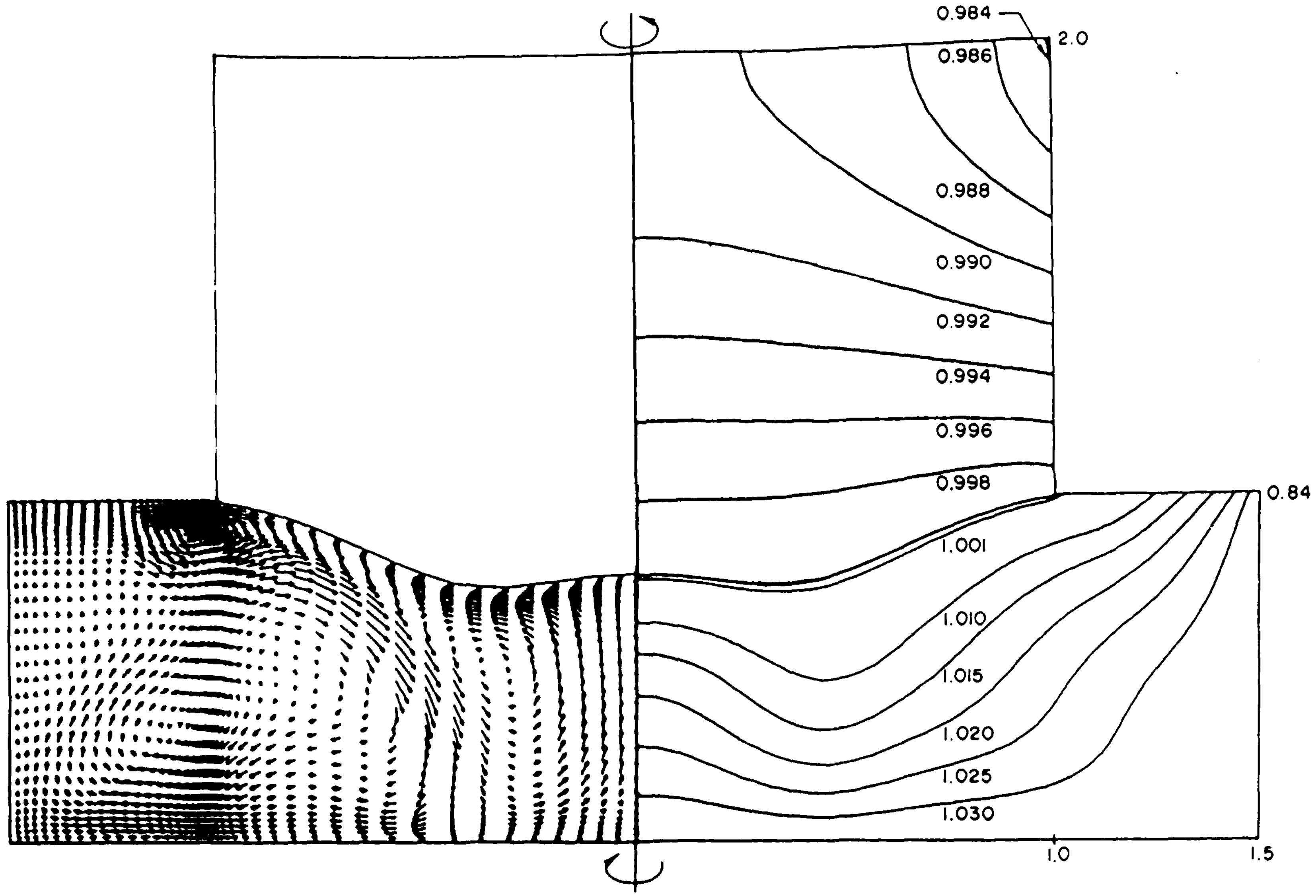

FIG. 5.1.7 - Group IV: Case 2 - Secondary Flow Field and Temperature Contours

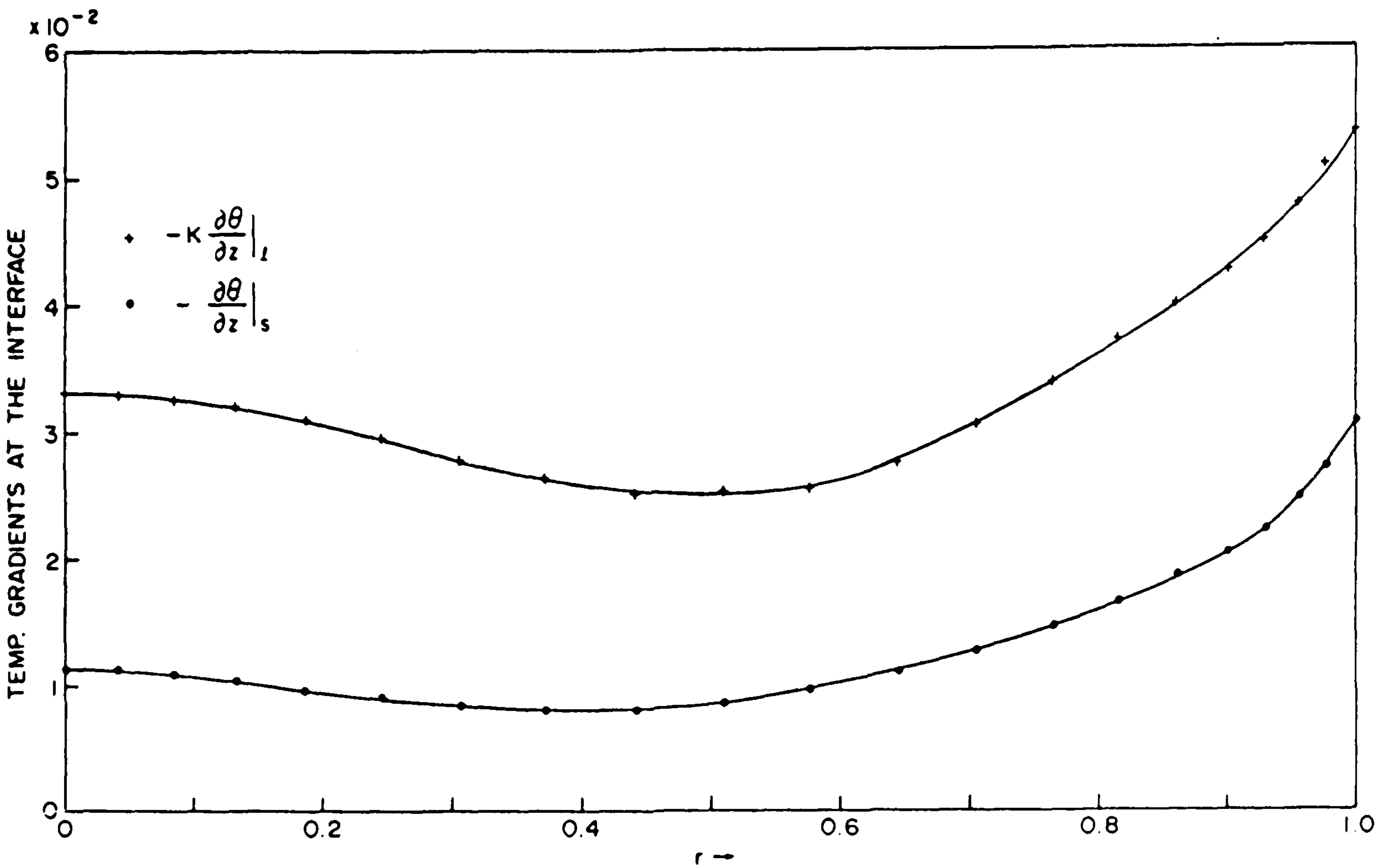

FIG. 5.1.8 - Group IV: Case 2 - Temperature Gradients of the Phases Along the Melt-Crystal Interface

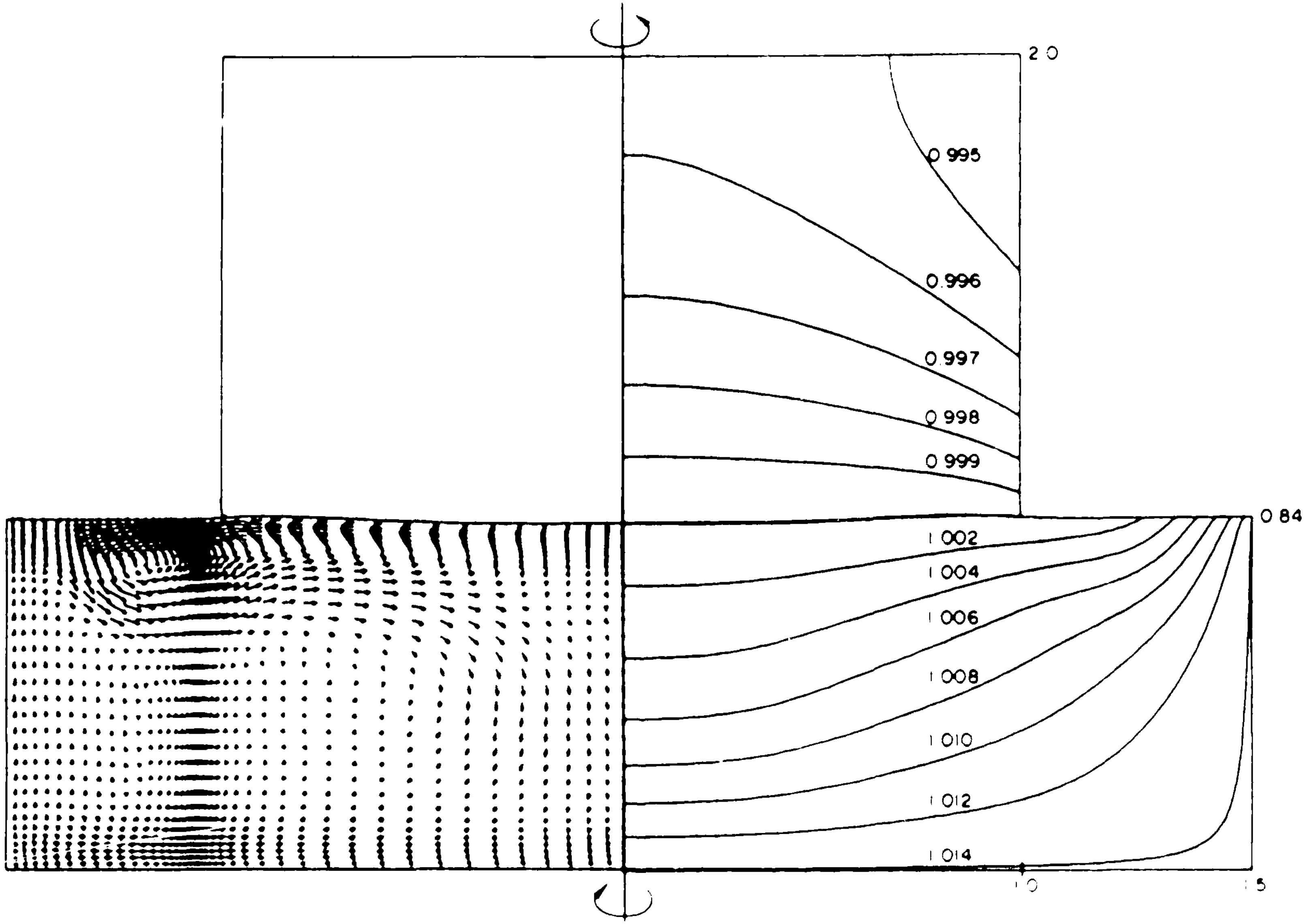

FIG. 5.1.9 - Group IV: Case 3 - Secondary Flow Field and Temperature Contours

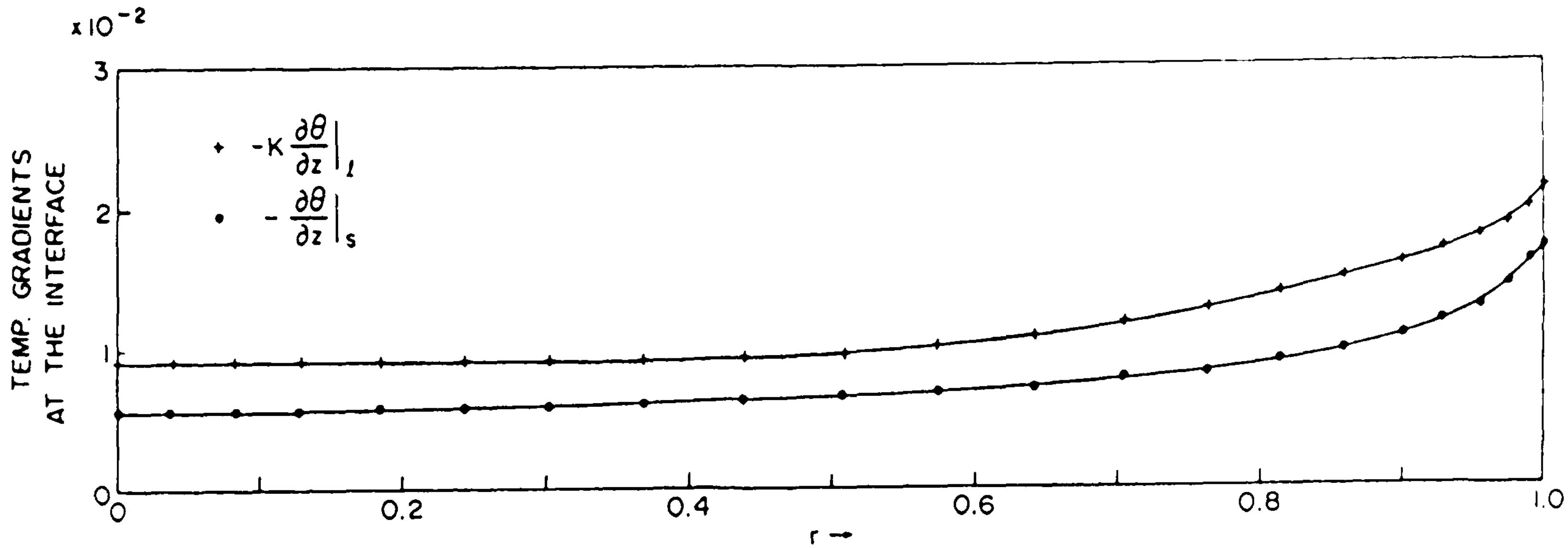

FIG. 5.1.10 - Group IV: Case 3 - Temperature Gradients of the Phases Along the Melt-Crystal Interface

AD-A176 888 THREE-DIMENSIONAL NUMERICAL STUDIES OF THE PHYSICS OF SEMICONDUCTOR CRYST (U) SCIENTIFIC RESEARCH ASSOCIATES INC GLASTONBURY CT Y T CHAN ET AL FEB 87 2/2

UNCLASSIFIED SRA-R-920018-F N00014-83-C-0510 F/G 20/12 NL

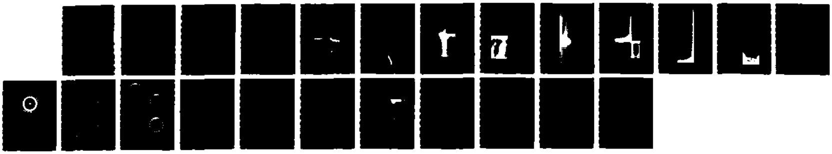

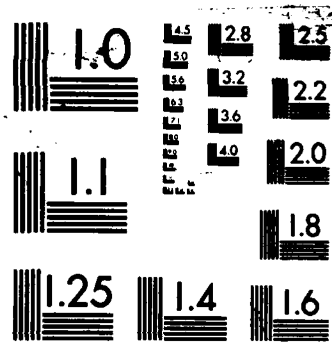

MICROCOPY RESOLUTION TEST CHART
NATIONAL BUREAU OF STANDARDS-1963-A

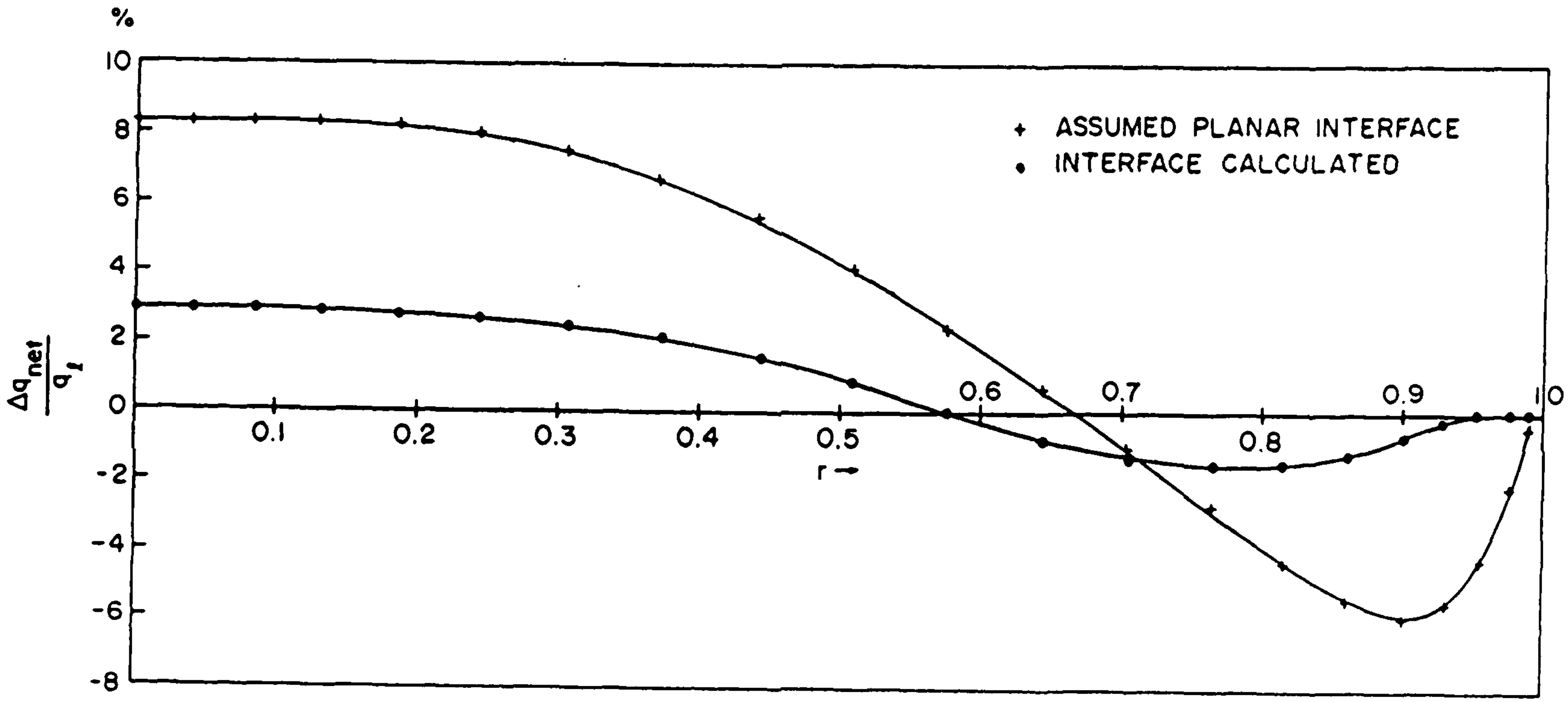

FIG. 5.1.11 - Group IV: Comparison of Heat Fluxes Between
Cases 2 and 3 Along the Melt-Crystal Interface

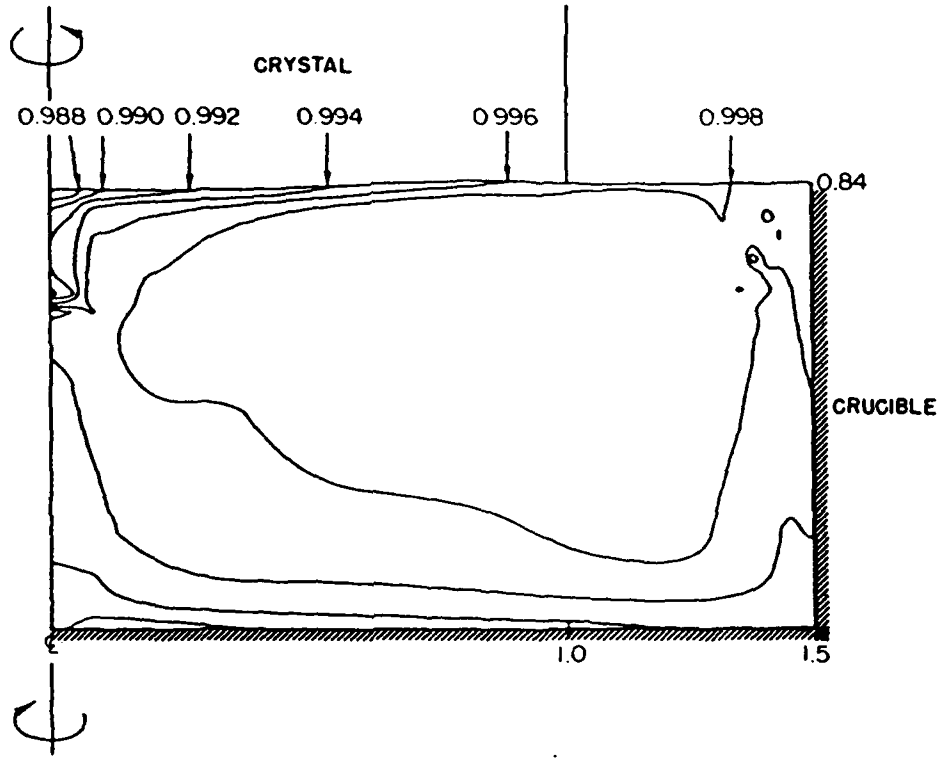

FIG. 5.1.12 - Group IV: Case 3 - Normalized Species Distribution in the Melt Phase

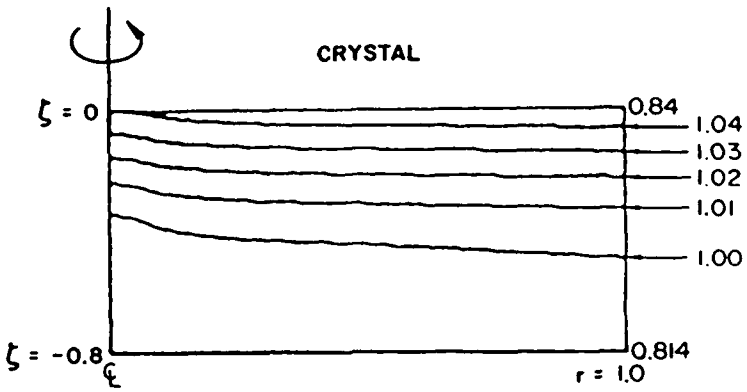

FIG. 5.1.13 - Group IV: Case 3 - Normalized Species Distribution in the Thin Region

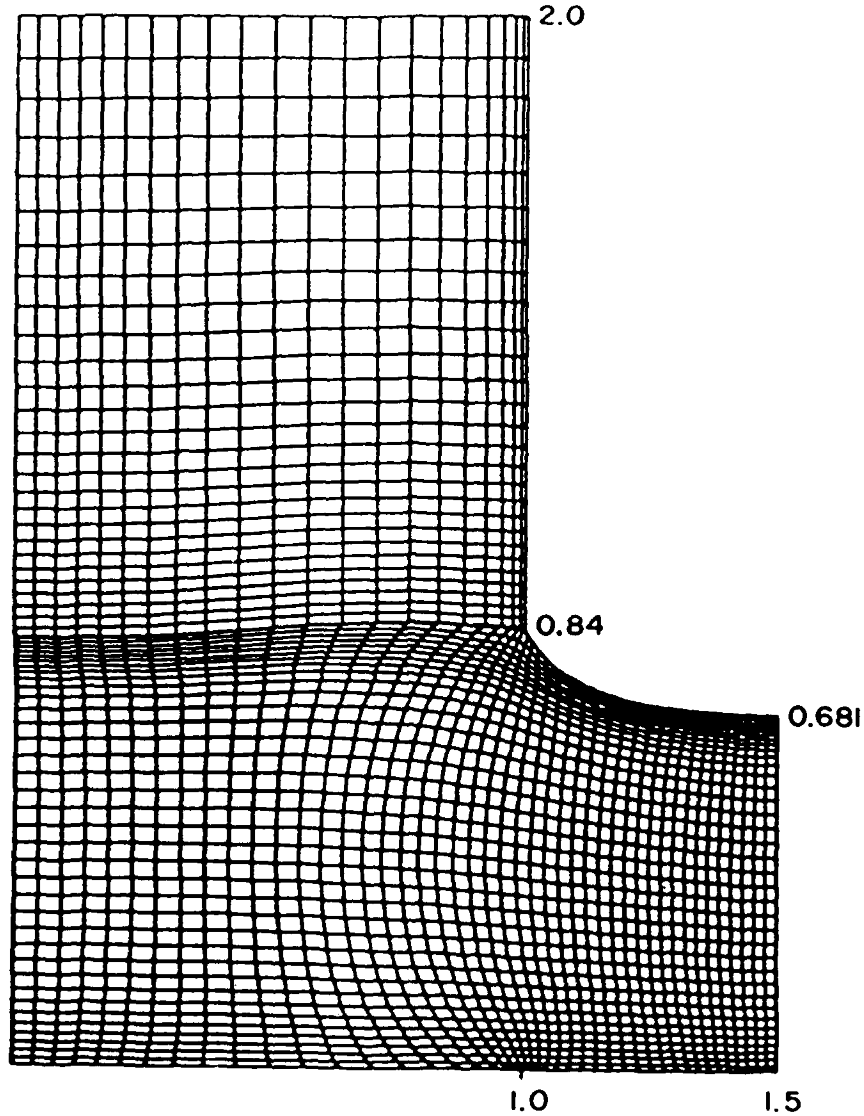

FIG. 5.1.14 - Group IV: Case 4 - Coordinates

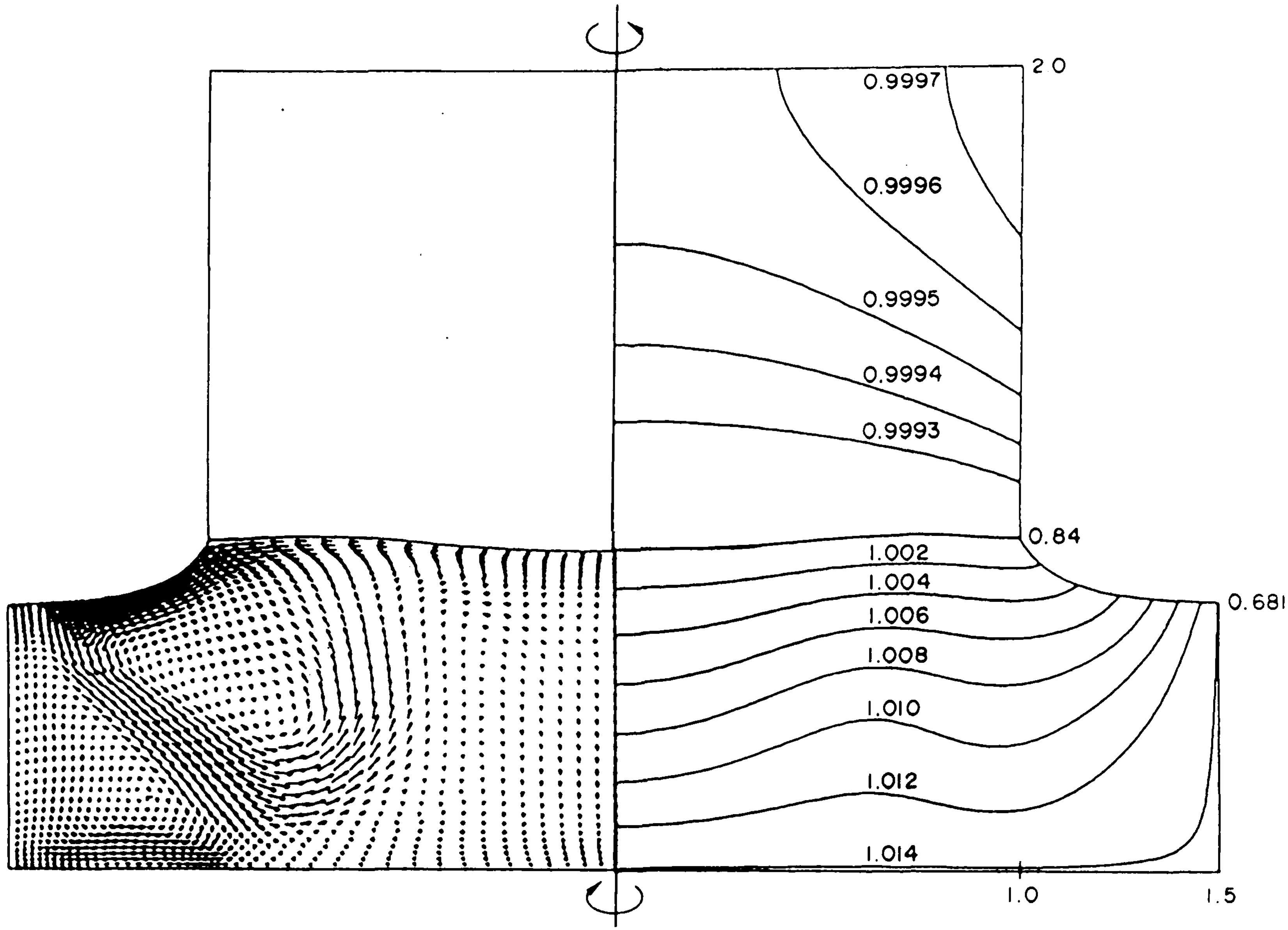

FIG. 5.1.15 - Group IV: Case 4 - Secondary Flow Field and Temperature Contours

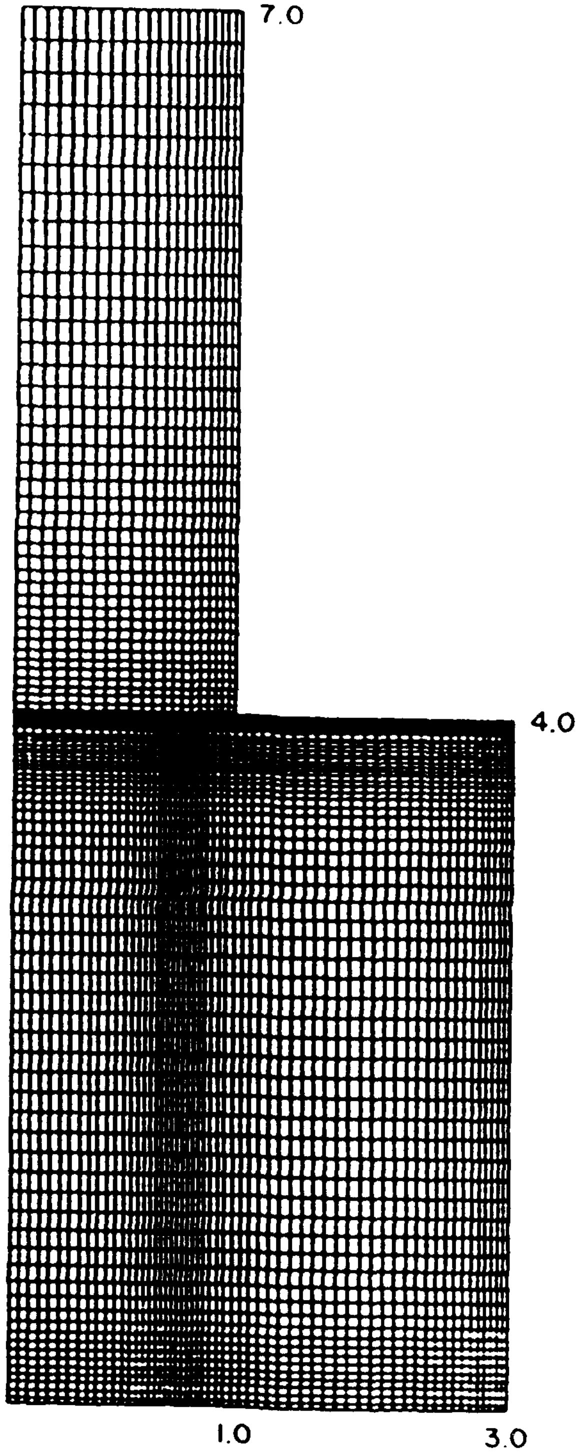

FIG. 5.1.16 - Group IV: Case 5 - Coordinates

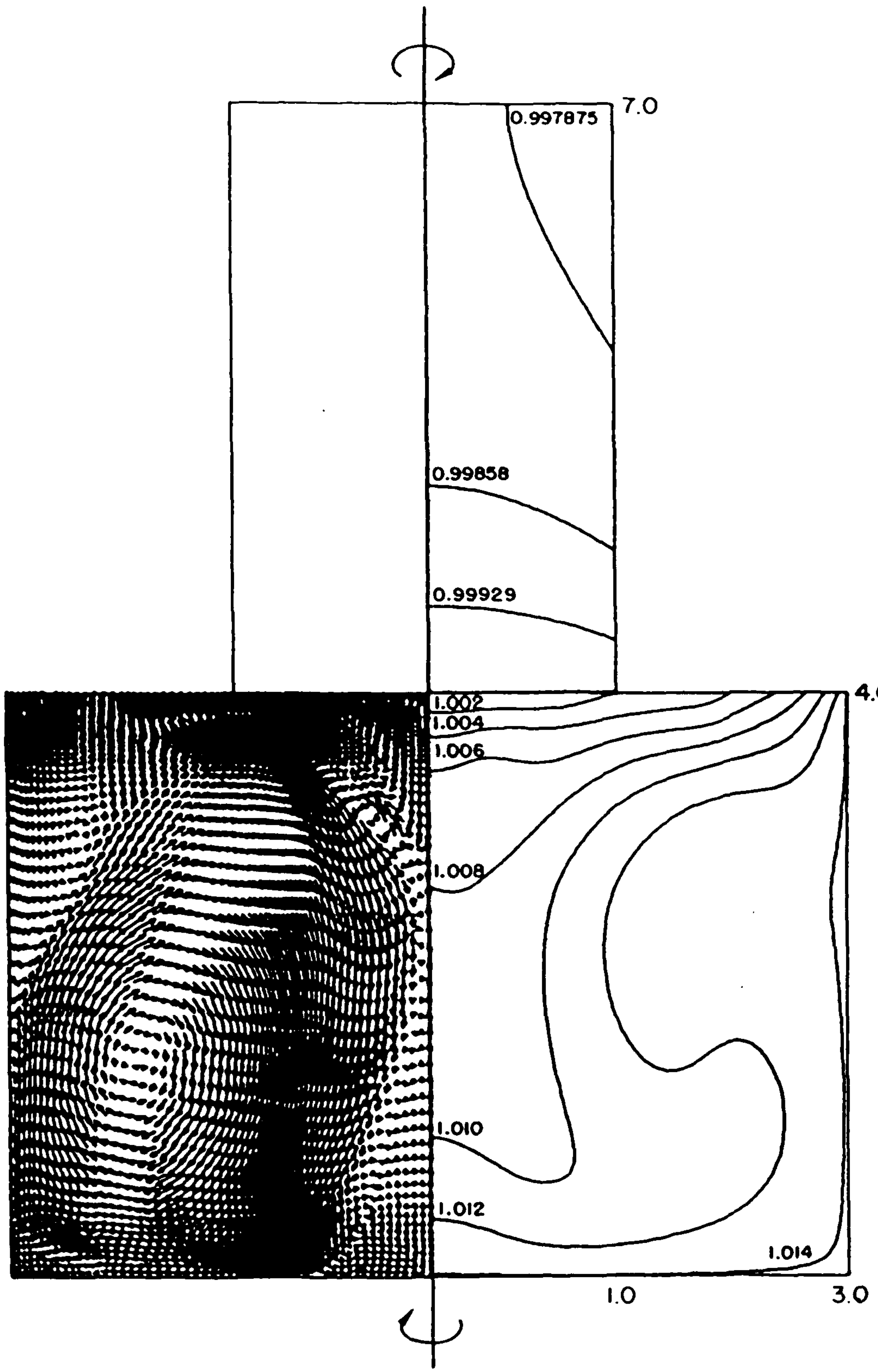

FIG. 5.1.17 - Group IV: Case 5 - Secondary Flow Field and Temperature Contours

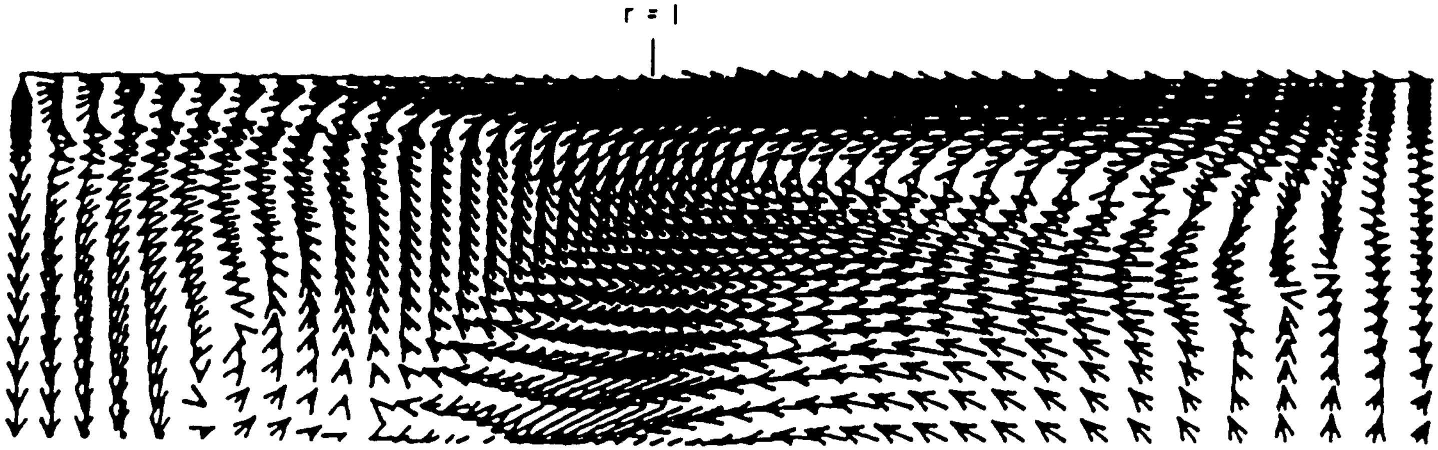

FIG. 5.1.18 - Group IV: Case 5 - Detail of the Secondary Flow Field Near the Melt-Crystal Interface

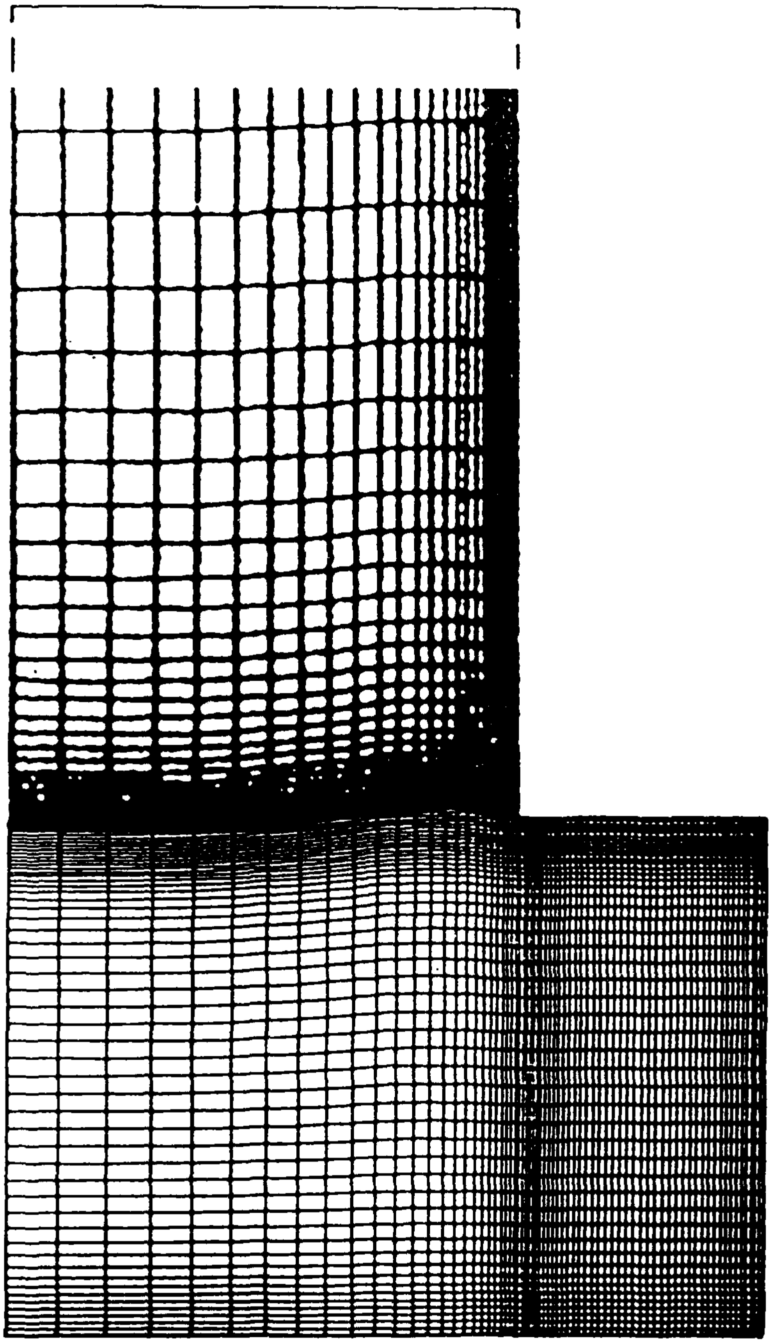

FIG. 5.1.19.a - Group IV: Case 6 - Coordinates for the Melt Phase

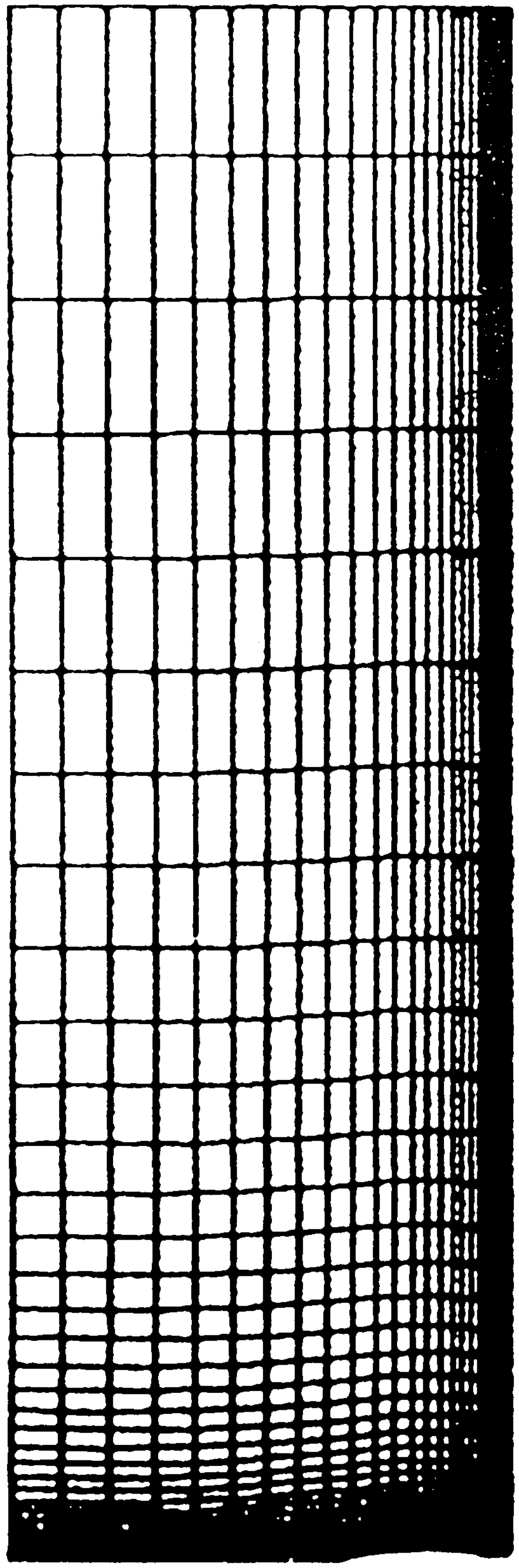

FIG. 5.1.19.b - Group IV: Case 6 - Coordinates for the Crystal Phase

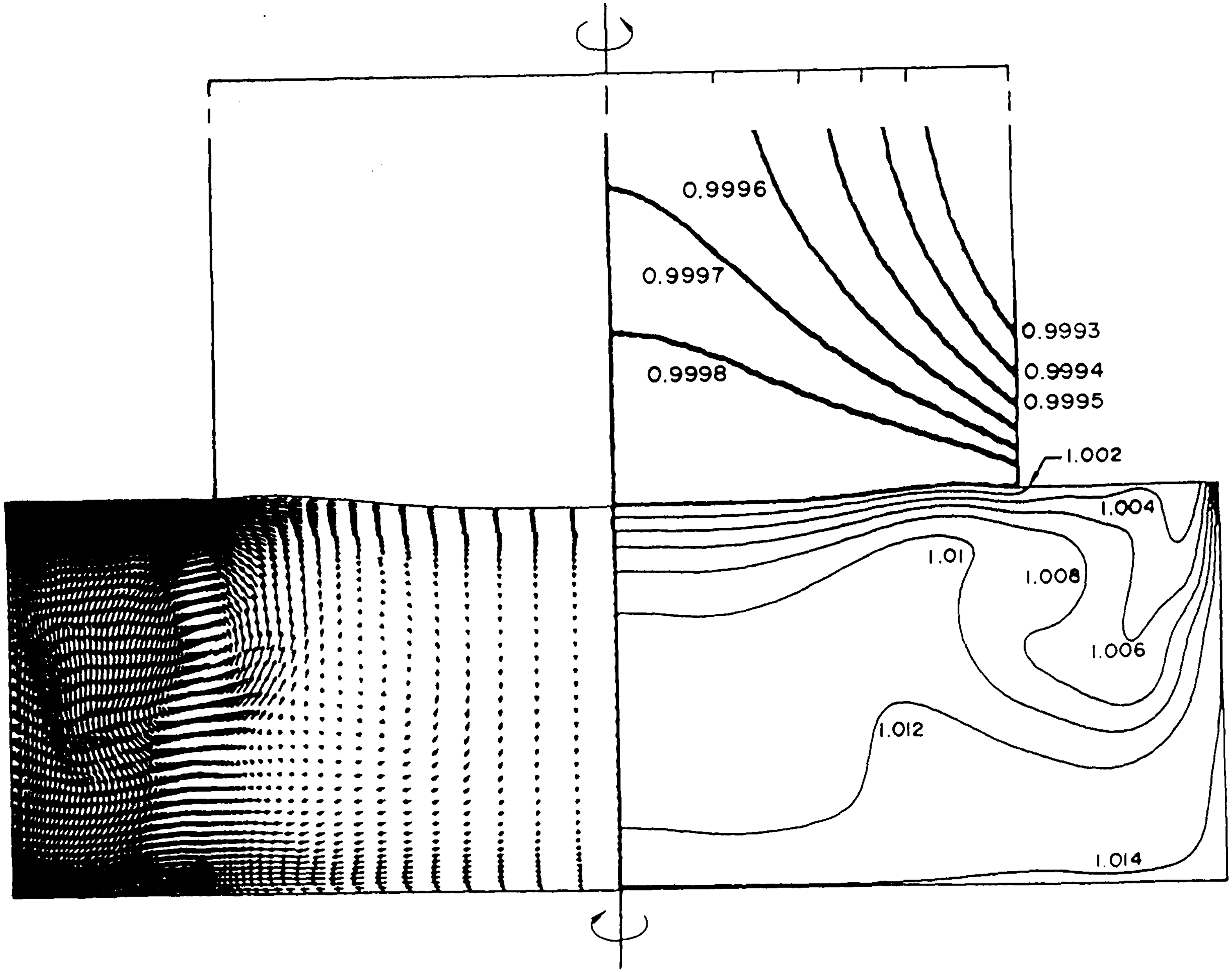

FIG. 5.1.20.a - Group IV: Case 6 - Secondary Flow
Field and Temperature Contours

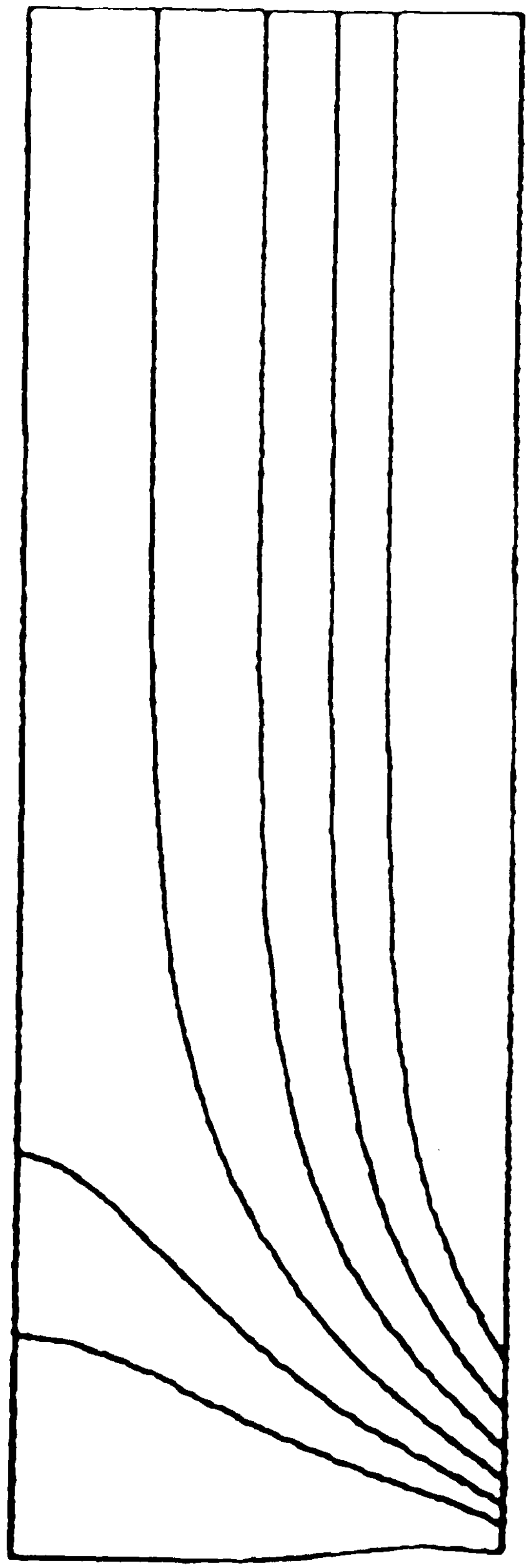

FIG. 5.1.20.b - Group IV: Case 6 - Temperature Contours of the Crystal Phase

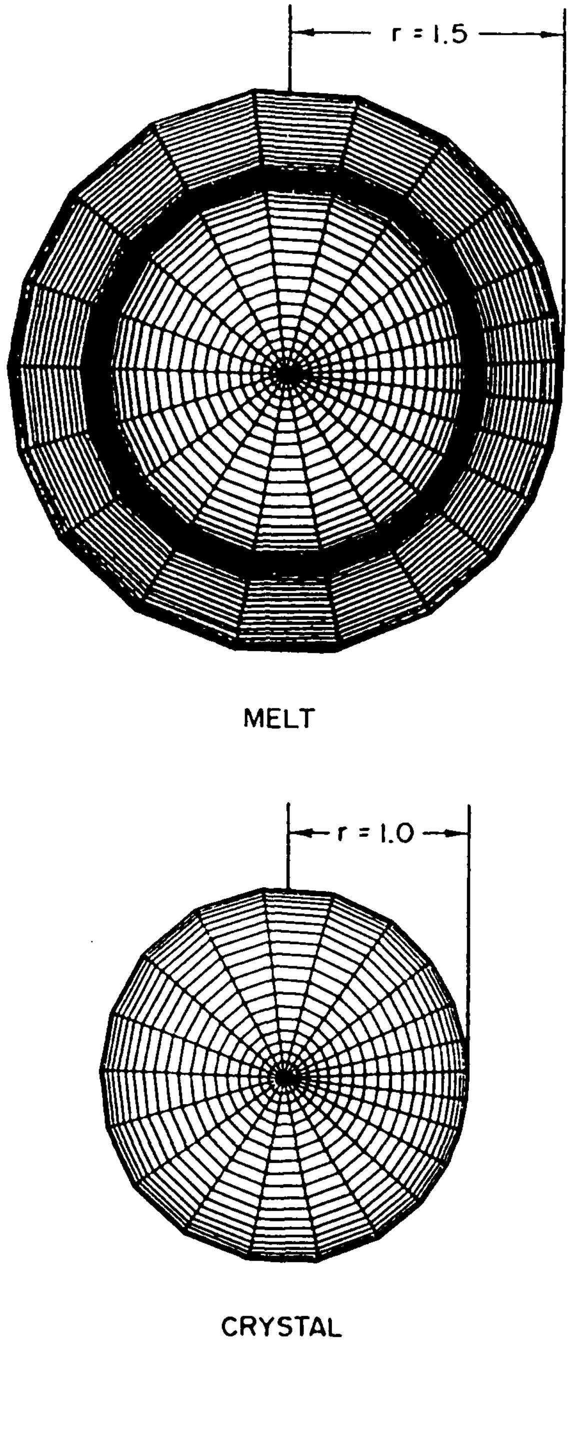

FIG. 6.1.1. - Group V: 3-D - Coordinates

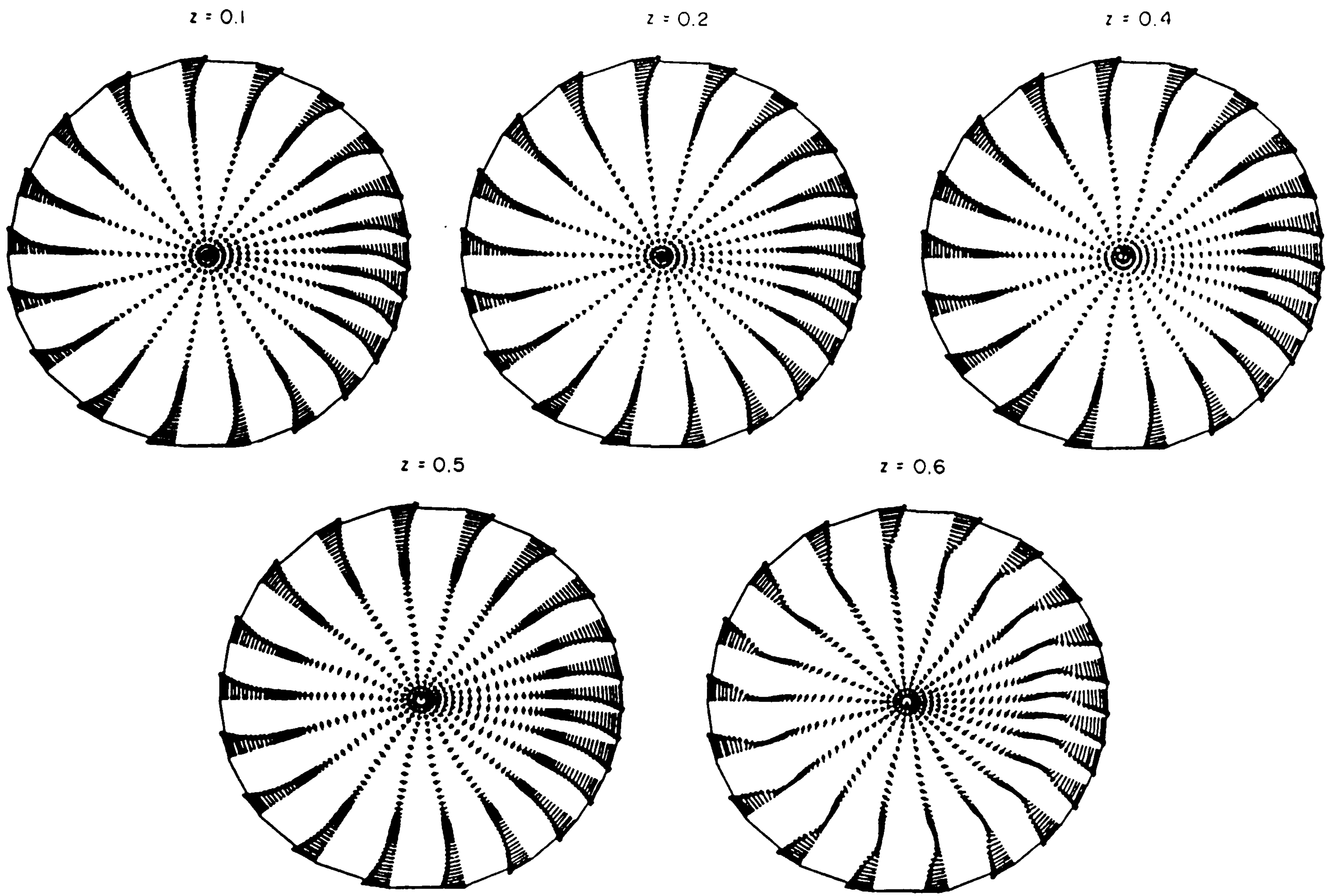

FIG. 6.1.2.a - Group V:3-D - Azimuthal Velocities in Various Horizontal Planes

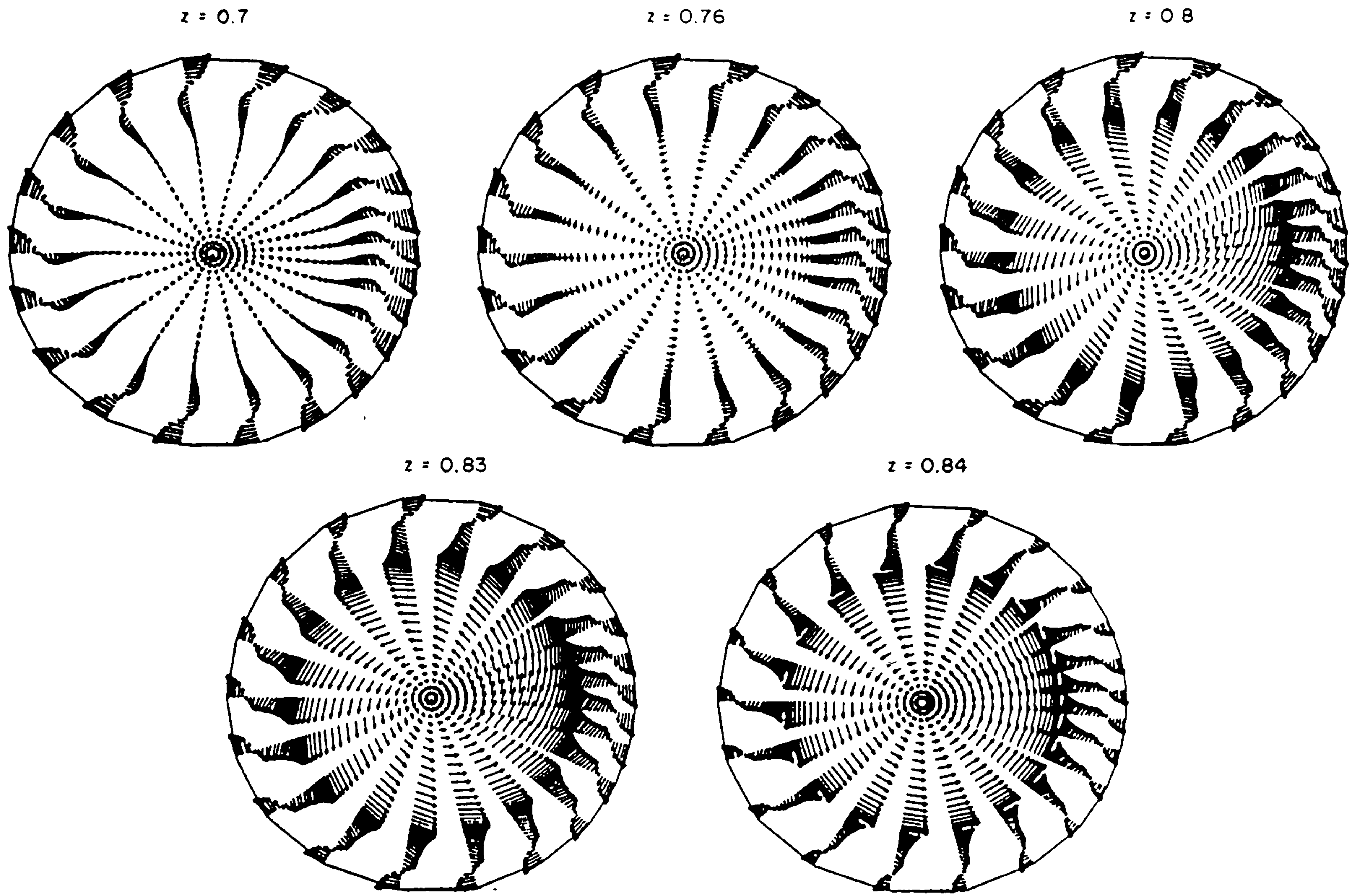

FIG. 6.1.2.b - Group V:3-D - Azimuthal Velocities in Various Horizontal Planes

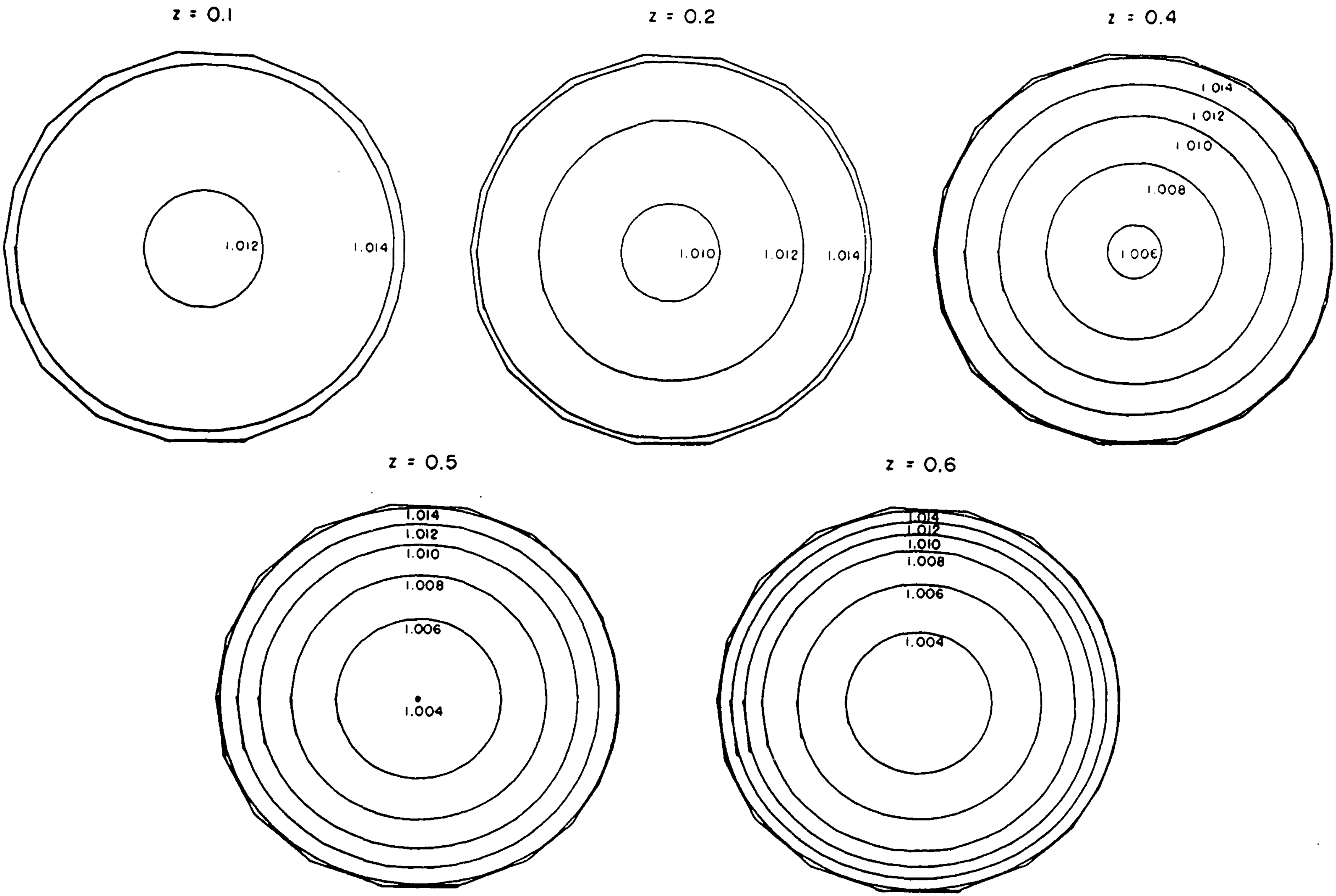

FIG. 6.1.3.a - Group V: 3-D - Temperature Contours in Various Horizontal Planes (Melt Phase)

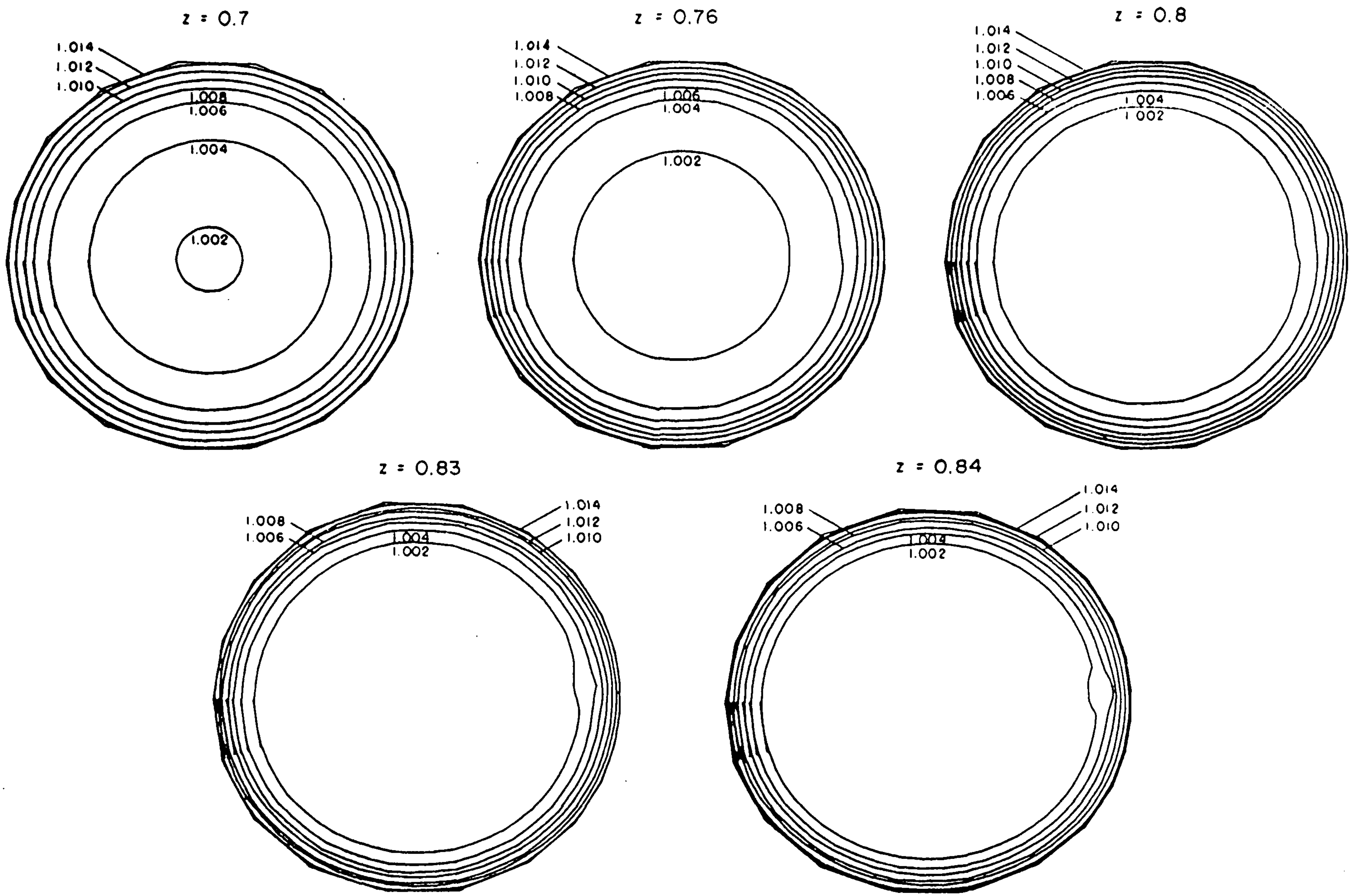

FIG. 6.1.3.b - Group V: 3-D - Temperature Contours in Various Horizontal Planes (Melt Phase)

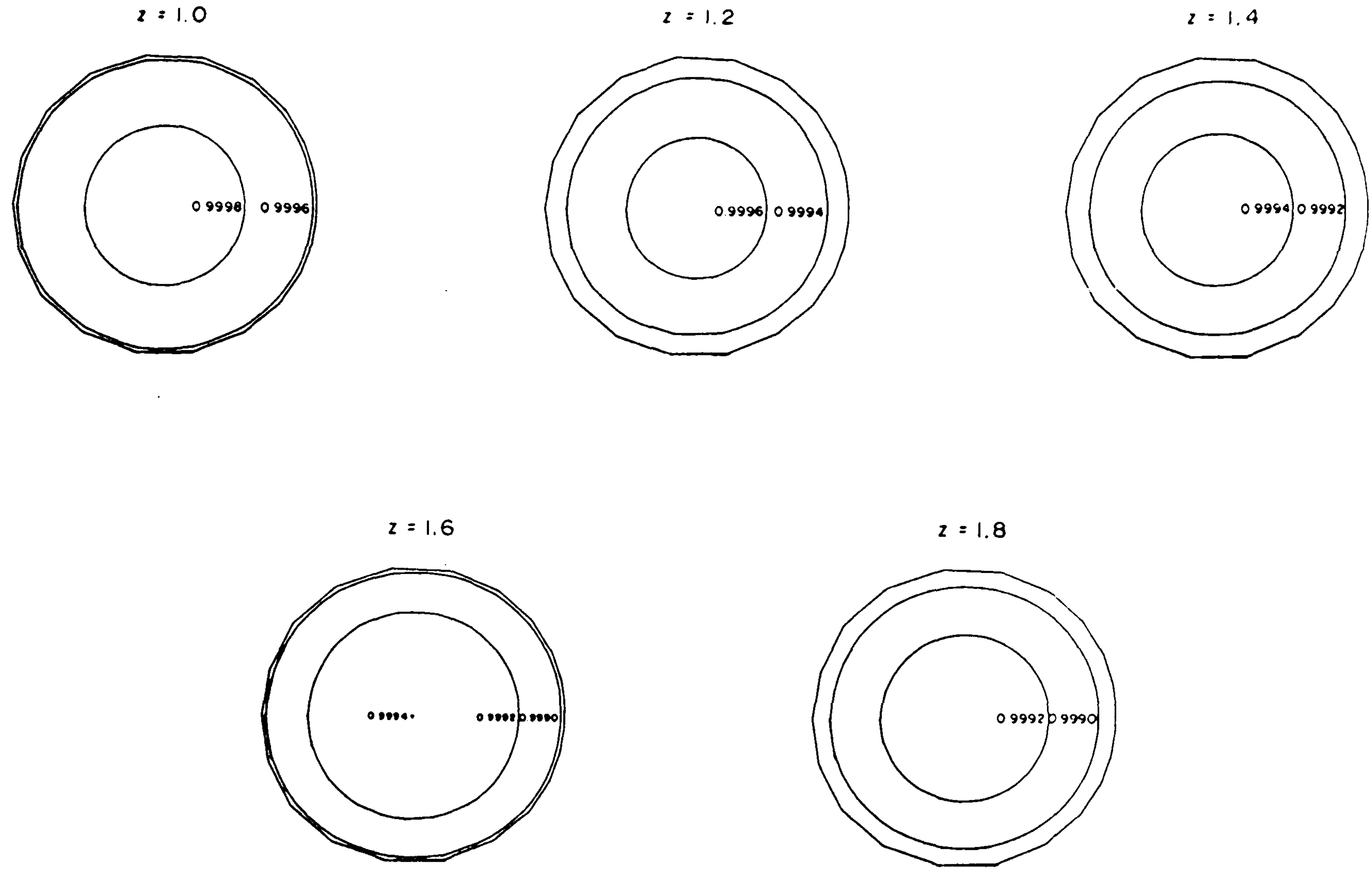

FIG. 6.1.4 - Group V: 3-D - Temperature Contours in Various Horizontal Planes (Crystal Phase)

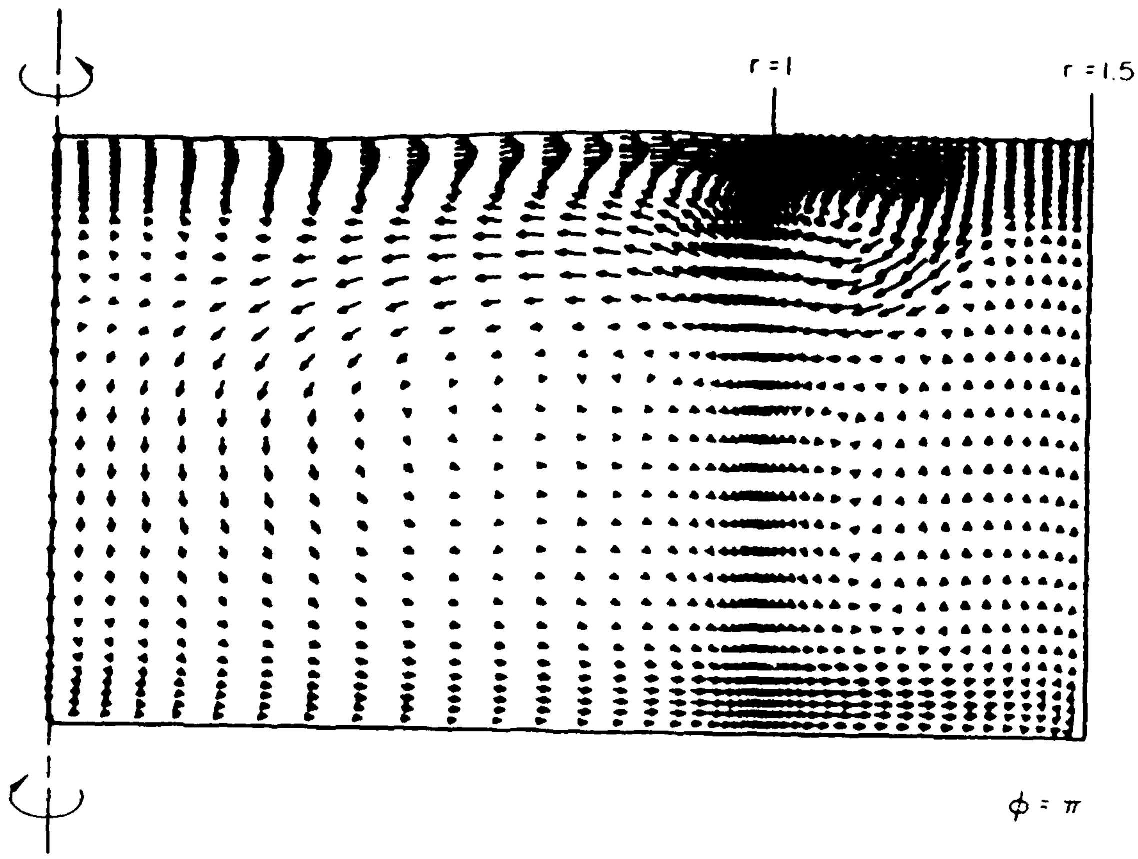

FIG. 6.1.5 - Group V: 3-D - Secondary Flow Field in a Vertical Plane Cutting Across the Perturbed Temperature Spot

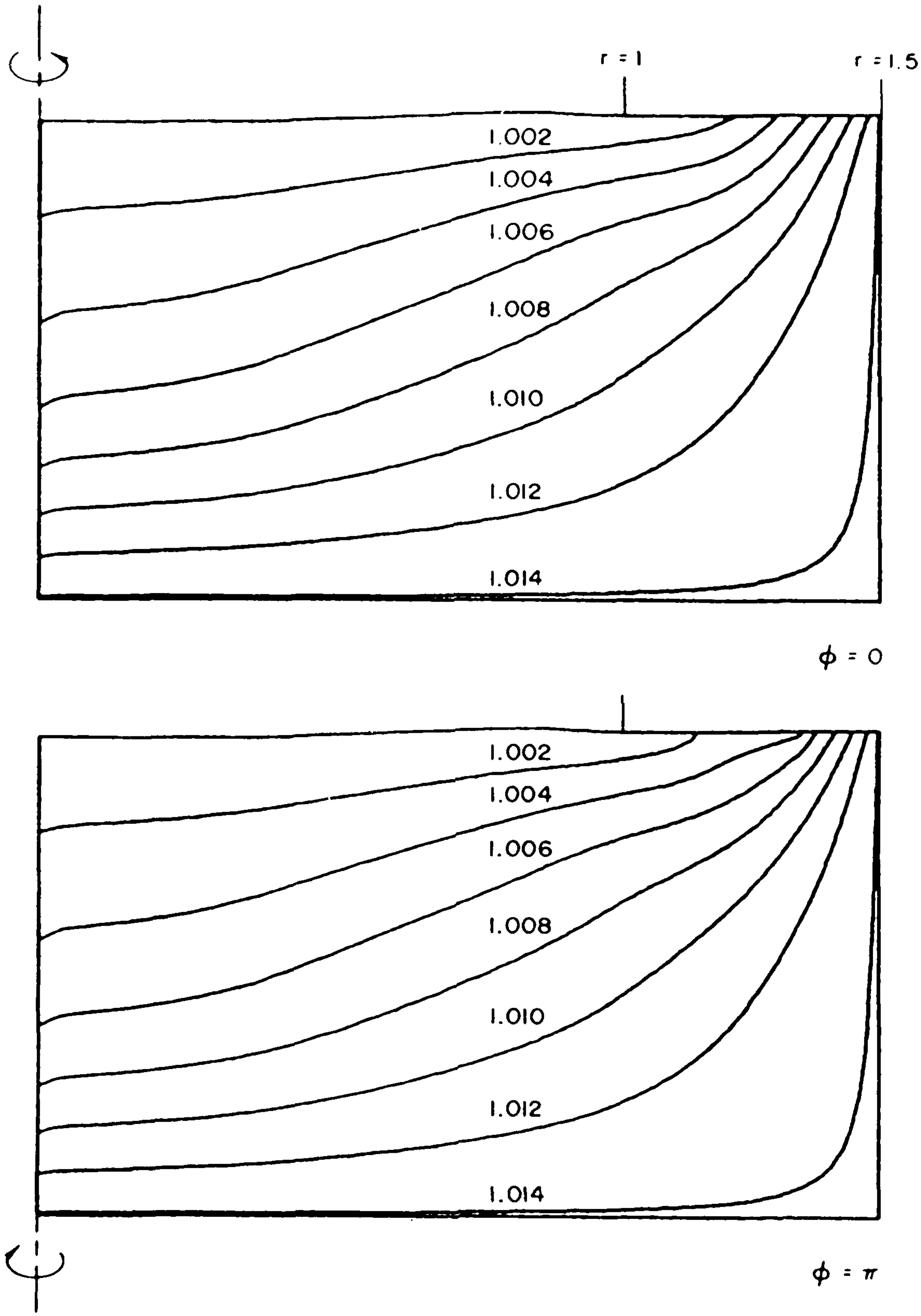

FIG. 6.1.6 - Group V: 3-D - Temperature Contours in a Vertical Plane Cutting Across the Perturbed Temperature Spot

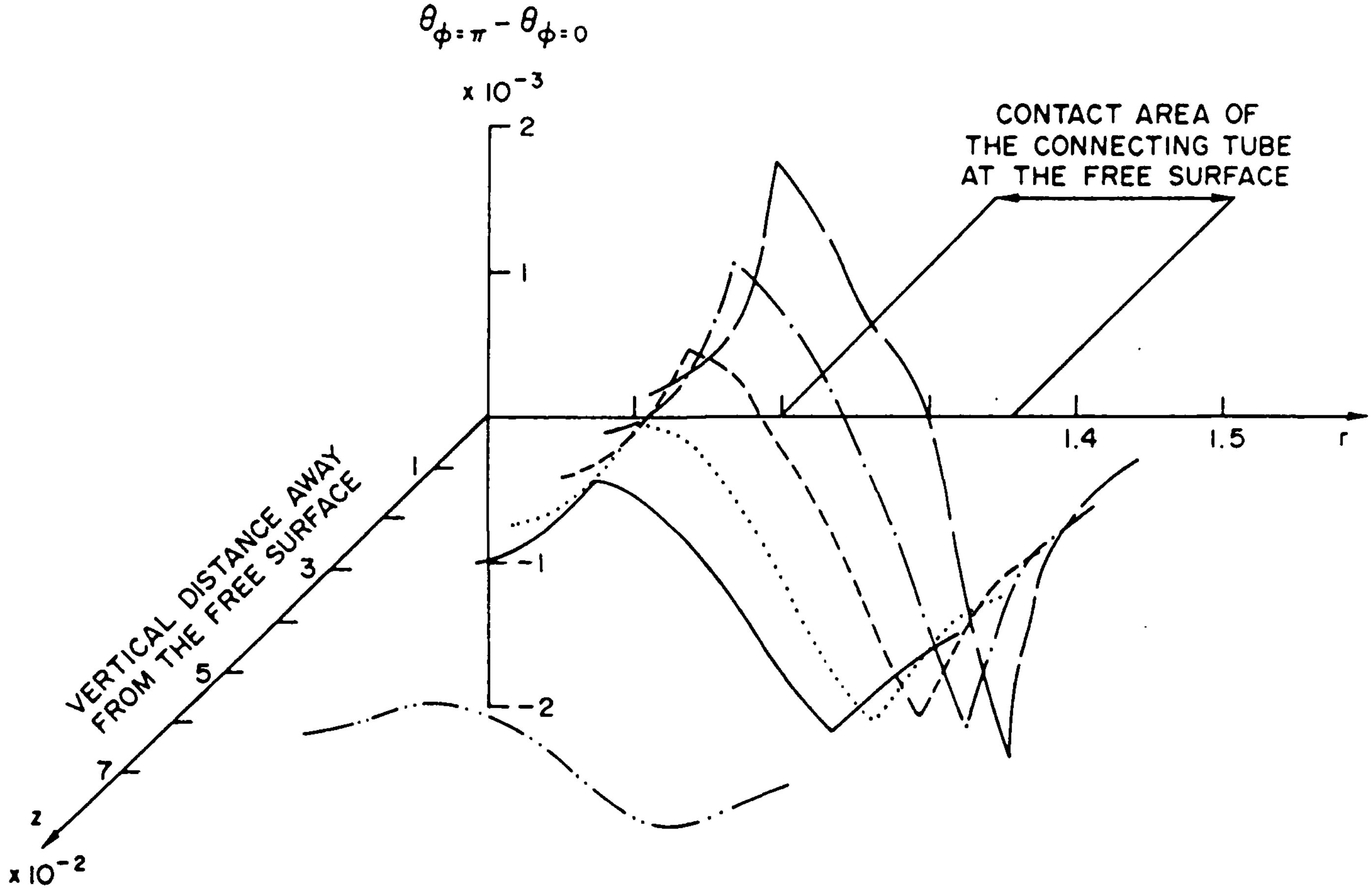

FIG. 6.1.7 - Group V: 3-D - Radial Temperature Difference vs. Depth of the Melt

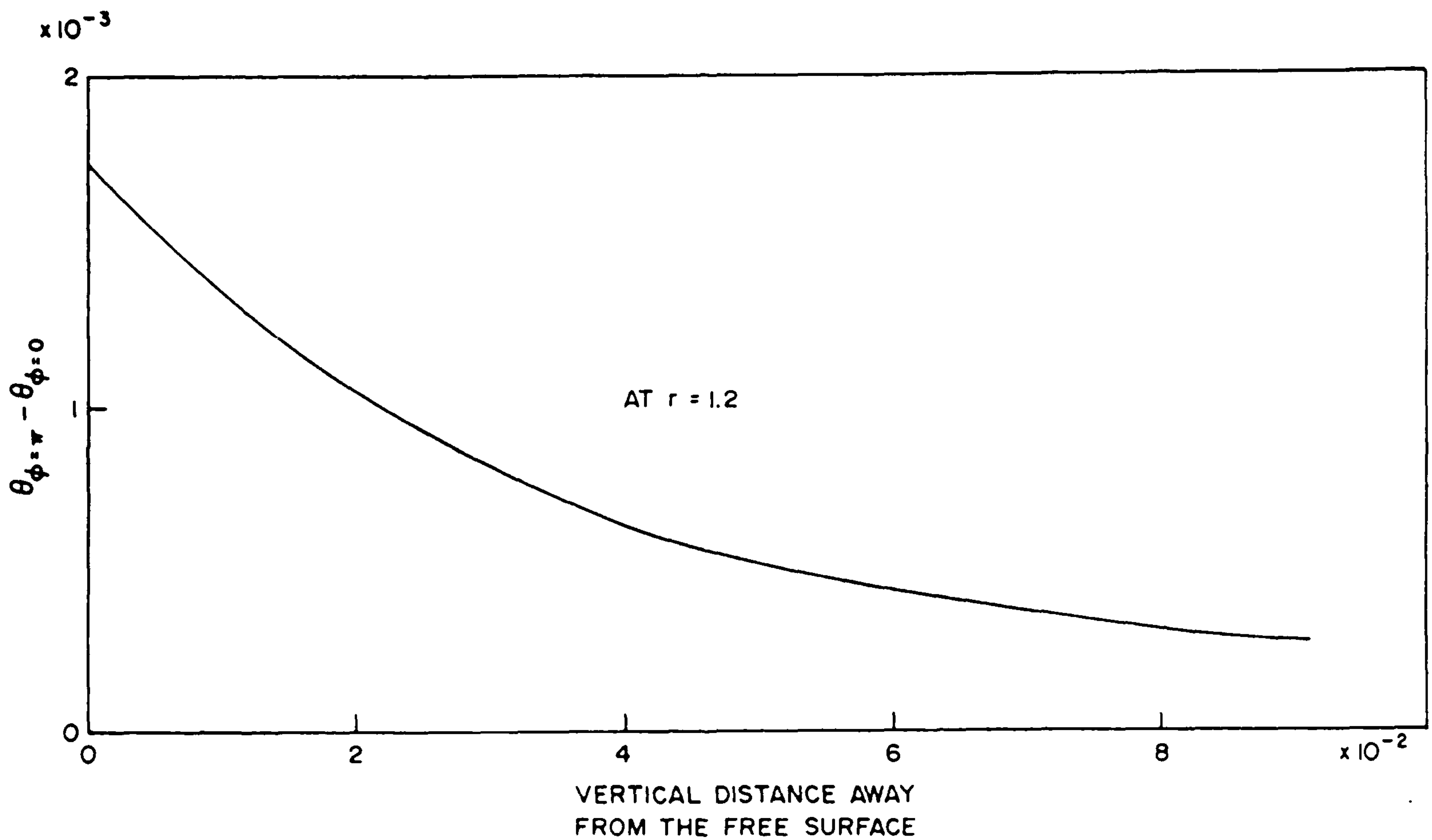

FIG. 6.1.8 - Group V: 3-D - Temperature Difference at r = 1.2 vs. Depth of the Melt

END

3-87

DTIC